Synthetic Lethality and Extracellular Vesicle Metabolism in Renal Cell Carcinoma

By

Aaron Richard Lim

Dissertation

Submitted to the Faculty of the

Graduate School of Vanderbilt University

in partial fulfillment of the requirements

for the degree of

DOCTOR OF PHILOSOPHY

in

Cancer Biology

May 31, 2021

Nashville, Tennessee

Approved:

Alissa M. Weaver, M.D., Ph.D. (chair)

Jin Chen, M.D., Ph.D.

Jeffrey C. Rathmell, Ph.D.

W. Kimryn Rathmell, M.D., Ph.D. (adviser)

DEDICATION

To my mother – Hope I made you proud

ACKNOWLEDGMENTS

The work described in this dissertation was funded by the following: T32 GM007347 (Vanderbilt MSTP), R01 CA203012 (WKR), R01 CA198482 (WKR), and the American Association for Cancer Research (AACR) Kure It Grant for Immunotherapy in Kidney Cancer.

First and foremost, thank you to my adviser, Dr. W. Kimryn Rathmell. Kim, you have always been a role model for me and so many others. Thank you for welcoming me into your lab as your first Vanderbilt graduate student with open arms. You exemplify what a leader and a physician-scientist should be, and I will always look up to you. I will forever cherish your mentorship, and I know I can always seek your advice in the future without hesitation.

I would also like to acknowledge my thesis committee members Drs. Alissa Weaver, Jeffrey Rathmell, and Jin Chen. You all challenged me to think critically about my data at every committee meeting. Thank you for your insightful questions that have made me a better scientist.

I would be remiss if I did not thank the entire Rathmell^2, Katy Beckermann, and Alissa Weaver labs. Anna, you always made sure to keep the lab well stocked and tracked down my orders when the FedEx or UPS delivery person lost the package. Esteban, thank you for all the laughs and fun conversations about our favorite television shows. Jamie, thank you for showing everyone how cool it is to wear a DNA dress. Stephen, for the fun sports talks every now and then. To Frank, for always reminding the lab how cool cell biology is by showing the best immunofluorescent images and movies. To Emily, for baking yummy goodies for the lab and keeping our lab organized. To Agi, for showing me how to be a great multitasker in lab. To Brad, for always giving me ten or more references whenever I asked a question about kidney cancer or the tumor microenvironment. To Melissa, for our interesting conversations about “The

Handmaid's Tale". To Matt, for always answering my flow cytometry questions without hesitation. To our undergraduate students Robert, Colby, Anuj, and others, thanks for making me feel old as we discussed life. To the Jeff Rathmell lab members, for showing the world the importance of immunometabolism in tumors. To the Katy Beckermann lab members, for showing me how to process blood and tumor samples. To the entire Weaver lab, thank you for accepting me as if I were a member of your lab and showing me how to study extracellular vesicles. It sure takes a village to complete a PhD, and without all of your help, I would not be here today. It was a privilege working alongside and learning from you all.

Thank you to all my past mentors who led me on this arduous yet rewarding path. To Monica Williams, the person who taught me how to pipet and how fun it is to work in a research laboratory at Children's Hospital Los Angeles while I was a high school student. To Drs. Henri Ford and Jeffrey Upperman, for showing me how fulfilling a career in both research and medicine would be while shadowing you on the wards of Children's Hospital Los Angeles and conducting research on necrotizing enterocolitis and *Enterobacter sakazakii* at the Saban Research Insitute. To Drs. Leonard B. Maggi, Jr. and Jason Weber, for teaching me how to conduct rigorous hypothesis-driven research, for asking me tough questions, for treating me like a regular member of the lab, and for showing me the joys of working on the toughest questions in cancer while I completed my undergraduate thesis research at Washington University in St. Louis.

A special thanks to everyone at Vanderbilt who helped me along this journey. To Dr. Terry Dermody, for giving me that phone call I would never forget: my acceptance to the Vanderbilt Medical Scientist Training Program. To the rest of the MSTP leadership team, Melissa Krasnove, Jim Bills, Larry Swift, Chris Williams, Megan Williams, Lourdes Estrada,

Sally York, Ambra Pozzi, Bryn, Sierra, and Danny Winder, for always being there for me and having my back in any situation. To the proteomics and imaging core facilities, thank you for bringing new dimensions to my data. To the Gabbe college students and Gabbe mentors, Drs. Ban Allos, Amy Fleming, and Matt Miller, for all of the stimulating discussions during learning communities. To Patrick Wu, for keeping me sane during the past seven years. To David Tovar, for keeping me physically fit during graduate school. To Goodpasture college, and especially to my MSTP family members Meredith Rogers, Paula Smith, MariaSanta Mangione, Eileen Shiuan, Kelsey McNew, Benjamin Fowler, Zack Williams, Matthew Loberg, and Sarah Reid, for being my family away from home.

Finally, thank you to my family. To my parents, thank you for showing me what it means to work hard. To my wife, Yao, for believing in me when I doubted myself, showing me what true love is, cooking delicious meals, and taking care of our child during a once-in-a-century pandemic. To my daughter born during a pandemic, Ariana, for always having a smile on her face whenever I come home from the lab. To my siblings, for constantly reminding me what life is like outside of being a student. To my father-in-law and mother-in-law, for welcoming me into your family, for providing a delicious meal and a place to stay for the holidays. Without my family's unwavering support, none of this would have been possible.

TABLE OF CONTENTS

PAGE

LIST OF TABLES

Table **Page**

LIST OF FIGURES

LIST OF ABBREVIATIONS

2-DG – 2-deoxygulcose

2-HG – 2-hydroxyglutarate

4EPB1 – 4E-binding protein 1

ACT – Adoptive cell transfer

ALIX – ALG-2 Interacting Protein X

ARF6 – ADP ribosylation factor 6

ARMM – ARRDC1-mediated microvesicle

ARRDC1 – Arrestin domain containing protein 1

ATCC – American Type Culture Collection

BAP1 – BRCA-associated protein 1

BHD – Birt-Hogg-Dubé

CAF – Cancer-associated fibroblast

CAR – Chimeric antigen receptor

ccRCC – Clear cell renal cell carcinoma

CEMIP – Cell migration inducing and hyaluronan-binding protein

CHMP4A – Charged MVB protein 4A

ChRCC – Chromophobe renal cell carcinoma

CPT1A – Carnitine palmitoyltransferase 1A

CTLA-4 – Cytotoxic T lymphocyte associated protein 4

DMSO – Dimethyl sulfoxide

ECM – Extracellular matrix

EGF – Epidermal growth factor

EGFR – Epidermal growth factor receptor

ESCRT – Endosomal sorting complex required for transport

ETC – Electron transport chain

EV – Extracellular vesicle

EZH2 – Enhancer of Zeste Homolog 2

FasL – Fas ligand

FBP – Fructose bisphosphatase

GAPDH – Glyceraldehyde 3-phosphate dehydrogenase

GDSC – Genomics of drug sensitivity in cancer

GLS – Glutaminase

GLUT1 – Glucose transporter 1

H3K27me3 – Histone 3 lysine 27 trimethylation

H3K36 – Histone 3 Lysine 36

H3K36me3 – Histone 3 lysine 36 trimethylation

HIF – Hypoxia-inducible factor

HK-2 – Hexokinase 2

ICB – Immune checkpoint blockade

IDO – Indoleamine 2,3-dioxygenase

IFN-α – Interferon-α

ILV – Intraluminal vesicle

ISG15 – Interferon-stimulated gene 15

iTRAQ – Isobaric tag for relative and absolute quantitation

kDa – Kilodalton

KO – Knockout

LC-MS – Liquid chromatography-tandem mass spectrometry

LCMV – Lymphocytic choriomeningitis virus

LDH-A – Lactate dehydrogenase A

lEV – Large extracellular vesicle

MDSC – Myeloid-derived suppressor cell

MFI – Median fluorescence intensity

MHC – Major histocompatibility complex

miRNA – microRNA

MLCK – Myosin light-chain kinase

MMP – Matrix metalloproteinase

mTOR – Mammalian target of rapamycin

MudPIT – Multidimensional protein identification technology

MVB – Multivesicular body

NFAT – Nuclear factor of activated T cells

nSMase2 – sphingomyelinase 2

OE – Overexpressing

PBRM1 – Protein polybromo 1

PCP – Planar cell polarity

PD-1 – Programmed cell death 1

PD-L1 – Programmed cell death ligand 1

PDGF – Platelet-derived growth factor

PDK1 – Phosphoinositide-dependent kinase 1

PGC-1α – Peroxisome proliferator-activated receptor-γ coactivator 1α

PH – Pleckstrin homology

PHD – Prolyl hydroxylase domain

PI3K – Phosphoinositide-3-kinase

PRAS40 – Proline-rich AKT substrate of 40 kilodaltons

PRC1 – Polycomb repressive complex 1

pRCC – Papillary renal cell carcinoma

PtdIns-3,4,5-P_3 – Phosphatidylinositol-3,4,5-trisphosphate

PtdIns-4,5-P_2 – Phosphatidylinositol-4,5-bisphosphate

PTEN – Phosphatase and tensin homolog

RBD – Ras binding domain

RCC – Renal cell carcinoma

RHEB – Ras homolog enriched in brain

RIG-I – Retinoic acid-inducible gene I

RISC – RNA-induced silencing complex

ROS – Reactive oxygen species

SEM – Standard error of the mean

SET – Suppressor of variegation, enhancer of zeste and trithorax

sEV – Small extracellular vesicle

SH2 – Src homology 2

SLC2A1 – Solute carrier family 2 member 1

SNAP – Synaptosomal-associated protein

SNARE – Synaptosomal-associated protein receptor

SNAT1 – Sodium-coupled neutral amino acid transporter 1

SOCS3 – Suppressor of cytokine signaling 3

SRI – Set2 Rbp1 interacting

STAT1 – Signal transducer and activator of transcription 1

SWI/SNF – SWitch/Sucrose non-fermentable

TAM – Tumor associated macrophage

TCGA – The cancer genome atlas

TCR – T cell receptor

TIL – Tumor-infiltrating lymphocyte

TKI – Tyrosine kinase inhibitor

TME – Tumor microenvironment

TRAIL – Tumor necrosis factor-related apoptosis-induced ligand

TRBP – TAR RNA binding protein

Treg – Regulatory T cell

TrpC5 – Transient receptor potential channel 5

TSC2 – Tuberous sclerosis complex 2

tSETD2 – Truncated SETD2

TSG101 – Tumor susceptibility gene 101

VEGF – Vascular endothelial growth factor

VEGFR – Vascular endothelial growth factor receptor

VHL – von Hippel-Lindau

WCL – Whole cell lysate

CHAPTER I

RENAL CELL CARCINOMA BACKGROUND AND LITERATURE REVIEW

Introduction to Renal Cell Carcinoma

Although the incidence and mortality rate of cancer is declining in the United States, the number of kidney cancer cases continues to rise, with over 73,000 new diagnoses in 2020[1–3]. Kidney cancer is the deadliest urologic malignancy and remains among the top ten most commonly diagnosed tumors each year, accounting for approximately 4% of all new cancer diagnoses in the United States[1]. Worldwide, kidney cancer accounts for 2% of global cancer deaths[4].

The most common form of kidney cancer arises from the epithelial cells in the nephron and is called renal cell carcinoma (RCC), which accounts for 90% of adult kidney cancer. Although most cases of RCC are detected as incidental findings on imaging studies, some patients present with the classic triad of hematuria, flank pain, and a palpable abdominal mass[1]. Up to one-third of patients with RCC present with or later develop metastatic disease, which confers a 12% 5-year survival rate[4,5]. Several modifiable and unmodifiable risk factors are strongly correlated with RCC, including smoking, obesity, hypertension, age, sex, and race[1,4]. The average age of diagnosis is 64 years old, and males are affected more than females in a two-to-one ratio[4]. Hispanic Americans, African Americans, and Native Americans have a higher risk for RCC and tend to have worse survival rates than White Americans[6]. Ongoing efforts to

understand the interplay between all of these factors may provide novel insights into RCC biology.

RCC is traditionally divided into several subtypes based on histological characteristics[7,8]. The most common histologic subtype is clear cell renal cell carcinoma (ccRCC), which accounts for 75% of RCCs[9]. Papillary RCC (pRCC), chromophobe RCC (ChRCC), and other rarer tumor subtypes encompass the remaining 25% of RCCs. In addition, sarcomatoid features, which predict a more aggressive tumor, can be found in 20% of advanced RCC cases[10].

With recent advances in sequencing and integration of genomic, epigenomic, transcriptomic, proteomic, and metabolomic data[11], RCC is now recognized as a heterogenous tumor, and RCC classification schemes have been expanded to include multiple molecular subtypes to risk stratify patients and predict response to certain therapies[10,12,13]. One recent RNAseq study of over 800 advanced RCC tumors revealed eight molecular subtypes: angiogenic/stromal, angiogenic, complement/Ω-oxidation, T-effector/proliferative, proliferative, stromal/proliferative, and small nucleolar RNA[10]. For the remainder of this dissertation, I will focus on ccRCC, given that it is the predominant subtype.

Genomic Landscape of Clear Cell Renal Cell Carcinoma

von Hippel-Lindau and hypoxia inducible factor

ccRCC is characterized by loss of the tumor suppressor gene von Hippel-Lindau (*VHL*), which occurs in 90% of cases[14–17]. A recent set of studies from the TRACERx group, which sequenced multiple regions of over one hundred tumor samples, detailed the evolutionary history of ccRCC[13,18]. They showed that a chromothripsis event occurs early in childhood or adolescence

with loss of chromosome 3p, on which the *VHL* gene resides, and gain of chromosome 5q[13,18]. Decades later, an inactivating mutation of the other copy of *VHL* or methylation of its promoter occurs[13,18]. The importance of *VHL* loss in the pathogenesis of RCC is underscored by the fact that patients with VHL syndrome, an autosomal dominant genetic condition associated with a germline mutation of *VHL*, develop multiple, bilateral kidney cysts and tumors, usually of the clear cell subtype[19].

Seminal reports from the laboratories of Nobel laureates William Kaelin, Jr., Gregg Semenza, and Sir Peter Radcliffe, as well as others, illustrate the central role VHL plays in cells as an oxygen sensor and an antagonist of the hypoxia signaling pathway [Figure 1]. *VHL* can be translated into two proteins: a larger, 24-30 kilodalton (kDa) protein and a smaller, 18-20 kDa protein[20]. The smaller VHL protein is the predominant form in most cells, though it is unclear why cells produce both forms[20]. When cells sense oxygen, prolyl-hydroxylase domain (PHD) dioxygenase proteins hydroxylate hypoxia-inducible factor (HIF), allowing VHL to bind to HIF[20–23]. VHL forms a complex with Cullin2, RBX, Elongin B, and Elongin C [Figure 2] and functions as an E3 ubiquitin ligase, attaching ubiquitin molecules onto the α subunit of HIF to mark it for degradation by the 26S proteasome[22,23]. However, when there is a lack of oxygen, which commonly occurs in the tumor microenvironment, or when a "pseudohypoxic" state occurs with the absence of VHL, HIFα will escape proteolysis, leading to HIFα accumulation. Consequently, HIFα is free to form a heterodimer with HIF-1β and translocate from the cytosol to the nucleus to activate genes associated with hypoxia-response elements such as vascular endothelial growth factor (*VEGF*) to promote angiogenesis, glucose transporter 1 (*GLUT1*) to induce glucose uptake, and other genes to promote other biological processes such as cell growth and survival[22,24,25] [Figure 1].

Although both HIF-1α and HIF-2α can activate genes associated with hypoxia-response elements, there is still debate about which isoform is more important in ccRCC. Both *in vitro* and *in vivo* studies suggest that HIF-2α is an oncoprotein critical for ccRCC tumorigenesis – indeed, inhibition of HIF-2α was sufficient to suppress *VHL*-deficient ccRCC growth[26,27]. On the other hand, there have been reports supporting a tumor suppressor role for HIF-1α. Loss of chromosome 14q, on which the *HIF1A* gene resides, portends a poor prognosis in ccRCC[28,29]. In fact, one study found that 40% of ccRCC cases have loss of chromosome 14q that encompasses the *HIF1A* locus[28]. Moreover, HIF-1α stabilization under normoxic conditions was not sufficient to induce tumorigenesis[30], and overexpression of HIF-1α impeded tumor growth *in vitro* and *in vivo*[28,31]. However, a recent study using an autochthonous mouse model of ccRCC showed that HIF-1α is critical for tumor formation, whereas HIF-2α had insignificant effects on tumor growth in this model[32]. This model had the advantage of having an intact immune system, which xenograft studies performed previously did not have, and thus may better model the ccRCC tumor microenvironment. However, *Rb1,* which negatively regulates E2F transcription factors to antagonize cell cycle progression, was deleted in their mouse model, which may be partially redundant with HIF-2α's function to activate Myc-dependent cell cycle progression. Although this preclinical work has been leveraged to develop HIF-2α inhibitors, which have demonstrated efficacy against ccRCC in early clinical trials[33,34], differentiating the roles of each HIF isoform in ccRCC with different genetic backgrounds warrants further exploration.

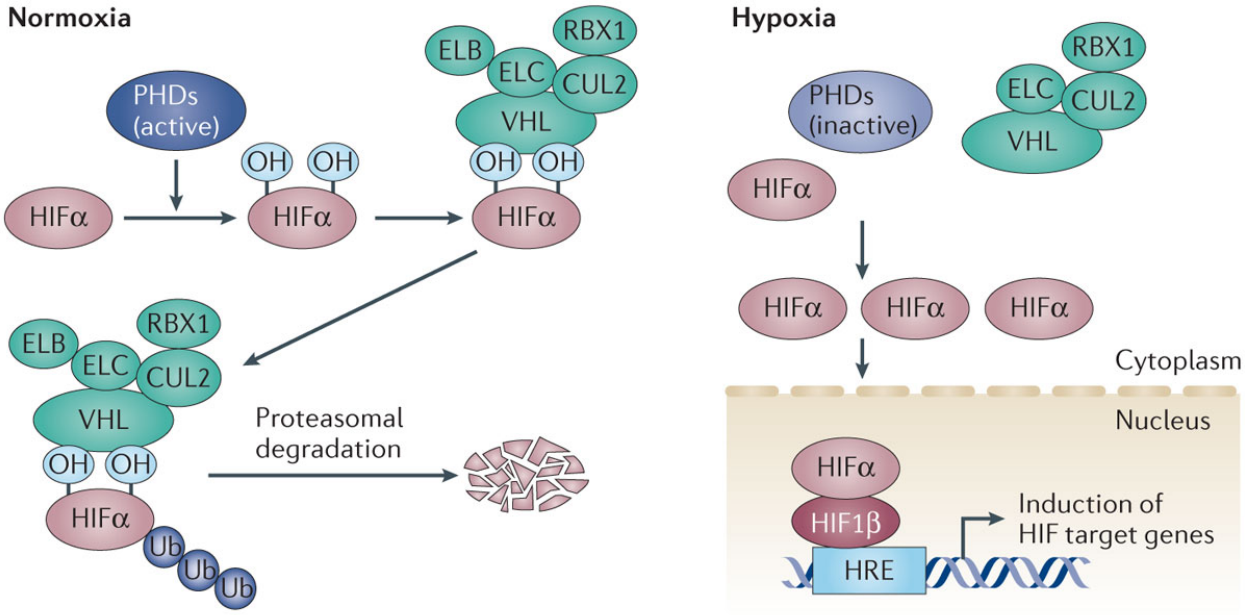

Figure 1. VHL regulation of hypoxia-inducible factors

In normoxic conditions, hypoxia-inducible factorα (both HIF1α and HIF2α) are hydroxylated on one or both of two conserved proline residues by prolyl hydroxylase 1 (PHD1), PHD2, and PHD3. Prolyl-hydroxylated HIFα is recognized by the VHL–elongin C (ELC)–elongin B–cullin 2 (CUL2)–RBX1 E3 ubiquitin ligase complex and targeted for ubiquitylation (Ub) and proteasomal degradation. In hypoxic conditions, PHD1, PHD2, and PHD3 are inactive (oxygen is an essential cofactor). HIFα therefore accumulates and forms heterodimers with HIF1β. These heterodimers translocate to the nucleus, bind to hypoxia-response elements (HREs) and induce the transcription of genes involved in adaptations to hypoxia. The figure and caption were reproduced and adapted with permission[17]; permission conveyed through Copyright Clearance Center.

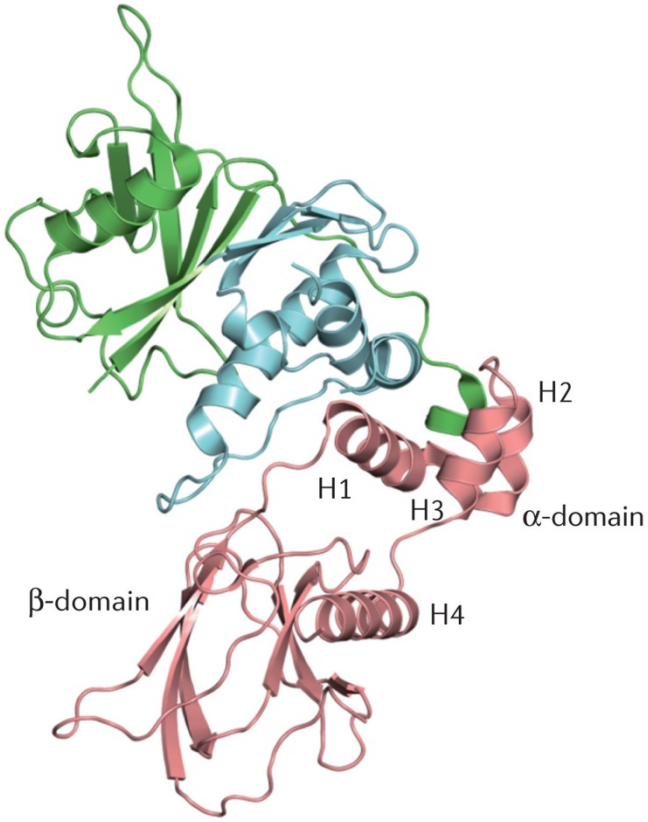

Figure 2. Ribbon diagram of the VHL-elongin B-elongin C complex

von Hippel–Lindau protein (VHL; pink) consists of two tightly coupled domains, α and β. The β-domain consists of seven strands arranged in two β-sheets in a sandwich arrangement with an α-helix, and it has the properties of a substrate docking site. The α-domain consists of three α-helices and binds to elongin C (blue). The H4 helix of elongin C fits into an extended groove formed by the H1, H2, and H3 helices of the VHL α-domain. The VHL–elongin C complex nucleates a complex containing elongin B (green), cullin 2 (not shown) and the RING finger protein RBX1 (not shown). The figure and caption were reproduced and adapted with permission[17]; permission conveyed through Copyright Clearance Center.

Chromatin modifier SETD2

Although *VHL* loss is a hallmark of ccRCC, alterations in *VHL* alone are not sufficient to generate renal tumors[35–37]. Subsequent mutations in key genes, particularly in genes located on chromosome 3p, occur during ccRCC tumorigenesis. Among the most commonly mutated driver genes in ccRCC include "writers" of the histone code[38,39] such as protein polybromo 1 (*PBRM1*), BRCA-associated protein 1 (*BAP1*), and SET Containing Domain 2 (*SETD2*) [Figure 3]. Mutations in these chromatin modifiers have been found to induce chromosomal instability and a more aggressive phenotype in ccRCC[40–44]. PBRM1 encodes a component of the SWitch/Sucrose Non-Fermentable (SWI/SNF) chromatin remodeling complex[45] and represses genes involved in hypoxia signaling[46]. BAP1, which is rarely mutated concurrently with PBRM1 in ccRCC[13], is a deubiquitinase involved in homologous recombination that maintains genomic integrity[47]. For more information about these two chromatin modifiers, the reader is referred to the *Nature Reviews Urology* review article by de Cubas and Rathmell[48]. The remainder of this sub-section will focus on *SETD2* as it is more relevant for the subsequent chapters of this dissertation.

Originally discovered in a yeast-2-hybrid screen to interact with huntingtin protein[49], *SETD2* has been shown to be mutated in many cancer types[50,51]. *SETD2* was first discovered to be mutated in ccRCC in 2010[52], and further genomic studies demonstrate that approximately 15% of ccRCC cases contain mutations in *SETD2* [Figure 3]. SETD2 is classically known as a N-lysine histone methyltransferase, and it is the only protein known to trimethylate histone 3 lysine 36 (H3K36me3), which marks actively transcribed genes [Figure 4]. This trimethylation activity is mediated by its Suppressor of variegation, Enhancer of Zeste and Trithorax (SET) domain. SETD2 also contains a Set2 Rpb1 Interacting (SRI) domain, which binds the Rpb1 subunit on the C-terminal domain of RNA polymerase[50,51]. Consequently, SETD2 performs a

myriad of functions related to maintaining genomic integrity and transcription, including engaging the p53-mediated checkpoint, recruiting the DNA repair machinery to active sites of transcription[53,54], mRNA processing[55], and preventing cryptic transcription[56], to name a few.

Recently, several studies have uncovered the diversity of SETD2's substrates, showing that this versatile methyltransferase has non-histone targets. For example, SETD2 was shown to trimethylate lysine 68 on actin and is a key regulator of actin polymerization/depolymerization dynamics and cell migration[57]. SETD2 was shown to trimethylate another cytoskeleton protein: α-tubulin at lysine 40[58]. Loss of this trimethylation mark on α-tubulin leads to chromosomal segregation errors and formation of micronuclei[58]. In fact, haploinsufficiency of *SETD2*, which is frequently seen with loss of the short arm of chromosome 3 in the early stages of ccRCC pathogenesis, induced loss of the α-tubulin lysine 40 trimethylation mark[59]. Even though SETD2's ability to trimethylated H3K36 remained intact in these cells, ablation of α-tubulin lysine 40 trimethylation was sufficient to form chromosomal bridges and lagging chromosomes during mitosis, suggesting that loss of the trimethylation mark on tubulin is an early driver of genomic instability in ccRCC[59].

Other targets of SETD2 besides histones and cytoskeletal proteins include Signal Transducer and Activator of Transcription 1 (STAT1) and Enhancer of Zeste Homolog 2 (EZH2). SETD2 can mono-methylate lysine 525 on STAT1, which was shown to be required for subsequent phosphorylation of STAT1 and its transcriptional activity[60]. Without SETD2, liver cells were more susceptible to infection by hepatitis B virus, highlighting the importance of this methyltransferase in antiviral responses[60]. In addition, SETD2 can mono-methylate lysine 735 on EZH2, leading to EZH2 degradation via Smurf2 E3 ubiquitin ligase and hindering prostate cancer metastasis[61]. An R1523 missense mutation in *SETD2* is found in a subset of prostate

cancer, which disrupts its interaction with EZH2 but not its H3K36me3 activity[61]. This indicates SETD2's antagonism of EZH2 and not its histone methylating activity may be more critical for tumor suppression in prostate cancer. Ongoing work aimed at identifying novel targets of SETD2 will broaden our understanding of this multifaceted methyltransferase and its diverse cellular functions in disease.

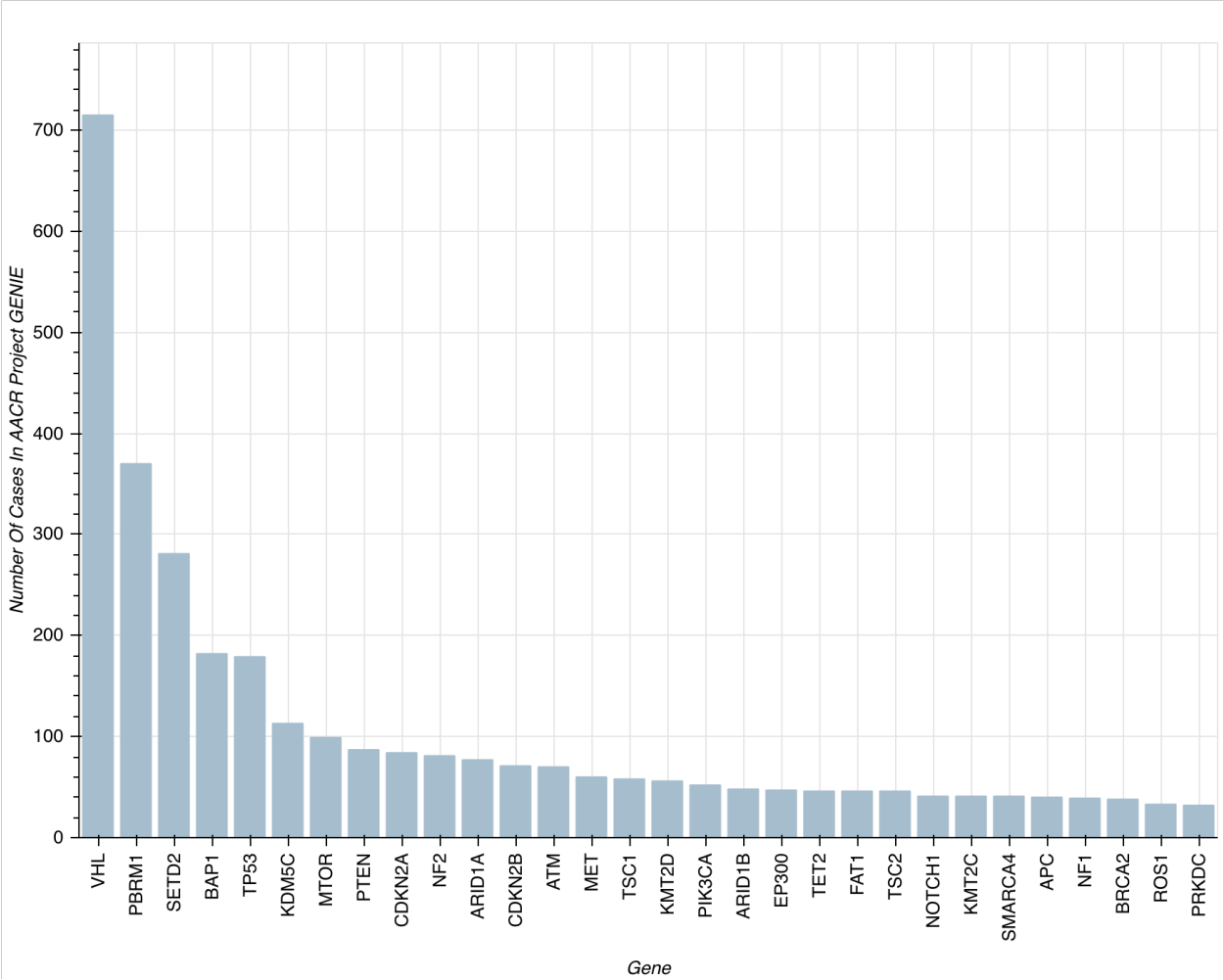

Figure 3. Most commonly altered genes in clear cell renal cell carcinoma

Genes located on the short arm of chromosome 3 are the most commonly mutated genes in, including *VHL, PBRM1, SETD2,* and *BAP1*. Adapted from mycancergenome.org

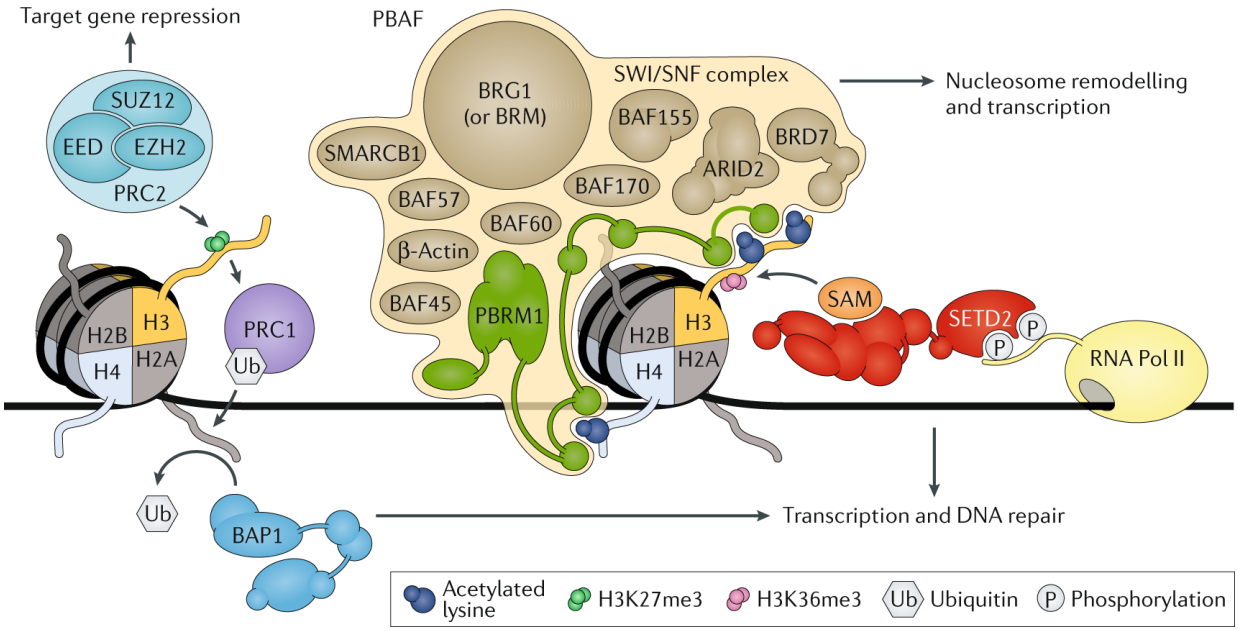

Figure 4. BAP1, PBRM1, and SETD2 chromatin modification activities

The switch/sucrose nonfermentable (SWI/SNF) chromatin remodeling complex — shown here as polybromo-associated BRG1-associated factor (PBAF) — comprises >11 subunits, including a catalytic core subunit (protein brahma homologue (BRM) or transcription activator BRG1), accessory subunits (β-actin, SWI/SNF-related matrix-associated actin-dependent regulator of chromatin subfamily B member 1 (SMARCB1), BRG1-associated factor 45 (BAF45), BAF57, BAF60, BAF155, and BAF170), and DNA-binding subunits (AT-rich interactive domain-containing protein 2 (ARID2), bromodomain-containing protein 7 (BRD7), and protein polybromo 1 (PBRM1), or alternatively, ARID1A and ARID1B). PBRM1 contains six bromodomains that mediate DNA targeting by binding acetylated histone residues. Histone-lysine *N*-methyltransferase SETD2 associates with hyperphosphorylated RNA polymerase II (RNA Pol II) and deposits the histone H3 lysine 36 trimethyl mark (H3K36me3) as it travels along with RNA Pol II during transcription; SETD2 uses S-adenosyl-L-methionine (SAM) as a one-carbon donor during methylation. Consequently, SETD2 deposits the H3K36me3 mark

primarily on exons of actively transcribed genes. Thus, SETD2 and its associated mark (H3K36me3) are involved in regulating transcription and mediating DNA damage repair. Polycomb repressive complex 1 (PRC1) and PRC2 are responsible for regulating cellular differentiation and lineage commitment and maintenance via transcriptional repression of target genes. PRC2, comprising Polycomb protein SUZ12, Polycomb protein EED, and histone-lysine N-methyltransferases EZH1 or EZH2, catalyzes the addition of the trimethyl mark on lysine 27 of histone H3 (H3K27me3), a mark that is associated with gene silencing. Canonically, H3K27me3 subsequently recruits PRC1 to reinforce gene repression through monoubiquitylation of lysine 119 on histone H2A (H2AK119ub1). PRC1 activity can be reversed by ubiquitin carboxyl-terminal hydrolase BAP1, a deubiquitinase that catalyzes the deubiquitylation of H2AK119ub1. BAP1-mediated deubiquitylation of H2AK119ub1 has important roles in regulating transcription and mediating DNA damage repair. The figure and caption were reproduced and adapted with permission[48]; permission conveyed through Copyright Clearance Center.

PI3K-AKT-mTOR

Phosphoinositide 3-kinase (PI3K) is the most frequently activated signaling pathway in cancer[62]. Although not frequently mutated in ccRCC, downstream activation of the PI3K signaling pathway is elevated in ccRCC patients[63–67]. Humans encode multiple isoforms of this lipid kinase, which is divided into the following classes: Ia, Ib, II, and III[68–70]. Studies have focused on Class Ia, as this is the main isoform implicated in cancer[71]. Class Ia PI3K is composed of a p110 catalytic subunit and a p85 regulatory subunit that keeps PI3K in an inactive form in the cytosol [68–70]. The three Class Ia p110 catalytic subunits are α, β, δ, which are encoded by PIK3CA, PIK3CB, and PIK3CD, respectively.

PI3K is activated by a variety of different signals, including epidermal growth factor (EGF), platelet-derived growth factor (PDGF), VEGF, insulin, and others[68,69]. Following activation of a growth factor receptor, the Src homology 2 (SH2) domains on the p85 regulatory subunit will associate with the phosphorylated tyrosine residues on the growth factor receptor [Figure 5]. This interaction will disinhibit p110, which is now in close proximity to the cell membrane. p110α and p110δ have a Ras Binding Domain (RBD) that binds to Ras or R-ras family members, whereas p110β's RBD binds to the Rho family of GTPases Rac/cdc42, which regulate actin cytoskeleton dynamics[72]. In addition, unlike the other p110 subunits, p110β can become activated by interacting with the G-protein βγ via G-coupled protein receptor signaling[73].

PI3K phosphorylates phosphatidylinositol-4,5-bisphosphate (PtdIns-4,5-P_2) to phosphatidylinositol-3,4,5-trisphosphate (PtdIns-3,4,5-P_3) within seconds of growth factor stimulation[74]. This activity is under tight control and is opposed by Phosphatase and tensin homolog (PTEN), the second most common tumor suppressor gene mutated in cancer[75,76].

PtdIns-3,4,5-P_3 then acts as a second messenger to activate downstream targets that contain a pleckstrin homology (PH) domain, such as AKT (also known as protein kinase B) and phosphoinositide-dependent kinase 1 (PDK1)[69,70,77]. AKT and PDK1 are recruited to the cell membrane, and binding of AKT to PtdIns-3,4,5-P_3 induces a conformational change, allowing phosphorylation of threonine 308 by PDK1 and serine 473 by mammalian target of rapamycin complex 2 (mTORC2)[78]. Phosphorylation of these residues is essential for full activation of AKT's kinase activity[79] [Figure 5]. AKT in turn serves as a serine and threonine kinase with over 100 substrates involved in diverse processes from cell cycle regulation to metabolism to vesicle trafficking[78,80]. Some of its most well studied targets include negative regulators of mTORC1, such as tuberous sclerosis complex 2 (TSC2) and proline-rich AKT substrate of 40 kilodaltons (PRAS40)[80,81]. Phosphorylation of TSC2 leads to activation of Ras homolog enriched in brain (RHEB), which turns on mTORC1[81]. mTORC1 will phosphorylate 4E-binding protein 1 (4EBP1) and ribosomal protein S6 kinase, inducing protein translation, cell proliferation, and angiogenesis[82] [Figure 5].

In ccRCC, there is considerable crosstalk between the HIF signaling and PI3K/AKT/mTOR signaling pathways. As described previously, HIF signaling increases the expression of growth factors such as PDGF, EGF, and VEGF. These growth factors, through autocrine and paracrine signaling, activate the PI3K/AKT/mTOR pathway as described above. mTORC1 and 2 are known to increase the translation of HIF-1 mRNA transcripts[83,84]. Thus, the HIF and PI3K/AKT/mTOR signaling pathways are closely linked and play critical roles in ccRCC.

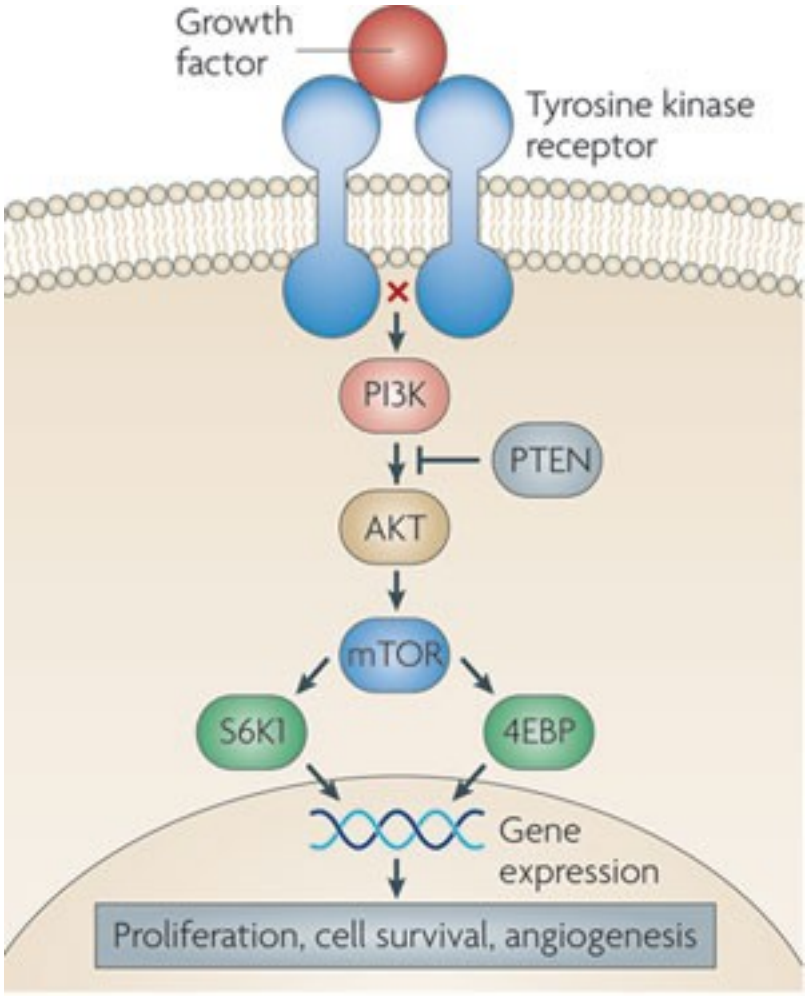

Figure 5. PI3K-AKT-mTOR signaling axis

Activation of a tyrosine kinase receptor by a growth factor leads to PI3K localizing to the cell membrane where it can phosphorylate PtdIns-4,5-P_2 to PtdIns-3,4,5-P_3. PtdIns-3,4,5-P_3 subsequently activates downstream AKT and mTOR signaling, promoting proliferation, cell survival, and angiogenesis. PTEN turns this pathway off by dephosphorylating PtdIns-3,4,5-P_3. The figure was reproduced and adapted with permission[85]; permission conveyed through Copyright Clearance Center.

Metabolic Reprogramming in Clear Cell Renal Cell Carcinoma

Metabolism is central to all cellular processes, and one emerging hallmark of cancer is the deregulation of cellular energetics[86]. Normally, cells use glucose to generate pyruvate, which undergoes oxidative metabolism in the mitochondria. In the 1920s, Otto Warburg hypothesized that cancer cells utilize glucose for glycolysis even in the presence of oxygen, which was termed aerobic glycolysis or the Warburg effect[87]. It is postulated that the metabolic shift to aerobic glycolysis supports cancer cells by re-directing nutrients for the biosynthesis of macromolecules and organelles needed for rapid growth and proliferation[88].

The clear cell phenotype of ccRCC derives its name from the fact that these cells accumulate glycogen and lipids, pointing to metabolic derangements in this cancer subtype[89–91]. Unsurprisingly, some of the most well characterized downstream targets of HIF are genes involved in cellular metabolism [Figure 6]. Although HIF-1α is thought to primarily mediate transcription of glycolytic genes, whereas HIF-2α is thought to be more involved with lipid metabolism and activating Myc and mTOR signaling, ChIP-seq studies revealed that there is considerable overlap in the metabolic genes controlled by both HIF isoforms[92–94]. Moreover, TCGA analysis demonstrated that metabolic shifts away from oxidative phosphorylation and toward aerobic glycolysis, fatty acid synthesis, and the pentose phosphate pathway were associated with high stage and low survival in ccRCC tumors[14]. These changes, which are described in more detail in the following subsections, illustrate that ccRCC undergoes advantageous metabolic adaptations that permits growth and survival in nutrient-deplete environments.

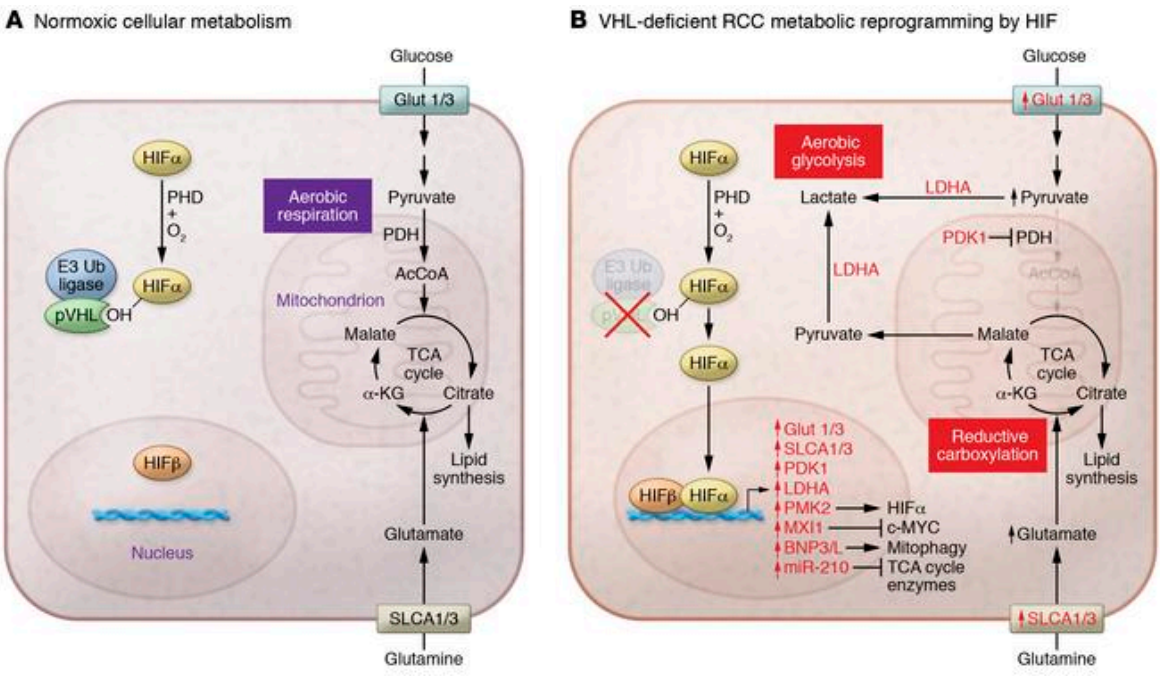

Figure 6. HIF mediates metabolic reprogramming in VHL-deficient RCC

Mutations that render the tumor suppressor gene VHL defective, as observed in a majority of clear cell renal carcinoma cells (ccRCC), interfere with VHL-mediated proteolysis of HIFα (compare a classic model of cellular metabolism in **A** with pseudohypoxic HIF-driven RCC metabolic reprogramming in **B**). Stabilized HIFα translocates to the nucleus, where it dimerizes with HIFβ and directly upregulates transcription of genes related to cellular metabolism, among hundreds of others. HIF reprograms metabolism away from aerobic respiration and toward aerobic glycolysis by increasing conversion from pyruvate to lactate (via upregulation of LDHA) and by blocking pyruvate conversion to acetyl-CoA by PDH (via upregulation of PDK1). HIF increases metabolic nutrients by upregulating transporters for both glucose (GLUT1 and GLUT3) and glutamine (SLCA1 and SLCA3), thereby increasing rates of glycolytic and reductive carboxylation pathways, respectively. In addition, HIF mediates a reduction in aerobic respiration by upregulating BNIP3 and BNIP3L, which leads

to selective mitochondrial degradation. HIF interferes with TCA cycle enzymes via miR-210, which disrupts formation of Fe-S clusters necessary for catalysis. Upregulation of the transcription suppressor MXI1 represses c-MYC expression that greatly facilitates the metabolic shift in cancer cells. HIF amplifies its own transcriptional activity by upregulating the HIFα cofactor PKM2. Ub, ubiquitin. α-KG, α-ketoglutarate. The figure and caption were reproduced and adapted with permission[95]; permission conveyed through Copyright Clearance Center.

Aerobic glycolysis is highly active in ccRCC

Due to the increase in HIF signaling as a result of *VHL* loss, ccRCC tumors display increased expression of Glut1, hexokinase-2 (HK-2), glyceraldehyde-3-phosphate dehydrogenase (GAPDH), lactate dehydrogenase-A (LDH-A), and pyruvate dehydrogenase kinase, which inactivates pyruvate dehydrogenase and thus impedes oxidative metabolism of pyruvate in the TCA cycle[14]. Chan *et al.* demonstrated a synthetic lethal interaction between *VHL* loss and GLUT1 inhibitors *in vitro* and *in vivo*, highlighting ccRCC's dependence on glycolysis[96]. Data from metabolomic studies performed in ccRCC are consistent with this finding. These studies demonstrate an increase in glycolytic intermediates, such as glucose-6-phosphate, fructose-6-phosphate, and lactate, with a concomitant a decrease in TCA metabolites in ccRCC[97,98]. In fact, pyruvate carboxylase, which converts pyruvate to oxaloacetate to fuel the TCA cycle, was found to be downregulated ccRCC tumors[98]. Furthermore, fructose-bisphosphatase (FBP), which opposes the activity of phosphofructokinase in glycolysis, was found to be depleted in 600 ccRCC tumor samples and correlated with higher stage and worse prognosis[99]. FBP inhibits ccRCC progression in two ways: reducing glycolytic flux as well as inhibiting HIF-1α and HIF-2α in the nucleus by interacting with their C-terminal domain[99]. These data suggest that ccRCC tumor cells preferentially use glucose for lactate fermentation instead of TCA cycle metabolism.

Glutamine addiction in ccRCC

Glutamine consumption is elevated in ccRCC[100]. Glutamine is converted to glutamate by the enzyme glutaminase (GLS). Glutamate is one of three amino acids required to produce the antioxidant glutathione to curb reactive oxygen species (ROS) levels, and it was reported that

glutamate-dependent formation of glutathione was elevated in ccRCC tumors with higher grades[98]. Further support of glutamate's important role in glutathione formation in ccRCC comes from the observation that inhibition of GLS with the drug CB-839 in ccRCC cells led to increased ROS[100] as well as reduced ccRCC xenograft growth[101,102]. Consequently, glutamine is a critical nutrient for ccRCC tumorigenesis, and multiple GLS inhibitors are currently being studied in clinical trials to exploit this weakness in ccRCC and other tumor types[103].

Another pathway for glutamine is conversion to α-ketoglutarate. α-ketoglutarate can subsequently form several metabolites, including the oncometabolite 2-hydroxyglutarate (2-HG), which alters the epigenome by antagonizing 2-oxyglutarate-dependent dioxygenases[104]. α-ketoglutarate can also be converted to citrate by reductive carboxylation. This reaction is promoted by HIF in *VHL*-deficient ccRCC cells by keeping intracellular citrate levels low[101,105], and consistent with this phenomenon, citrate levels were found to be decreased in late stage ccRCC tumors[97]. Citrate will subsequently be converted to acetyl-CoA, fueling lipogenesis[106] as described in the next section.

Fatty acid synthesis in ccRCC

Lipid accumulation in ccRCC tumors compared to normal kidney tissue was described as early as 1987[107]. Consistent with this initial observation, subsequent studies reported that fatty acid synthase expression correlates with tumor aggressiveness and poor survival[108]. Furthermore, expression of stearoyl-CoA desaturase 1, which mediates monounsaturated fatty acid biosynthesis, is elevated in all stages of ccRCC, and inhibition of this enzyme reduced tumor cell growth and promoted cell death *in vitro* and *in vivo*[109]. In addition, carnitine palmitoyltransferase 1A (*CPT1A)* expression was found to be suppressed by HIF1 and HIF2 in ccRCC[110]. Reduced

CPT1A expression led to the shunting of fatty acids from mitochondria into lipid droplets for storage and correlated with poor patient outcomes[110]. Finally, metabolomics and proteomics studies of ccRCC show decreased levels of β-oxidation enzymes[98,111] as well as increased levels of long chain fatty acids[97]. Together, these findings indicate upregulation of fatty acid synthesis and lipid storage and downregulation of β-oxidation in ccRCC.

Current Therapies for Advanced Clear Cell Renal Cell Carcinoma

Cytokine therapies

Metastatic renal cell carcinoma is historically known to be resistant to traditional chemotherapy. Elucidation of the fundamental genomic and molecular characteristics of ccRCC have revolutionized the treatment landscape of ccRCC [Figure 7]. Cytokine immunotherapy with interferon-α (IFN-α) and high dose IL-2 was used in the 1990s to activate antitumor immunity. Patients treated with high dose IL-2 had a 25% response rate and showed durable responses[112], whereas IFN-α had a 10-15% response rate and a median overall survival of 13 months[113]. Unfortunately, due to severe systemic toxicity associated with these cytokines, their utility was limited because patients had to receive treatment at a facility with the appropriate expertise. Consequently, there was heightened interest in developing targeted therapies for ccRCC.

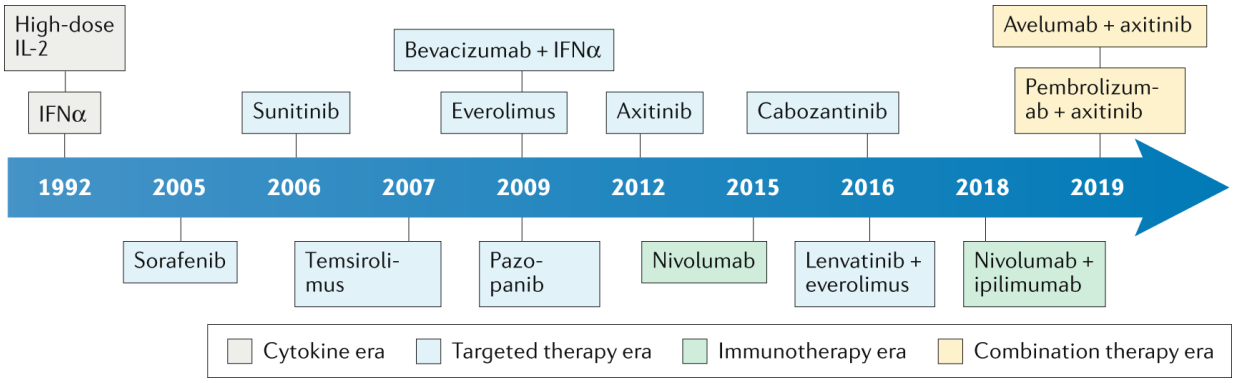

Figure 7. Development of ccRCC treatments timeline

Since the 2000s, cytokine therapies that were used to treat metastatic clear cell renal cell carcinoma, such as IFNα and IL-2, have been largely supplanted by targeted therapies directed at VEGFRs and mTOR. New inhibitors with improved specificity for VEGFR (for example, Axitinib) were subsequently developed, as well as multi-kinase inhibitors. Cabozantinib, for example, targets the MET receptor tyrosine kinase encoded by *MET* and the tyrosine protein kinase receptor UFO encoded by *AXL*, whereas Lenvatinib targets include VEGFRs and fibroblast growth factor receptors. Nivolumab, which prevents signaling through programmed cell death 1 (PD-1), was the first immunotherapy agent approved for RCC. The combination of Nivolumab and Ipilimumab, which inhibits cytotoxic T lymphocyte-associated protein 4 (CTLA4), was subsequently shown to improve patient survival and became the standard of care first-line treatment for patients with intermediate and high-risk RCC. The latest combination therapy regimens include agents that target VEGF and immune checkpoints such as Axitinib–Avelumab and Axitinib–Pembrolizumab, which target VEGFR in combination with PD-1 ligand 1 (PD-L1) and PD-1, respectively. The figure and caption were reproduced and adapted with permission[114]; permission conveyed through Copyright Clearance Center.

Targeted therapies

Elucidation of the pro-angiogenic effects of *VHL* loss spurred the development of anti-VEGFR inhibitors. In 2005, Sorafenib became the first anti-angiogenic tyrosine kinase inhibitor (TKI) targeting VEGFR to be approved, ushering in the targeted therapy era. Newer generations of anti-angiogenic TKIs were developed, and Sunitinib soon replaced Sorafenib and was shown to prolong progression-free survival and improve response rates compared to IFN-α[115]. Sunitinib is known to target multiple tyrosine kinases in addition to VEGFR such as c-KIT and platelet derived growth factor receptor. Bevacizumab, a monoclonal antibody that targets VEGF, was approved in combination with IFN-α[116], but has since fallen out of favor. TKIs more specific for VEGFR (such as Axitinib[117,118]), with fewer side effects (such as Pazopanib[119]), and that inhibit other receptors implicated in resistance (such as Cabozantinib that also targets AXL and MET[120]) have since been approved. In addition, mTOR inhibitors like Everolimus and Temsirolimus were approved in 2009 for ccRCC. However, resistance to these agents is nearly universal, with the majority of patients developing resistance six to fifteen months after starting treatment[121].

Immune checkpoint blockade

The introduction of immune checkpoint blockade (ICB) has revolutionized cancer treatment, especially in ccRCC[122]. These agents target inhibitory T cell receptors such as cytotoxic T lymphocyte associated protein-4 (CTLA-4) and programmed cell death protein 1 (PD-1) to reinvigorate these immune cells to attack tumor cells. Even though ccRCC doesn't have a high mutational burden, which is usually a positive predicative marker for response to ICB, ccRCC is known to be an immunogenic tumor that is highly infiltrated with cytotoxic T cells[123]. As described above, the cytokine treatments for ccRCC, IFN-α and high dose IL-2, were

the first evidence that activating the immune system could lead to durable responses in ccRCC patients. In 2015, Nivolumab, a monoclonal antibody targeting PD-1, was approved in the second-line setting for metastatic ccRCC. Patients on Nivolumab showed greater response rate and longer median overall survival compared to Everolimus[124]. Patients on combination Nivolumab and Ipilimumab, which inhibits CTLA-4, showed an increased response rate, including a 9% complete response rate, compared to Sunitinib in previously untreated advanced RCC.

More recently, combination anti-angiogenic TKIs with ICB have been approved for first-line treatment in advanced RCC. This combination was shown to prolong overall survival and improve objective response rates in four clinical trials testing this combination (Avelumab plus Axitinib[125], Pembrolizumab plus Axitinib[126], Pembrolizumab plus Lenvatinib[127], and Nivolumab plus Cabozantinib[128]), compared to Sunitinib monotherapy. One possible reason that this combination is effective is VEGFR inhibitors are known to induce vascular normalization, which paradoxically improves blood flow and thus immune infiltration into a tumor[129]. In addition, VEGF has been shown to mediate immune suppression by activating myeloid derived suppressor cells (MDSCs) and regulatory T cells[130]. As combination anti-angiogenic TKIs with ICB regimens replace Sunitinib as standard of care, future clinical trials will have to compare effects of new treatment options to this new baseline regimen.

Summary and Thesis Projects

ccRCC is characterized by loss of the VHL protein, leading to activation of HIF signaling and metabolic alterations. Our improved understanding of the molecular biology and heterogeneity underlying ccRCC has provided the framework for new studies to translate these findings into novel therapeutic strategies. Chapter II reviews the metabolism of cancer and immune cells and the metabolic barriers to immune function and immunotherapy efficacy in cancer. In Chapter III, we discuss our discovery of a synthetic lethal interaction between *SETD2* loss and PI3Kβ inhibition. We found that PI3Kβ inhibitors can inhibit growth of SETD2-deficient ccRCC cells *in vitro* and *in vivo,* suggesting that the ~15% of ccRCC patients harboring *SETD2* mutations could benefit from PI3Kβ-specific inhibitors. We then shift gears in Chapter IV, which provides an overview of the current literature on emerging players in intercellular communication in cancer: extracellular vesicles. This is followed by a chapter on our discovery that anti-angiogenic TKIs increase the secretion and glycolytic activity of sEVs in ccRCC, indicating that these bioactive vesicles could be impacting the metabolic composition of the tumor microenvironment. Finally, the last chapter of this dissertation summarizes these findings and presents the remaining questions for the field to tackle.

CHAPTER II

THE TUMOR MICROENVIRONMENT AS A METABOLIC BARRIER TO EFFECTOR T CELLS AND IMMUNOTHERAPY

Aaron R. Lim[1], W. Kimryn Rathmell[1,2,3], Jeffrey C. Rathmell[2,3,4]

[1]Department of Medicine, Division of Hematology and Oncology, Vanderbilt University Medical Center, Nashville, TN 37232, [2]Vanderbilt-Ingram Cancer Center, Vanderbilt University Medical Center, Nashville, TN 37232, [3]Vanderbilt Center for Immunobiology, Vanderbilt University Medical Center, Nashville, TN 37232, [4]Department of Pathology, Microbiology, and Immunology, Vanderbilt University Medical Center, Nashville, TN 37232

The work presented in this section is published in *eLife*[131] and has been reproduced with the permission of the journal and my co-authors.

Abstract

Recent breakthroughs in our understanding of the role of T cells in anti-tumor immunity have led to unprecedented advances in immunotherapy. However, a great majority of cancer patients will not respond to these treatments as tumors and the tumor microenvironment (TME) restrain immunity. It is now clear that T cells must substantially increase their nutrient uptake to mount a proper immune response. Each T cell functional population utilizes a distinct metabolic

program that supports the differentiation and activity of those cells. Failure to obtain sufficient nutrients or engage the appropriate metabolic pathways can alter or prevent effector T cell differentiation and function. The TME, however, can be metabolically hostile to these functions due to insufficient vascular exchange and cancer cell metabolism that leads to hypoxia, depletion of nutrients, and accumulation of waste products. Further, cancer cells themselves can express inhibitory receptors that inhibit T cell metabolism and can alter T cell signaling through release of extracellular vesicles such as exosomes. Together, these aspects of the TME can impose metabolic barriers to anti-tumor immunity. This review will discuss the metabolic changes that drive T cells into different stages of their development and how the TME influences the metabolism and activity of tumor infiltrating lymphocytes.

Introduction

Hanahan and Weinberg's seminal paper "The Hallmarks of Cancer" was revised in 2011 to include deregulating cellular energetics and evasion of immune destruction[86]. Tumors fuel their rapid growth and proliferation with aerobic glycolysis, a process initially described by Otto Warburg in which cells undergo glycolysis even in the presence of oxygen[132]. Although less energetically efficient than oxidation that occurs in most mature tissues, aerobic glycolysis shuttles intermediates into biosynthetic pathways to make amino acids, nucleotides, fatty acids and other macromolecules to support rapid anabolic growth[133]. As a consequence, glucose and amino acids can be rapidly consumed while waste products accumulate. Activated T cells also undergo a metabolic switch from oxidative metabolism to aerobic glycolysis to proliferate and develop effector function[134,135]. Rapid proliferation and acquisition of effector function are

demanding processes that require precise metabolic re-wiring. Failure of activated T cells to undergo metabolic re-wiring impairs effector function[136]. As T cell metabolism dictates effector function, it is now apparent that the effect of cancer cell metabolism on the tumor microenvironment (TME) may impair anti-tumor immunity, and these new hallmarks of cancer are therefore inextricably linked.

Expanded understanding of the basic biology of T cell activation has enabled immunotherapy to combat cancer, and T cell metabolism now offers the opportunity to optimize and improve these therapeutic strategies. Two of the primary immunotherapies are immune checkpoint blockade (ICB) and adoptive cell transfer (ACT). ICB is based on the use of antibodies to neutralize inhibitory immune receptors such as CTLA-4 or PD-1 to reinvigorate T cells[137]. In contrast, ACT expands a patient's own T cells *ex vivo* to direct anti-tumor immunity when transfused back into the patient. These treatment modalities have shown great promise in many types of cancer and even produce long-lasting responses in some patients[138]. However, many patients fail to respond to these therapies, and metabolic barriers imposed on T cells by the TME may contribute. This review will discuss the metabolic adaptations necessary for T cells to meet changing biochemical needs throughout different stages of differentiation. We will then examine how tumor cells create a toxic milieu for T cells that enter the TME. Finally, we will provide an overview of how utilizing an understanding of T cell metabolism may inform strategies to alter the TME or enhance T cell metabolism to strengthen the immunotherapy arsenal.

Metabolic Reprogramming of T Cells

There is a growing appreciation that distinct metabolic programs drive different developmental stages of a T cell throughout its lifespan [Figure 8]. After leaving the thymus, naïve T cells utilize a catabolic metabolism in which small amounts of glucose are used to generate ATP mainly through oxidative phosphorylation to support immune surveillance[139,140]. To proliferate and gain effector function, stimulated T cells must undergo rapid metabolic reprogramming and switch to aerobic glycolysis to support anabolic metabolism and exit quiescence[139,140]. Although fewer ATP molecules are generated per glucose molecule, aerobic glycolysis allows T cells to build substrates needed for growth and proliferation and is essential for effector differentiation[134]. Metabolic reprogramming from catabolism to anabolism is initiated upon T Cell Receptor (TCR) recognition of cognate antigen presented on major histocompatibility complex (MHC) and with the help of CD28-mediated co-stimulation. TCRs cluster and signal to the phosphatidtyl-inositide-3 kinase (PI3K)/AKT/mTORC1 pathway to upregulate nutrient uptake, glycolysis and, to a lesser extent, oxidative phosphorylation[141,142]. T cell metabolism is further re-wired by transcription factors such as c-Myc and hypoxia inducible factors (HIFs), which transcribe genes essential for T cell activation and regulate glycolysis and glutaminolysis[143,144]. Importantly, limiting glucose availability or inhibiting glycolytic enzymes impairs effector T cell proliferation and cytokine production[145–147]. Increased amino acid uptake is also essential, and deficiency of glutamine, neutral amino, or essential amino acid transporters can impair effector T cell development[148–151]. While glutamine uptake itself is required for T cell activation, glutamine metabolism appears to play a complex role, as glutaminolysis can suppress effector T cell differentiation and function[151,152]. In addition to these pathways, mitochondria undergo physical and functional changes required for efficient T cell activation. T cell activation with CD28 co-stimulation leads to mitochondrial fragmentation that can reduce oxidative

efficiency in effector T cells[153], although CD28 co-stimulation increased respiration under glucose limiting conditions[142]. This distinction may be due to findings that CD28 co-stimulation can increase T cells spare respiratory capacity and remodel cristae, allowing memory T cells to manage metabolic stress and quickly to future stimuli[154]. The mitochondria of T lymphocytes also undergo significant proteomic changes that favor one-carbon metabolism critical for nucleotide synthesis, methylation, and redox balance in T cell activation[155]. Meanwhile, mitochondrial reactive oxygen species (ROS) production promotes nuclear factor of activated T cells (NFAT) activation and IL-2 production[141].

Although most of our understanding of T cell metabolism comes from *in vitro* or *ex vivo* studies, the question of whether this translates *in vivo* has been understudied. A recent study by Ma *et al.* compared $CD8^+$ T cell metabolism *in vivo* versus *in vitro* by tracing glucose metabolism with ^{13}C-glucose IV infusions in a listeria monocytogenes infection mouse model[156]. Their results showed that $CD8^+$ T cells *in situ* had reduced lactate production and higher rates of oxidative metabolism and serine metabolism compared to *in vitro* $CD8^+$ T cells that adopted a metabolic phenotype consistent with the Warburg effect[156]. The environment may contribute to these metabolic differences, since *in vitro* conditions often supply high amounts of glucose. Indeed, when the *in vivo* effector T cells were cultured in the same *in vitro* media conditions, the cells secreted more lactate[156]. These data suggest that T cells *in vivo* utilize glucose primarily as an anabolic source with alternate fuels such as glutamine supporting ATP, whereas glucose may play a broader anabolic and energetic role *in vitro* that would necessitate higher glucose flux and subsequent lactate production to maintain redox balance. Re-assessing the nutrients *in vitro* cultures of T cells to better reflect *in vivo* conditions is necessary to more precisely study T cell metabolism under a variety of contexts such as cancer.

Long-lived memory T cells that form after the induction of an immune response also have distinct metabolic features. Unlike activated T lymphocytes, memory T cells have low mTOR signaling and high AMPK signaling, promoting fatty acid oxidation[157,158]. To support this state, memory T cells increase their uptake of glycerol, which is used to synthesize fatty acids that subsequently fuel fatty acid oxidation[159]. In contrast to naïve or activated T cells, memory T cells have more mitochondrial mass and mitochondrial spare respiratory capacity[160] and are poised to rapidly induce aerobic glycolysis[161,162]. This unique metabolic program allows memory T cells to quickly respond upon encountering the cognate antigen[163]. However, when effector T cells cannot effectively clear antigens such as during chronic infection or cancer, they may not form memory T cells and instead may become exhausted[164]. Exhausted T cells are a distinct class of T lymphocytes characterized by lower proliferative capacity, survival, and cytokine production. They also express different transcription factors and high amounts of inhibitory receptors such as PD-1, leading to metabolic re-wiring[165]. In particular, PD-1 signaling promotes the switch from glycolysis to fatty acid oxidation by suppressing AKT and mTOR activity[166]. These functionally impaired T cells also have impaired mitochondria[167], and improving mitochondrial function with anti-oxidants restored T cell activity[168]. In addition, overexpression of peroxisome proliferator-activated receptor-γ coactivator (PGC-1α) increased glucose uptake and decreased mitochondrial mass and polarization, and it enhances the function of exhausted T cells in both a lymphocytic choriomeningitis virus (LCMV) infection[169] and in a B16 melanoma model[170]. Overall, T cells must adapt their metabolism to fuel a program that meets their changing needs at different activation, functional, and microenvironmental stages.

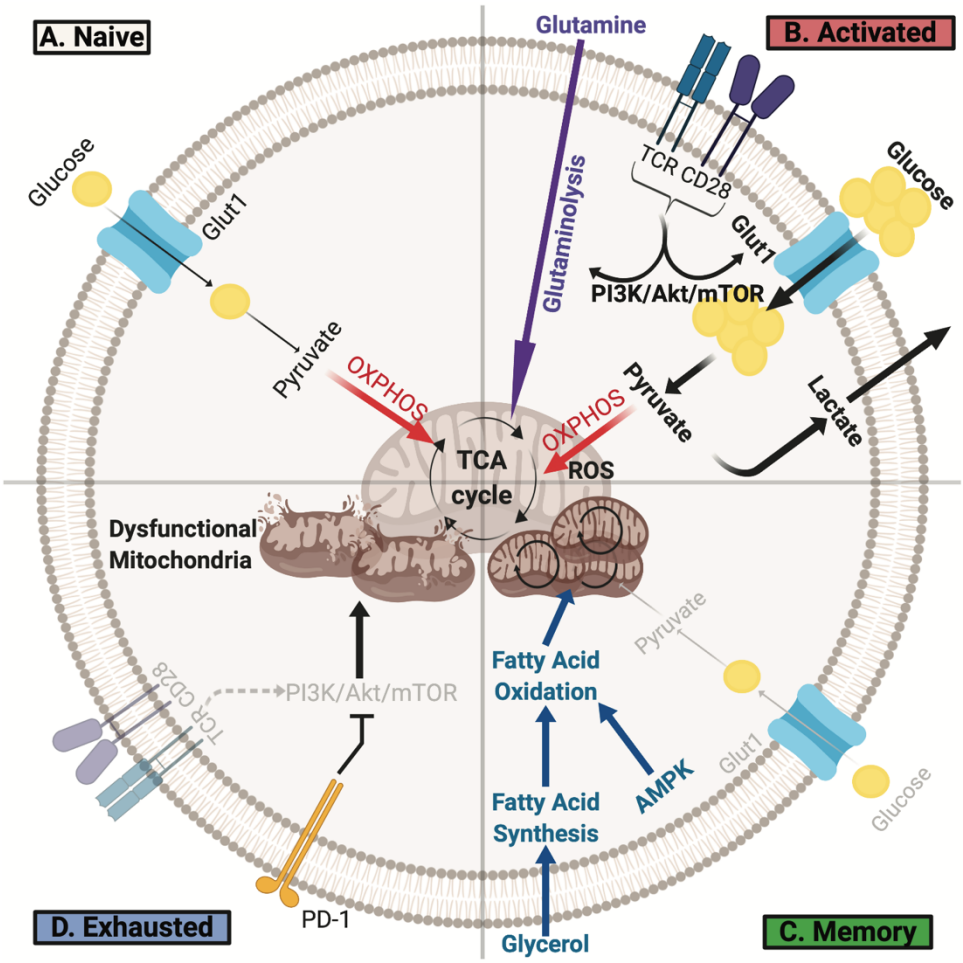

Figure 8. T cells undergo metabolic rewiring in different stages of their life

(A) Naïve T cells uptake sufficient amounts of glucose to fuel oxidative phosphorylation and survive as they survey antigens. (B) Upon encountering cognate antigen, activated T cells rapidly uptake glucose and glutamine to fuel their bioenergetic needs. Activated T cells perform aerobic glycolysis, which shunts products of glycolysis to biosynthetic processes necessary for proliferation and effector function and generates lactate as a byproduct. (C) Once the antigen is cleared, T cells can form long-lived memory cells in which AMPK signaling stimulates fatty acid oxidation. Memory T cells also increase their mitochondrial mass and spare respiratory capacity to prepare for future encounter with cognate antigen. (D) T cells can

become exhausted if they fail to clear antigens such as during chronic infections or cancer. T lymphocytes isolated from tumors display elevated levels of PD-1, which decreases PI3K/Akt/mTOR signaling and glycolysis. Exhausted TILs rely on fatty acid oxidation, though they often have dysfunctional mitochondria and decreased mitochondrial mass as well.

T Cells Encounter a Hostile Metabolic Environment in Tumors

T cells isolated from tumors often show signs of exhaustion and have distinct metabolic signatures[123,170]. For example, tumor-infiltrating lymphocytes (TILs) isolated from clear cell renal cell carcinoma patients show decreased glucose uptake as well as small, fragmented mitochondria with elevated ROS[123]. Bypassing these metabolic defects by supplementing with pyruvate or adding ROS scavengers partially restored TIL activation[123]. TILs in a murine melanoma model have also been shown to have dysfunctional enolase[171] and reduced mitochondria biogenesis[170], and tumor-associated lactate and cholesterol suppress TIL function[172,173]. In addition, TILs can infiltrate sarcoma tumors but do not produce cytokines until after checkpoint blockade[174]. These studies suggest that antigen recognition and infiltration into tumors alone are insufficient for an antitumor response, and that the tumor metabolic microenvironment can directly suppress T cells.

Hypoxia

T cells are primed in nutrient-rich lymphoid tissues but enter tumors where cancer cell metabolism and poor vascular exchange may lead to a fierce competition for resources. One hostile aspect of the TME that infiltrating T cells encounter is hypoxia, created by the high metabolic rate of tumor cells in conjunction with inadequate vasculature. Cancer cells can adapt to thrive under low oxygen conditions, and several studies have shown the association of hypoxia with angiogenesis, metastasis, and chemoresistance[175,176]. Under low oxygen states, the transcription factor hypoxia-inducible factor (HIF) is free from its negative regulator von Hippel-Lindau (VHL) to upregulate its target genes[177]. Studies have begun to show how hypoxia can

lead to metabolic dysfunction in T cells, though it still remains a complex subject. There are studies that suggest hypoxia can have an immunostimulatory effect on T cells in the TME. For example, lack of oxygen stabilizes HIF-1α, which increases pyruvate dehydrogenase kinase and lactate dehydrogenase A expression and thus decreases oxidative phosphorylation[178,179]. Hypoxic $CD8^+$ T cells increase granzyme B packaging into granules and reject B16 tumors in mice more efficiently than normoxic T cells[180], and loss of HIF-1α, but not HIF-2α, inhibited the activity and migration of OT-I T cells and enhanced tumorigenesis[144]. In contrast, other studies indicate an immunosuppressive role for hypoxia. For example, HIF-1α is known to upregulate PD-L1 on myeloid-derived suppressor cells (MDSCs), which leads to T cell exhaustion, and can promote the generation of regulatory T cells[181–183]. Highly oxidative cancer cells can lead to areas of hypoxia, and this has been associated with decreased T cell response to ICB[150]. Indeed, T cells have been shown to avoid areas of hypoxia in the TME, but mice breathing 60% oxygen displayed enhanced CD8 T cell infiltration into the TME and increased tumor regression and survival in multiple tumor models[184]. These studies underscore that there is likely a fine balance with HIF-1α expression in TILs that can later their function in the TME. Further investigation is warranted to tease out the effects of hypoxia in the TME.

Nutrient competition and metabolic byproducts

Consistent with both cancer cells and effector T cells utilizing aerobic glycolysis in tumor microenvironments that can have poor vascular exchange, evidence supports competition for available nutrients that can impair TILs [

Table 1]. Indeed, intratumor glucose levels have been measured and can be significantly reduced in some settings[170,185], although glucose levels can remain unchanged in others[123].

Cancer cells may contribute to reduced glucose availability as rapid glucose consumption by mouse sarcoma cells was found to restrict the effector function of TILs and thus permitted tumor progression[186]. Tumor regression and TIL function were inversely associated with the capacity of sarcoma cells to perform aerobic glycolysis. Another study found that culturing T lymphocytes in conditioned media from ovarian cancer cells decreased expression of the methyltransferase EZH2 in T cells and their polyfunctionality, and these effects were abrogated upon glucose supplementation[187]. In addition, treating human ovarian cancer-specific T cells with an EZH2 inhibitor prior to adoptive transfer led to increased tumor growth in a humanized ovarian cancer mouse model[187]. These data suggest that glucose metabolism can regulate T cell polyfunctionality by modulating EZH2 expression, although whether one should induce EZH2 expression in cancer patients is complicated since some cancers acquire gain-of-function mutations in this methyltransferase[188]. It would be interesting to test whether inducing EZH2 expression in adoptively transferred T cells could overcome the effects of glucose deprivation in the TME. Insufficient glucose in tumors may also impair T cell signaling to restrain anti-tumor immunity through a phosphoenolpyruvate-dependent regulation of calcium signaling[185]. Collectively, these studies highlight the importance of glucose in the TME for T cell function.

In addition to potential limitations to available glucose, other nutrients may also become limiting in context specific manners. A mass spectrometry-based analyses of institutional fluid from a pancreatic ductal carcinoma mouse model showed depletion of some essential and branch chain amino acids, while others were enriched in the tumor microenvironment[189]. Importantly, the tumor location, diet, and cancer type could shift the metabolic composition of the tumor interstitial fluid, indicating that the overall tumor context may exert a strong influence over the TME. Strategies to increase alternative programs, such as lipid metabolism driven by PGC1α[170]

or PPARα[190], may rewire metabolism and overcome these metabolic deficiencies, although the metabolic implications of these adaptations for T cell proliferation and effector function remain poorly understood.

Tumor cells also produce byproducts detrimental to T cells. Indoleamine 2,3-dioxygenase (IDO) in cancer cells catalyzes oxidative catabolism of tryptophan, thus dampening antitumor immune responses by depleting this essential amino acid and producing kyneurenine, which generates immunosuppressive regulatory T cells (Tregs)[191,192]. These Tregs in turn can promote IDO expression on dendritic cells, further increasing kynurenine and depleting tryptophan in the TME.[193] Another toxic byproduct produced by cancer cells is lactate[194]. High lactate concentrations produced by tumor cells impeded lactic acid export in $CD8^+$ T cells and thus suppressed their effector function[195]. Tumor-associated expression of lactate dehydrogenase A is associated with lower survival and impaired T cell activity in melanoma patients[172]. In contrast, a recent proteomic analysis of melanoma showed that tumors with higher oxidative phosphorylation and lipid metabolism had increased antigen presentation and were associated with response to anti-PD-1 or TIL-based immunotherapy[196]. One possible explanation could be that these tumors are undergoing less glycolysis, creating an excess supply of glucose for infiltrating T cells[196]. In addition, these tumors would also secrete less lactate, creating a more favorable environment for T cell-mediated killing[196]. Overall, T cells face fierce competition for nutrients and are exposed to a multitude of toxic byproducts that can impair their function in the TME.

Component of the TME	Impact on T Cell Metabolism	Effect on Anti-Tumor Immunity
Hypoxia	• Stabilizes HIF-1a • Increases pyruvate dehydrogenase kinase, blocking the conversion of pyruvate to acetyl-CoA and thus mitochondrial respiration and ROS production • Increases lactate dehydrogenase A expression and inactivates pyruvate dehydrogenase, shunting pyruvate to lactate	• Increases granzyme B packaging into granules, leading to rejection of B16 tumors in mice • Upregulates PD-L1 expression on MDSCs • Decreases T cell infiltration
Depletion of Glucose	• Reduces aerobic glycolysis • Decreases levels of phosphoenolpyruvate, which regulates calcium and NFAT signaling	• Suppresses TIL effector function • Reduces EZH2 expression, decreasing T cell polyfunctionality
Accumulation of Lactate	• Impedes lactic acid export from $CD8^+$ T cells, which slows down glycolysis and reduces ATP levels • Decreases NFAT levels and translocation to the nucleus	• Inhibits T cell proliferation, activation, and function • Induces T and NK cell apoptosis
Tumor-derived Extracellular Vesicles (EVs)	• Modulates the metabolism of tumor associated macrophages and other cell types. • Effects of EVs on T cell metabolism are currently unknown	• Suppresses TIL anti-tumor function. • However, blocking EV biogenesis induces T cell activation, proliferation, and effector function.

Table 1. Hostile conditions in the tumor microenvironment impair T cell metabolism and anti-tumor immunity

Cancer cell metabolism, improper blood vessel formation, and extracellular vesicles all contribute to a toxic milieu deficient in key nutrients, such as glucose and oxygen, and high in waste products, such as lactate. Consequently, TILs entering the TME are deprived of key nutrients, disturbing metabolic processes critical for their anti-tumor functions.

Extracellular vesicles

In addition to the concentration of metabolites, gradients in molecular elements like O_2, and changes in physical characteristics of the TME such as pH, there are other discrete transferable factors that may also influence immune cell metabolism and function. Extracellular vesicles (EVs) encompass a diverse set of membrane vesicles secreted by most, if not all, cell types[197]. Tumors have been shown to secrete an abundance of EVs that can subsequently have biological effects on many different cell types, including immune cells[198–200]. Under hypoxic conditions, pancreatic cancer cells secrete microRNAs into EVs that activate the PI3K signaling pathway to induce M2 macrophage polarization, which subsequently promotes cancer progression and predicts poor prognosis[201]. Recent studies have begun to investigate metabolic effects of secreted EVs. In particular, both hepatic stellate cells and mutant KRAS colonic cells have been found to release EVs containing Glut1, which induces glycolysis in other cells in the TME[202,203]. In addition, proteomic and lipidomic analysis of EVs released from tumor associated macrophages were shown to contain a Th1/M1 signature and enzymes involved in lipid metabolism, which strongly correlated with an anti-tumor immune phenotype[204]. The full range of effects of EVs on immune cell metabolism and function in anti-tumor immunity remains uncertain but has the potential to impact immunotherapy.

Directly Manipulating T Cell Metabolism to Improve Immunotherapy

There is considerable excitement surrounding ICB to treat cancer, which may derive its efficacy in part by altering T cell metabolism. Although both PD-1 and CTLA-4 impair utilization of glucose and glutamine by decreasing their uptake, these immune checkpoint

proteins change lymphocyte metabolism through distinct molecular mechanisms[205,206]. In particular, PD-1 signaling blocks activation of PI3K and Akt in T lymphocytes, flipping a metabolic switch from glycolysis to lipolysis and fatty acid oxidation and thus impairing effector function[206]. A similar metabolic shift and decrease in cytokine production was observed upon PD-1 ligation activating STAT3 in $CD8^+$ T cells, facilitating obesity-associated breast cancer progression[207]. These findings suggest that PD-1 blockade may function synergistically at two levels by re-invigorating T cell glycolysis while simultaneously inhibiting tumor cell glycolysis. On the other hand, binding of CD80 and CD86 to CTLA-4, a negative regulator of CD28 co-stimulation, inhibits glycolysis without affecting fatty acid oxidation, maintaining the metabolic program of quiescent cells and blocking this interaction can enhance CD28-mediated T cell metabolic reprogramming[206]. Like PD-1, ligand engagement of CTLA-4 also blocks Akt activation, but CTLA-4 performs this function in a PI3K-independent fashion[205]. Thus, the suppressive effects of CTLA-4 on T cell activation may stem from its preservation of a bioenergetic profile similar to non-stimulated cells, while PD-L1 binding to PD-1 induces a distinct T cell metabolic state.

Modulating the metabolism of T cells presents an exciting avenue to improve current immunotherapies, in particular adoptive cell transfer, in which T cells are taken from a patient, primed, and expanded *ex vivo* before transfusing them back into the patient. This process requires careful manipulation of the T cells and presents an opportunity for discrete access to the cells for metabolic interventions. Several studies have shown that modulating the metabolism of adoptively transferred T cells with pharmacologic agents is a promising path to improve this form of immunotherapy[208]. Treating T cells *in vitro* during the priming and expansion phases with 2-deoxyglucose (2-DG), an inhibitor of glycolysis, increased memory T cell formation and

subsequently enhanced antitumor function *in vivo*[209]. Adoptive transfer of antigen-specific T cells treated *ex vivo* with an inhibitor of oxygen-sensing prolyl-hydroxylase domain proteins increased glycolytic activity and reduced lung metastasis in a B16-melanoma model[210]. Similarly, treating T cells *in vitro* with Mdivi, an inhibitor of mitochondrial fission, also increases *in vivo* anti-tumor activity[153]. Moreover, *in vitro* Akt pharmacologic inhibition increased the persistence of memory T cells after adoptive transfer and led to increased antitumor function *in vivo*[211]. Finally, adding bicarbonate to neutralize acidic environments improved response rates to checkpoint inhibition and adoptive cell therapy in mice models of melanoma[212]. Taken together, these studies indicate that fine-tuning T cell metabolism *in vitro* prior to transfusion back into patients is key to their success *in vivo.*

Conclusion

Disruption of T cell activation due to altered tumor cell metabolism and other metabolic features in the TME indicates that this is an important mechanism for immunosuppression. As tumors grow and proliferate, they rapidly consume nutrients such as oxygen and glucose and secrete lactate, creating regions of hypoxia and high acidity. Cancer cells and cells in the tumor microenvironment also shed EVs which may convey metabolic signals that can further hinder immune cell function. Upon entering the TME, TILs must overcome these metabolic challenges in order to mount a successful immune response. Although significant progress has been made in strengthening immunotherapy regimens, there remains significant knowledge gaps about how they work and why a majority of patients do not respond to treatment.

There are a number of challenges and opportunities to exploit the TME and immunometabolism in immunotherapy. One key challenge is to identify metabolic pathways that are cancer-specific or targets that can negatively influence cancers while improving the TME for immune function and not overly impairing immune cells. Targeting some pathways, such as glucose metabolism, may be challenging because both cancer and effector T cells and macrophages use and require these pathways. However, it was recently shown that other metabolic pathways, such as glutamine-dependent metabolism, may be more critical for cancer cells than inflammatory effector T cells or macrophages[151,152,213], indicating that it may be possible to both target cancer metabolism and enhance immunity. The influence of tumor type, location, and diet on metabolites in the TME[189] though could necessitate context-specific interventions. Nevertheless, dietary modifications that affect nutrient availability in the TME and have shown promise in clinical trials to slow tumor growth, though context specific aspects may require distinct guidelines for different cancers[214].

Another instance where immunometabolism may be exploited to enhance immunotherapy is through adoptive cell therapy. Indeed, the potential to enhance the metabolic capacity of Chimeric Antigen Receptor (CAR)-T cells or other cells through *in vitro* manipulation prior to cell transfer may overcome barriers of unintended direct effects on the tumor cells. The potential side effects of metabolic modulatory drugs have also not been fully explored and must be considered as normal tissues may be affected. Nevertheless, metabolic inhibitors have had fewer toxicities than expected, possibly due to the lower metabolic activity and high degree of metabolic flexibility of most tissues. Key remaining questions include: Can we translate findings from experimental models to humans? How do we keep T cells alive long enough to form memory cells to reject future cancer cells? How do we balance activating anti-

tumor T cells with autoimmune side effects or inadvertently enhancing cancer cell growth? Understanding the T cell metabolic program and how it underlies function and dysfunction represents a promising venue that can be exploited to improve immunotherapy efficacy.

CHAPTER III

SETD2 LOSS SENSITIZES CELLS TO PI3Kβ AND AKT INHIBITION

Esteban A. Terzo[1,5±], Aaron R. Lim[1,2±], Anna Chytil[1], Yun Chen Chiang[3,6], Leah Farmer[1], Kathryn E. Hacker Gessner[3], Cheryl Lyn Walker[4], and Valerie M. Jansen[1,7]*, W. Kimryn Rathmell[1]*

[1]Vanderbilt-Ingram Cancer Center, Division of Hematology and Oncology, Department of Medicine, Vanderbilt University Medical Center, Nashville, TN 37232, [2]Medical Scientist Training Program, Vanderbilt University School of Medicine, Nashville, TN 37232, [3]Lineberger Comprehensive Cancer Center, University of North Carolina, Chapel Hill, NC 27599, [4]Center for Precision Environmental Health, Baylor College of Medicine, Houston, TX 77030, [5]Now at: Constellation Pharmaceuticals, [6]Now at: Novella/IQVIA, [7]Now at: Eli Lilly and Company, [±]Co-first authors, *Co-corresponding authors

The work presented in this section is published in *Oncotarget*[215] and has been reproduced with the permission of the journal and my co-authors.

Abstract

Upregulation of the PI3K pathway has been implicated in the initiation and progression of several types of cancer, including renal cell carcinoma (RCC). Although several targeted

therapies have been developed for RCC, durable and complete responses are exceptional. Thus, advanced RCC remains a lethal disease, underscoring the need of robust biomarker-based strategies to treat RCC. We report a synthetic lethal interaction between inhibition of phosphatidylinositol 3-kinase beta (PI3Kβ) and loss of *SETD2* methyltransferase. Clear cell RCC (ccRCC)-derived *SETD2* knockout 786-0 and *SETD2* mutant A498 cells treated with TGX221 (PI3Kβ-specific) and AZD8186 (PI3Kβ- and δ-specific) inhibitors displayed decreased cell viability, cell growth, and migration compared to *SETD2* proficient 786-0 cells. Inhibition of the p110 δ and α isoforms alone had modest (δ) and no (α) effect on ccRCC cell viability, growth, and migration. *In vivo*, treatment of *SETD2* mutant A498 cells, but not *SETD2* proficient 786-0 cells, with AZD8186 significantly decreased tumor growth. Interestingly, inhibition of the downstream effector AKT (MK2206) recapitulated the effects observed in AZD8186-treated *SETD2* deficient cells. Our data show that specific inhibition of PI3Kβ causes synthetic lethality with *SETD2* loss and suggest targeting of the AKT downstream effector pathway offers a rationale for further translational and clinical investigation of PI3Kβ-specific inhibitors in ccRCC.

Introduction

Renal cell carcinoma (RCC) is composed of a heterogeneous group of cancers and is the ninth most common cancer worldwide[5]. Clear cell renal cell carcinoma (ccRCC), the most common histological subtype, accounts for the majority of RCC-related deaths[216]. ccRCC tumors are known to be unresponsive to traditional chemotherapies and lack the genetic hallmarks of other solid tumors, such as *KRAS* and *TP53* mutations[217]. A number of targeted therapies against

the vascular endothelial growth factor (VEGF) and mechanistic target of rapamycin (mTOR) pathways have been developed, in addition to recent advances in immunotherapy, but the response to these treatments is varied with the majority of patients eventually developing progressive disease[218]. This underscores the urgent need to identify biomarkers that better predict tumor behavior in response to targeted therapeutics.

In ccRCC tumors, the tumor suppressor von Hippel-Lindau (*VHL*) is the most frequently mutated gene[14,219]. Its complete inactivation by either mutation or methylation is observed in more than 80% of ccRCCs and represents the earliest truncal oncogenic event in these tumors[15,220–222]. In recent years, large-scale cancer genomic projects have revealed numerous additional mutations in other tumor suppressors genes encoding chromatin remodelers, including protein polybromo 1 (*PBRM1/BAF180*), BRCA associated protein 1 (*BAP1)*, and Set domain containing 2 (*SETD2*) [47,52,223]. As opposed to *VHL* inactivation, a known founding event of ccRCC, mutations in genes involved in disease progression such as *PBRM1*, *BAP1*, and *SETD2* are associated with aggressive clinical features[224–226].

SETD2 encodes a methyltransferase known to be responsible for the trimethylation of lysine 36 on histone H3 (H3K36me3)[227,228], a mark associated with actively transcribed genes. In addition to H3K36, SETD2 methylates two novel non-histone targets: α tubulin on lysine 40 (αTubK40me3) of mitotic microtubules[58] and STAT1 on lysine 525 (STAT1K525me1)[60]. By methylating such diverse targets, SETD2 contributes to the maintenance of a wide spectrum of biological processes ranging from chromatin accessibility, mRNA splicing and processing[55], DNA double-strand break repair[53], genomic stability[58], and cellular defense against viral infection[60]. The diversity of molecular pathways requiring SETD2's methylating activity

underscores the enzyme's crucial role in maintaining cellular homeostasis and warrants further investigation into molecular networks involving SETD2 that drive ccRCC oncogenesis.

The phosphoinositide 3-kinase (PI3K)-AKT axis is the most commonly altered molecular pathway in cancer[229]. Although the PI3K-AKT pathway presents a relatively low overall mutation rate in ccRCC when compared to other cancer types, the overall activation of AKT and downstream substrates is high[63–65]. A recent study utilizing the Genomics of Drug Sensitivity in Cancer (GDSC) database identified that RCC cells with mutated *VHL* or *SETD2* were sensitive to the small molecule PIK3β inhibitor TGX221[230]. TGX221 was also shown to target cancer cells with *CDKN2A* and *PTEN* mutations, suggesting nonspecific inhibition at the molar concentration (5 μM) used in the study.

In this study, we sought to expand on this reported sensitivity by examining the effects of genetic and pharmacologic inhibition of the PI3K-AKT axis and its downstream effectors in more well-defined and *in vivo* model systems. We show that *SETD2* deficient 786-0 and A498 cells are significantly more sensitive to PI3Kβ-specific (TGX221 and GSK2636) and PI3Kβ/δ-specific (AZD8186) inhibitors than *SETD2* proficient (+/+) isogenic paired 786-0 cells, as evidenced by impaired viability, cell migration, spheroid formation, as well as genotype-selective reduced growth *in vivo*. These findings are replicated with siRNA approaches to confirm the target involvement. At the molecular level, we show that pAKT-S473, pPRAS40, and pS6-S235/236 phosphorylation levels are selectively reduced in *SETD2* deficient cell lines treated with the PI3Kβ-specific inhibitors TGX221 and AZD8186. Lastly, *SETD2* deficient cell lines treated with MK2206 (AKT-specific inhibitor) recapitulated the effects observed in AZD8186-treated *SETD2* deficient cells, implicating canonical PI3K signaling via AKT as a key mechanism of viability. Combined, our data demonstrate a molecular crosstalk between SETD2

methyltransferase and PI3Kβ kinase critical for *in vitro* cell proliferation and migration and for growth *in vivo*. Further, our results demonstrate that p-AKT-S473 is an integral component of the SETD2-PI3Kβ axis and shed light on the molecular mechanism underlying this novel pathway.

Results

PI3Kβ-specific inhibitors cause synthetic lethality with *SETD2* loss in ccRCC-derived cells

We have observed that the deletion of *SETD2*, following clonal selection, consistently produces cells with a slightly more rapid cell cycle transit time[231], and a measurable advantage in proliferation. Notably, *SETD2* knockout (KO) ccRCC-derived 786-0 cells, previously generated and described in more detail[58], showed a significantly higher proliferation rate than their *SETD2* proficient (+/+) counterparts [Figure 9]. To explore the molecular mechanism underlying the proliferative advantage of these cells and determine whether critical vulnerabilities exist between targetable PI3K-AKT pathway members and *SETD2* loss, we treated *SETD2* proficient and *SETD2* deficient ccRCC-derived cell lines with a panel of inhibitors targeting PI3Kα (BYL719); PI3Kβ (TGX221, GSK2636, AZD8186); PI3Kδ (Idelalisib); and all PI3K isoforms with a Pan-PI3K inhibitor (BKM120). In addition to 786-0 *SETD2* proficient (+/+) and *SETD2* knockout (KO) cells, we used *SETD2* deficient A498 cells, which have lost one *SETD2* allele due to loss of the short arm of chromosome 3 (3p) and carry a two-base pair c.6098_6099 deletion (delTG) that causes a frameshift in the carboxyl terminus that inactivates the second allele. These cells express a SETD2 with reduced histone H3 on lysine 36 trimethylating activity and hereinafter referred to as (-/-), for simplicity.

We seeded all three cell lines in duplicate into 24-well plates and assessed viability by counting cell number from one well and by staining living cells with 0.3% crystal violet solution in the other for each treatment at 10 days, and obtained data from three independent biological experiments. Characterization of the three cell lines by immunoblotting showed that, as expected, *SETD2* proficient 786-0 cells express a functional SETD2 protein, whereas *SETD2* KO 786-0 cells do not. Moreover, *SETD2* (-/-) A498 cells express reduced levels of SETD2 protein accompanied by a noticeably reduced capacity to trimethylate histone H3 on lysine 36 (H3K36me3) [Figure 10A]. The two *SETD2* deficient cell lines showed a significant increase in sensitivity to all three PI3Kβ (AZD8186>TGX221>GSK2636) inhibitors, as evidenced by their decreased relative cell viability. When treated with the PI3Kα-specific inhibitor BYL719, *SETD2* deficient 786-0 and A498 lines did not show the pronounced relative cell viability changes consistently observed with PI3Kβ-specific inhibitors, although viability was somewhat decreased [Figure 10B and Figure 11A]. As AZD8186 is known to inhibit both PI3Kβ and δ isoforms in a cell-free assay (IC_{50} = 4nM and 12nM, respectively), we also treated cells with the PI3Kδ-specific inhibitor Idelalisib to see if this PI3K isoform also contributed to synthetic lethality with *SETD2* loss. Both *SETD2* deficient cell lines were sensitive to Idelalisib; however, cell viability was not as dramatically decreased as with PI3Kβ-specific inhibitors [Figure 10B and Figure 11A]. When *SETD2* deficient cells (KO 786-0 and (-/-) A498) were treated with the Pan-PI3K inhibitor BKM120, they displayed a significant increase in sensitivity that resembled the effects observed with PI3Kβ-specific inhibitors [Figure 10B and Figure 11A].

To further examine whether the observed sensitivity of *SETD2* deficient cells was specifically determined by PI3Kβ isoform inhibition, we conducted a dose-response assay using AZD8186, as it displayed the most pronounced response among the three PI3Kβ-specific

inhibitors [Figure 11A], along with BYL719 (PI3Kα-specific), Idelalisib (PI3Kδ-specific), and BKM120 (Pan-PI3K) inhibitors and calculated their respective half maximal inhibitory concentrations (IC_{50}s). Dose-response curves showed that *SETD2* deficient 786-0 and A498 cells were highly sensitive to AZD8186 when compared to *SETD2* proficient 786-0 cells (IC_{50} = 0.29μM, 0.01μM, and 21μM respectively) [Figure 11B]. In addition, all three cell lines were only sensitive to BYL719 at toxic concentrations[232]. Idelalisib dose-response curves showed that *SETD2* deficient 786-0 and A498 cells were more sensitive to the PI3Kδ-specific inhibitor than *SETD2* proficient 786-0 cells. However, the difference was not as pronounced as that observed with AZD8186 treatment. The Pan-PI3K dose-response curves also showed that, at low concentrations, *SETD2* deficient cells were more sensitive to the compound than *SETD2* proficient cells. However, at higher drug concentrations, sensitivity was SETD2-independent, as all three cell lines showed increased sensitivity. Combined, these data show that PI3Kβ-specific inhibitors, and most prominently AZD8186, cause a synthetic lethal-type interaction with *SETD2* loss in ccRCC-derived cell lines.

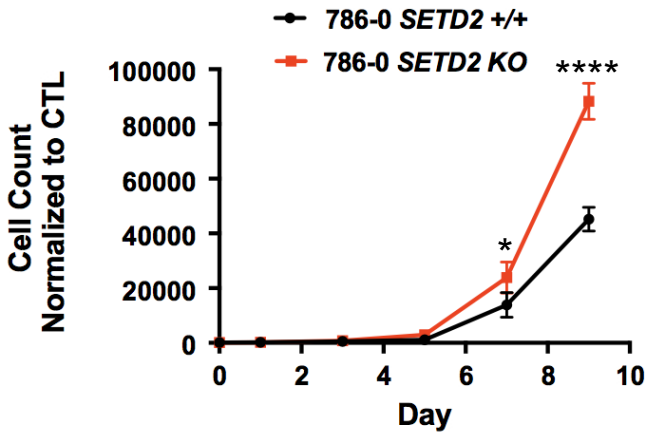

Figure 9. Increased proliferation rate in *SETD2* deficient ccRCC-derived cells

Graph showing proliferation curves for *SETD2* proficient (+/+) and *SETD2* deficient (KO) 786-0 cells as a function of time (day). Cell count was normalized to control (CTL). *, $P < 0.05$; ****, $P < 0.0001$. Standard deviations were calculated and represented for all conditions.

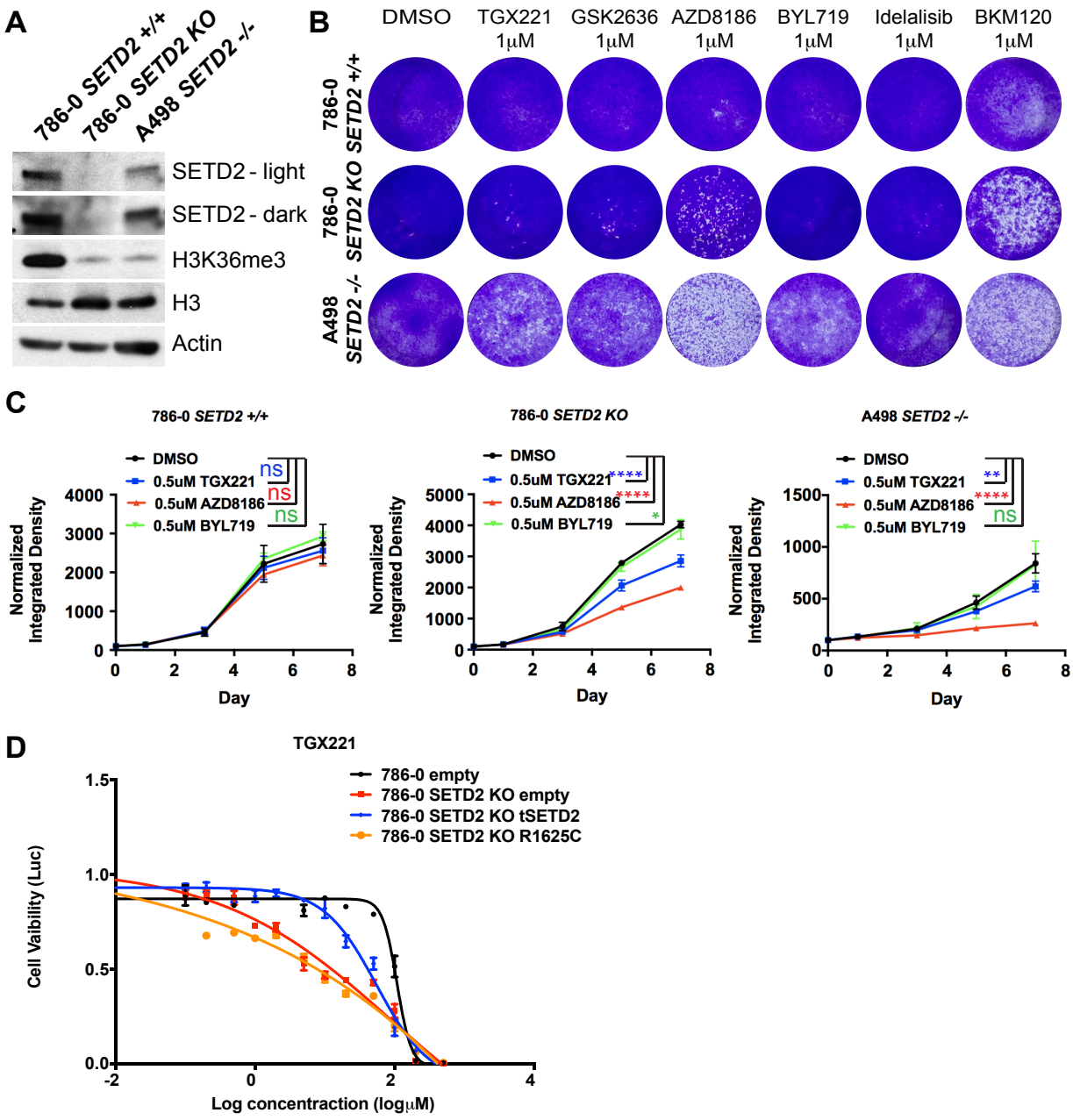

Figure 10. Response of *SETD2* proficient and *SETD2* deficient RCC cell lines to PI3K inhibitors

(A) Western blot analysis of indicated proteins showing variations in histone H3 lysine 36 trimethylation (H3K36me3) levels in *SETD2* proficient (+/+) and *SETD2* deficient (KO) 786-0 and (-/-) A498 cells. SETD2 blotting is shown in two exposures (light and dark). Whole-cell

protein lysates from cells grown for 24 hours were resolved by SDS-PAGE. Actin is a loading control. (B) Bright-field microscopy images showing living cells (attached to bottom of well) stained with 0.3% crystal violet solution of *SETD2* (+/+) 786-0 and *SETD2* (KO) 786-0 and (-/-) A498 cells were treated with vehicle (DMSO) or 1μM inhibitor for 10 days. (C) Graphs plotting normalized integrated density calculated from cells stained with 0.3% crystal violet solution as a function of time (day) showing proliferation rates of *SETD2* proficient (+/+) and *SETD2* deficient (KO) 786-0 and (-/-) A498 cells treated with 0.5μM of TGX221 (blue line), AZD8186 (red line), and BYL719 (green line) or DMSO (black line) as control for 7 days. *, $P < 0.05$; **, $P < 0.005$; ****, $P < 0.0001$; ns, no statistical significance observed. Standard deviations were calculated and represented for all conditions. (D) Cell viability for 786-0 cells treated with a dose titration of TGX221. Genetic modifications to knock out and rescue SETD2 expression are indicated in the legend, showing increased sensitivity for those cells lacking SETD2 methylating activity.

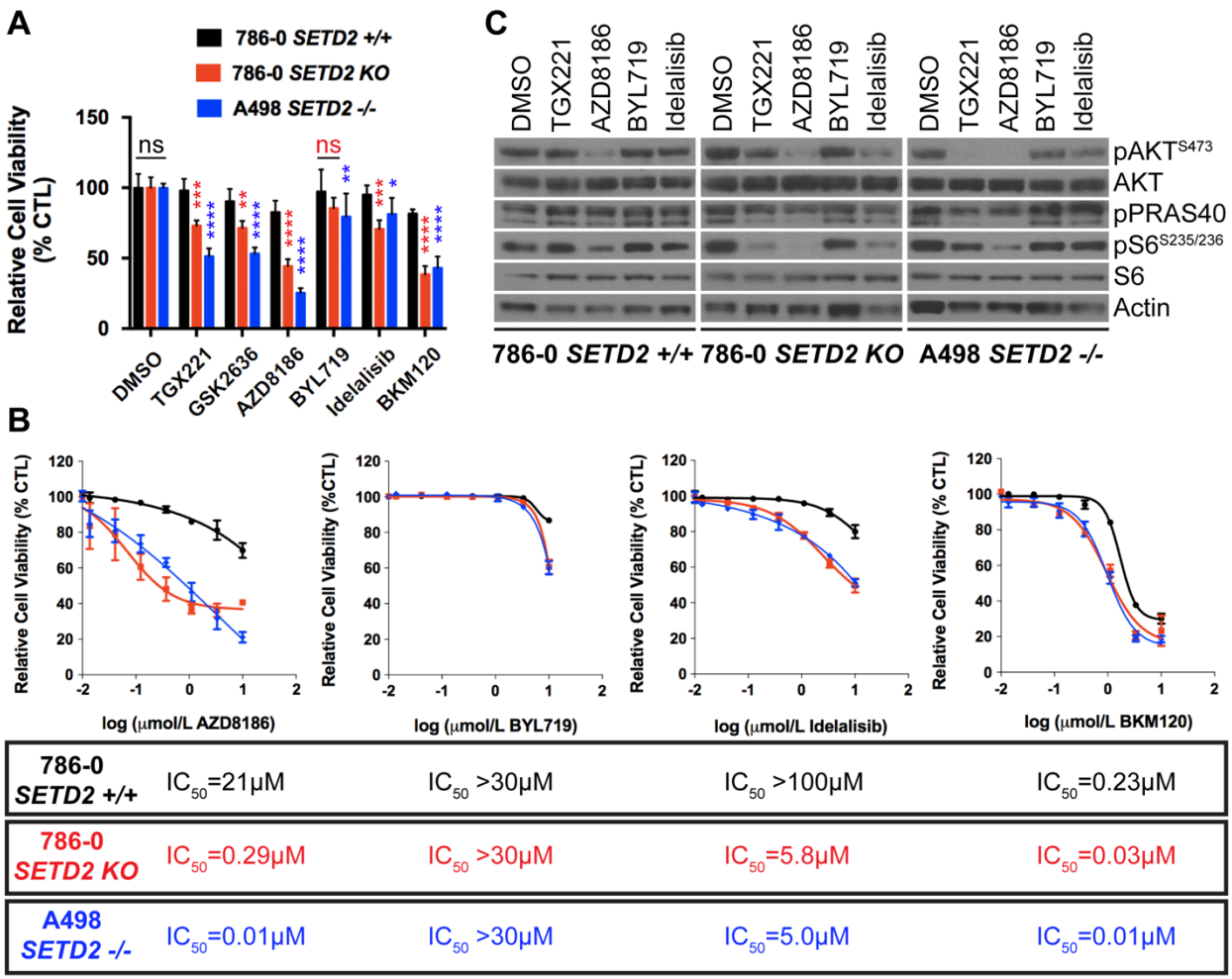

786-0 *SETD2 +/+*	IC_{50}=21μM	IC_{50} >30μM	IC_{50} >100μM	IC_{50}=0.23μM
786-0 *SETD2 KO*	IC_{50}=0.29μM	IC_{50} >30μM	IC_{50}=5.8μM	IC_{50}=0.03μM
A498 *SETD2 -/-*	IC_{50}=0.01μM	IC_{50} >30μM	IC_{50}=5.0μM	IC_{50}=0.01μM

Figure 11. Increased sensitivity of *SETD2* deficient ccRCC-derived cells to PI3Kβ-specific inhibitors

(A) Bar graph showing relative cell viability as a percentage of CTL (DMSO-treated) of *SETD2* proficient (+/+) 786-0 and *SETD2* deficient (KO) 786-0 and (-/-) A498 cells in response to treatment with small-molecule inhibitors. *, $P < 0.05$; **, $P < 0.005$; ***, $P < 0.001$; ****, $P < 0.0001$; ns, no statistical significance. Standard deviations were calculated and represented for all conditions. (B). Dose-response curves showing sensitivity to AZD8186, BYL719, Idelalisib, and BKM120 at different concentrations. IC_{50} was calculated for each treated cell line with a non-linear fit of transformed values using GraphPad software. (C) Western blot analysis of

indicated proteins showing variations in phosphorylation levels in response to chemical inhibition. Whole-cell protein lysates from cells treated with 1μM inhibitor for 24 hours were resolved by SDS-PAGE. Actin is a loading control.

PI3Kβ-specific inhibitors TGX221 and AZD8186 decrease proliferation in *SETD2* deficient ccRCC-derived cells

To explore if the synthetic lethal interaction between *SETD2* loss and targeted PI3Kβ inhibition specifically affects cell proliferation, we treated *SETD2 (+/+)* 786-0, *SETD2* (*KO*) 786-0, and *SETD2 (-/-)* A498 cell lines with TGX221, AZD8186, and BYL719 and measured cell number over 7 days. *SETD2* deficient cells showed a significantly decreased proliferation rate when treated with TGX221 and consistently more so with AZD8186, while BYL719 showed a mild or no decrease in all tested cell lines [Figure 10C]. Notably, 786-0 *SETD2* KO cells rescued with functional truncated SETD2 (tSETD2) abrogated sensitivity to PI3Kβ inhibition, whereas a catalytically inactivating mutation in the SET domain (R1625C) still retained increased sensitivity to PI3Kβ inhibition [Figure 10D].

To interrogate what downstream effectors of the PI3Kβ-AKT axis might mediate the synthetic lethal interaction, we conducted a drug-target engagement experiment treating *SETD2* proficient (786-0) and *SETD2* deficient (786-0 and A498) cells with 1μM inhibitor for 24 hours. Immunoblotting of whole-cell extracts from treated cells showed that phosphorylation of pAKT-S473 and pS6-S235/236 were decreased in *SETD2* deficient cells relative to SETD2-proficient cells by TGX221, whereas AZD8186 treatment resulted in inhibition of AKT and S6 phosphorylation in both SETD2-proficient and SETD2-deficient cells. The same was observed for pPRAS40, which is a phosphorylation target of AKT [Figure 11C]. These results show that *SETD2* deficient ccRCC-derived cells are significantly less proliferative when treated with PI3Kβ inhibitors and strongly suggest inhibition of downstream effectors in the PI3K pathway (pAKT-S473 and pS6) may play a role in this synthetic lethal interaction.

Genetic inhibition of PI3Kβ with siRNA reduces viability of *SETD2* deficient ccRCC-derived cells

To confirm that pharmacological inhibition (small-molecule inhibitors) specifically causes synthetic lethality in *SETD2* deficient cells via effects on PI3Kβ (as opposed to off-target effects elsewhere), we conducted a genetic knockdown experiment using siRNA specifically targeting the α, β, and δ isoforms of PI3K. We interrogated the effect of siRNA for single targets or in combinations (α/β and β/δ) on cell viability. We predicted that siRNA targeting PI3Kβ would closely replicate the effect on relative cell viability observed in *SETD2* deficient ccRCC-derived cells when treated with PI3Kβ-specific inhibitors. Knockdown using two different siRNAs specifically targeting PI3Kβ (si-p110β-1 and -2) consistently showed a significant decrease in the relative viability of both *SETD2* KO 786-0 and *SETD2* -/- A498 cells when compared to that of *SETD2* proficient 786-0 cells, a phenomenon not observed with si-p110α- or si-p110δ-specific knockdowns [Figure 12A]; immunoblotting confirmed the specificity of the single and combinatorial knockdowns [Figure 12B].

When siRNAs targeting PI3Kβ were used in combination with those against α and δ PI3K isoforms, the combinatorial siRNA treatments showed a significant decrease in relative cell viability, but not as pronounced as the effect observed when cells were treated with either of these siRNAs against PI3Kβ (si-p110β-1 or -2) alone [Figure 12A]. Phosphorylation levels of a PI3K downstream effector, pAKT-S473, were assessed by immunoblot analysis to corroborate the efficiency of PI3K isoform knockdowns. We found that reduced levels of pAKT-S473 were observed in whole cell extracts from the three RCC-derived cell lines when treated with siRNA against PI3Kβ alone and in combination with si-p110δ [Figure 12B]. These results strongly suggest that the decrease in pAKT-S473 phosphorylation levels observed when PI3Kβ is

chemically inhibited (TGX221 and more consistently AZD8186) [Figure 11C] was due to the specific inhibition of PI3Kβ's enzymatic activity, revealing pAKT-S473 as a critical reporter, and perhaps mediator, of the SETD2-dependency on the PI3Kβ signaling network.

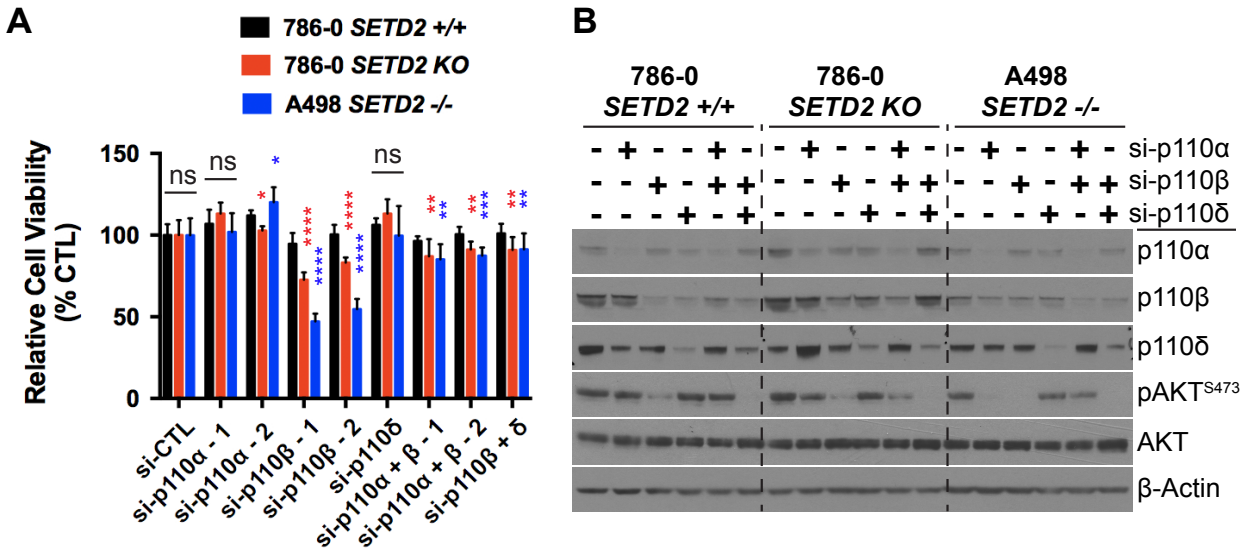

Figure 12. Genetic inhibition of PI3K p110β with siRNA reduces viability of *SETD2* deficient ccRCC-derived cells

(A) Bar graph showing relative cell viability as a percentage of control (si-CTL) of *SETD2* (+/+) 786-0 and *SETD2* (KO) 786-0 and (-/-) A498 cells in response to treatment with siRNA specific to p110α, p110β, and p110δ (singlets and doublets). *, $P < 0.05$; **, $P < 0.005$; ***, $P < 0.001$; ****, $P < 0.0001$; ns, no statistical significance observed. Standard deviations were calculated and represented for all conditions. (B) Western blot analysis of indicated proteins showing decrease in expression of p110α, p110β, and p110δ in individual or combinatorial treatments (specificity) and variations in phosphorylation levels of known downstream target pAKT-S473 (efficacy). Actin is a loading control.

PI3Kβ-specific inhibitors TGX221 and AZD8186 abrogate spheroid formation and cell migration in *SETD2* deficient ccRCC-derived cells

To determine if the tumor growth capacity of *SETD2* deficient ccRCC-derived cell lines was similarly dependent on PI3Kβ, we utilized 3-D spheroid cultures in Matrigel to allow cells to self-assemble into organotypic structures (spheroids). These spheroids mimic *in vitro* tumor morphology adopted *in vivo* and provide a tractable model for evaluating tumor growth in response to pharmacological agents. Untreated *SETD2* proficient 786-0 cells displayed a round spheroid morphology that remained almost unaffected despite the diverse treatments with PI3K isoform-specific and Pan PI3K inhibitors [Figure 13A]. Conversely, both *SETD2* deficient cell lines showed a less structured spheroid morphology and a significant decrease in their number when treated with PI3Kβ-specific, but not PI3Kα-specific, inhibitors when compared to *SETD2* proficient cells [Figure 13A and C]. Interestingly, both Idelalisib (PI3Kδ-specific) and BKM120 (Pan-PI3K) inhibitors showed significant cell growth decrease in *SETD2* deficient cell lines, but more prominently with the latter inhibitor, recapitulating the effects observed with PI3Kβ-specific inhibitors [Figure 13C].

To interrogate the ability of *SETD2* deficient cells to migrate in the presence of pharmacological agents, we performed a 2-D wound-healing assay. We then tracked migration through time (2 days) and stained with crystal violet once cells treated with vehicle reached confluency and calculated migration as a percentage (%) of wound closure. We observed that *SETD2* deficient cells were significantly less migratory than their *SETD2* proficient counterparts when treated with PI3Kβ-specific inhibitors, a phenomenon closely resembled by the treatment with the Pan-PI3K inhibitor, BKM120 [Figure 13B and D]. Combined, these data demonstrate that the capacity of *SETD2* deficient ccRCC-derived cell lines to form spheroids (3-D) and to

migrate (2-D) is significantly hindered by PI3Kβ-specific inhibitors, which we observed is closely replicated when these cells are treated with the Pan-PI3K inhibitor BKM120. These data also strongly suggest that the PI3Kβ pathway may participate in the regulation of both migration and tumor growth in SETD2-deficient states.

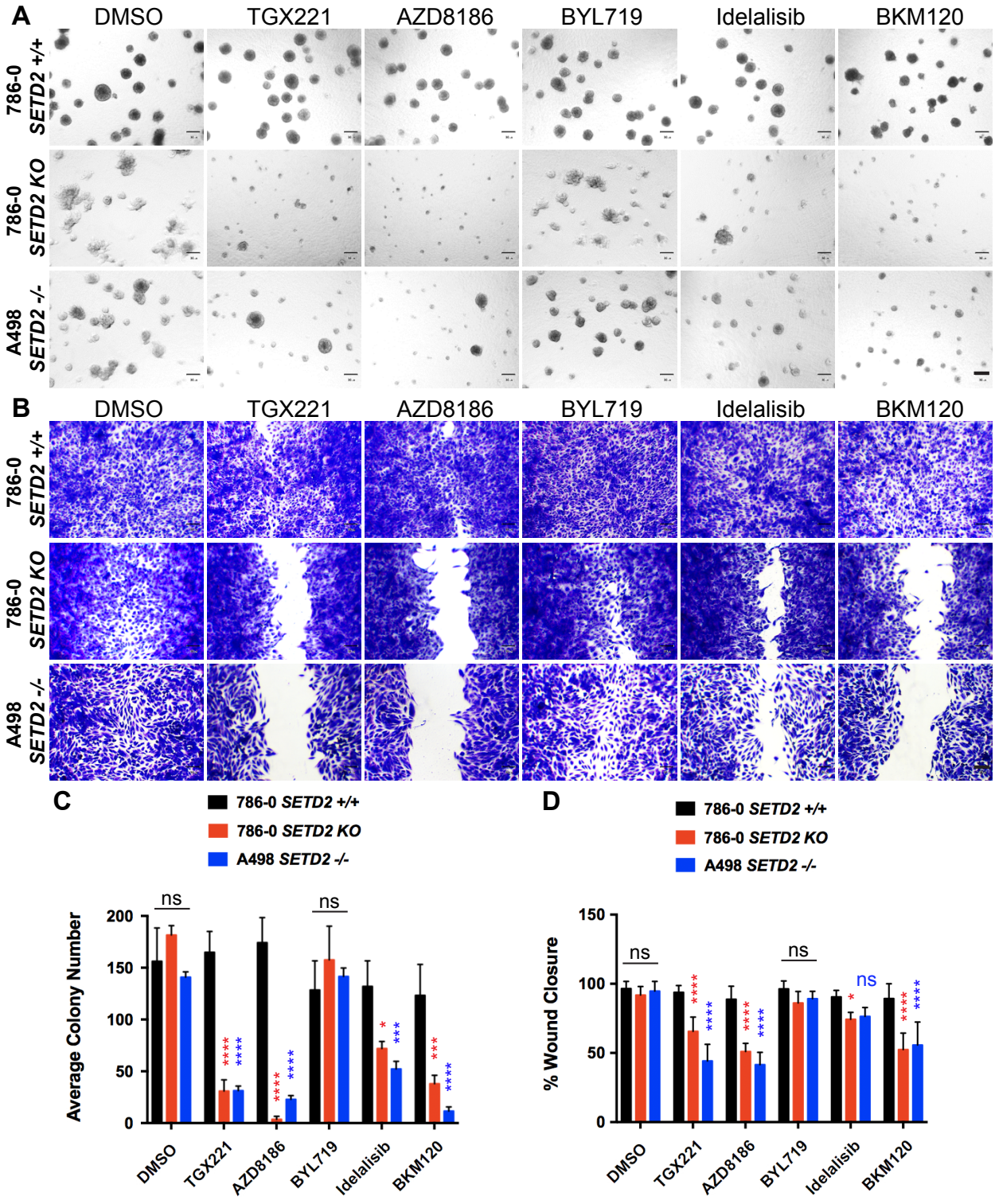

Figure 13. PI3Kβ-specific inhibitors TGX221 and AZD8186 abrogate spheroid formation and cell migration in *SETD2* deficient ccRCC-derived cells

(A) Phase-contrast pictures showing spheroid formation of *SETD2* (+/+) 786-0 and *SETD2* (KO) 786-0 and (-/-) A498 cells in response to treatment with vehicle (DMSO) and 500 nM inhibitor for 14 days grown in Matrigel. Scale bar: 30μm. (B) Bright-field microscopy images showing living cells stained with 0.3% crystal violet solution. Treated cells (1 μM for 3 days) incapable of migrating show remnants of scratch (wound) of different widths. Scale bar: 30 μm. (C) Bar graph showing average colony number for the three cell lines treated with different inhibitors. *, $P < 0.05$; ***, $P < 0.001$; ****, $P < 0.0001$; ns, no statistical significance observed. Standard deviations were calculated and represented for all conditions. (D) Bar graph showing percentage (%) of wound closure compared to cells treated with vehicle (DMSO). *, $P < 0.05$; ****, $P < 0.0001$; ns, no statistical significance observed. Standard deviations were calculated and represented for all conditions.

PI3Kβ-specific inhibitor AZD8186 abrogates *SETD2* deficient tumor formation *in vivo*

To translate our *in vitro* findings that *SETD2* deficient ccRCC-derived cells exhibit increased sensitivity to PI3Kβ-specific inhibition to the *in vivo* setting, we conducted xenograft studies. NOD *scid* gamma mice were injected subcutaneously with *SETD2* mutant ccRCC-derived A498 cells and approximately a month later, mice bearing tumors measuring ≥150 mm^3 were randomized to treatment with vehicle (control) or AZD8186. Animals treated with the PI3Kβ-specific inhibitor AZD8186 showed a significant decrease in tumor growth and final tumor weight compared to control mice [Figure 14A-C]. However, 786-0 *SETD2* proficient xenograft tumors did not have a significant response to PI3Kβ inhibition [Figure 15]. Thus, AZD8186 can effectively reduce growth of *SETD2* mutant tumors but not *SETD2* wild-type tumors, underscoring the importance of the molecular connection between the PI3Kβ signaling network and *SETD2* loss as a promising therapeutic target for ccRCC.

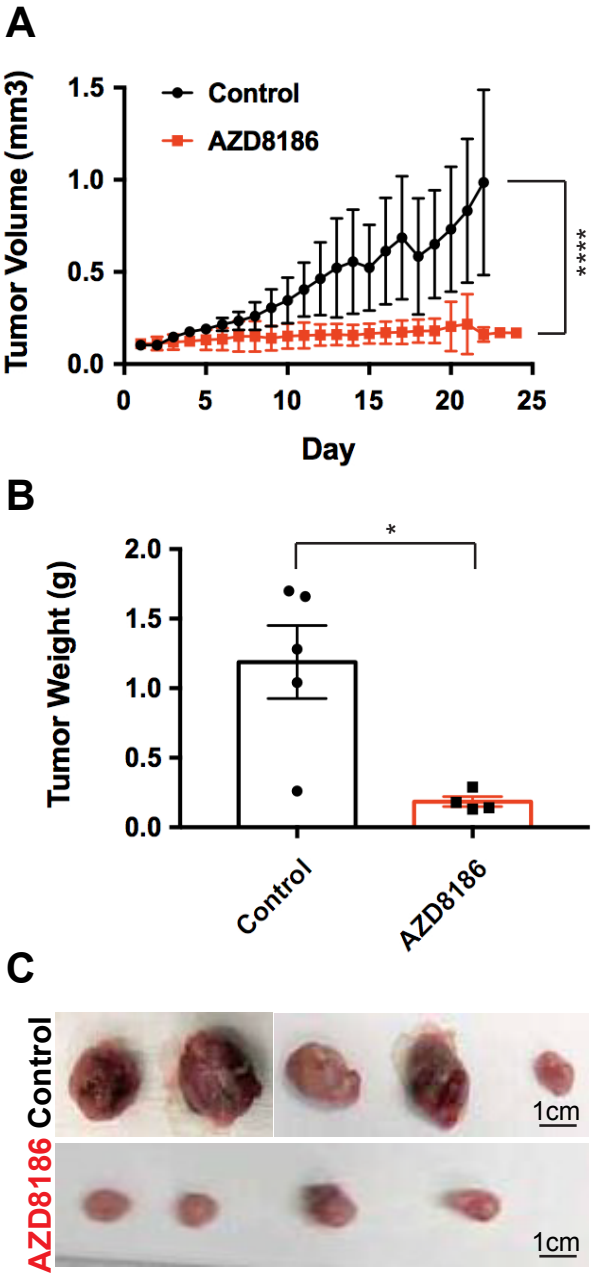

Figure 14. PI3Kβ-specific inhibitor AZD8186 hinders *SETD2* deficient tumors *in vivo*

(A) Graph plotting tumor volume (mm^3) as a function of time (day) showing changes in volume of untreated (control) and AZD8186-treated tumors. ****, $P < 0.0001$. (B) Bar graph showing average tumor weight (g) for control and AZD8186-treated tumors. *, $P < 0.05$. (C) Pictures of untreated (control) and AZD8186-treated tumors. Scale bar: 1cm.

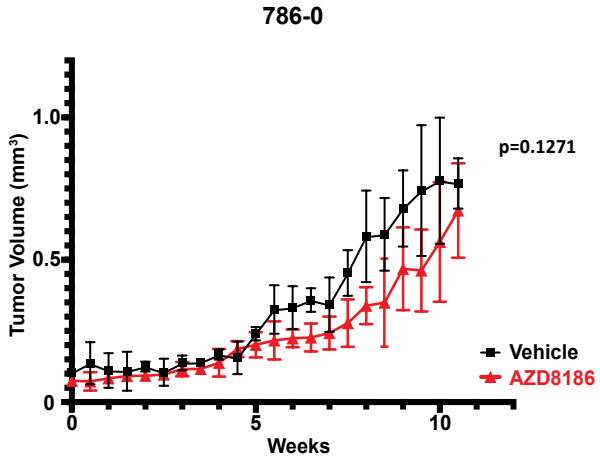

Figure 15. PI3Kβ-specific inhibitor AZD8186 does not significantly change *SETD2* proficient tumor growth *in vivo*

Graph plotting tumor volume (mm^3) as a function of time (week) for vehicle-treated (control) and AZD8186-treated tumors. Data are represented by mean ± standard deviation.

AKT-specific inhibitor MK2206 decreases cell viability, spheroid formation, and migration of *SETD2* deficient ccRCC-derived cells

Our previous data demonstrating that PI3Kβ-specific inhibitors decrease phosphorylation levels of key downstream effectors in the PI3K-AKT pathway (pAKT-S473 and pS6-S235/236) in *SETD2* deficient ccRCC-derived cells prompted us to further explore the molecular mechanism connecting SETD2 to PI3Kβ. To do this, we challenged *SETD2* proficient and *SETD2* deficient ccRCC-derived cell lines with the AKT-specific inhibitor MK2206 and observed their sensitivity to the compound, spheroid formation, and migration. Similar to the treatment with PI3Kβ-specific inhibitors, we observed that *SETD2* deficient cells were more sensitive to MK2206, as evidenced by a significant decrease in their cell viability [Figure 16A and B]. Sensitivity of *SETD2* deficient cells was also observed in 3-D growth and 2-D wound healing assays, where they displayed a significantly reduced ability to form spheroids and to migrate [Figure 16C-F]. Immunoblotting of whole-cell lysates from a drug-target engagement assay using 1μM of MK2206 showed that MK2206 effectively reduces phosphorylation levels of pAKT-S473. Interestingly, however, dramatically reduced pS6 phosphorylation levels were only observed in *SETD2* deficient cell lines [Figure 16G]. Together, these data demonstrate that AKT is a key effector of a molecular axis connecting SETD2 to PI3Kβ that is required for the regulation of growth and migration.

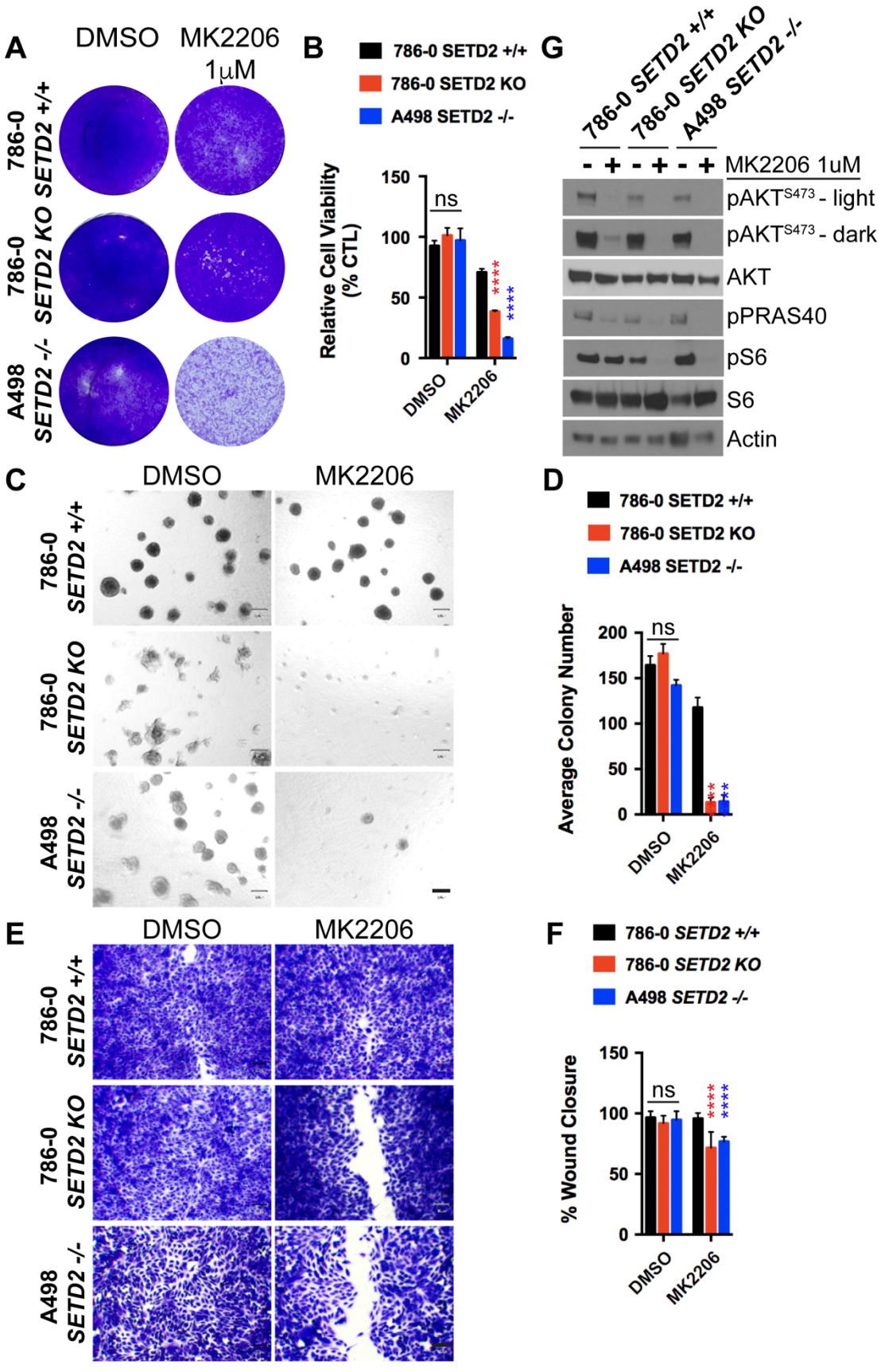
A
DMSO
MK2206 1μM
786-0 SETD2 +/+
786-0 SETD2 KO
A498 SETD2 -/-
B
786-0 SETD2 +/+
786-0 SETD2 KO
A498 SETD2 -/-
Relative Cell Viability (% CTL)
150
100
50
0
ns
****
****
DMSO
MK2206
G
786-0 SETD2 +/+
786-0 SETD2 KO
A498 SETD2 -/-
- + - + - +
MK2206 1uM
pAKTS473 - light
pAKTS473 - dark
AKT
pPRAS40
pS6
S6
Actin
C
DMSO
MK2206
786-0 SETD2 +/+
786-0 SETD2 KO
A498 SETD2 -/-
D
786-0 SETD2 +/+
786-0 SETD2 KO
A498 SETD2 -/-
Average Colony Number
200
150
100
50
0
ns
**
**
DMSO
MK2206
E
DMSO
MK2206
786-0 SETD2 +/+
786-0 SETD2 KO
A498 SETD2 -/-
F
786-0 SETD2 +/+
786-0 SETD2 KO
A498 SETD2 -/-
% Wound Closure
150
100
50
0
ns
****
****
DMSO
MK2206

Figure 16. AKT-specific inhibitor MK2206 decreases cell viability, spheroid formation, and migration of *SETD2* deficient ccRCC-derived cells

(A) Bright-field microscopy images showing living cells (attached to bottom of well) stained with 0.3% crystal violet solution of *SETD2* (+/+) 786-0 and *SETD2* (KO) 786-0 and (-/-) A498 cells were treated with vehicle (DMSO) or 1 μM AKT-specific inhibitor MK2206 for 10 days. (B) Bar graph showing relative cell viability as a percentage of CTL of *SETD2* (+/+) 786-0 and *SETD2* (KO) 786-0 and (-/-) A498 cells in response to treatment with MK2206. ****, $P <$ 0.0001; ns, no statistical significance observed. Standard deviations were calculated and represented for all conditions. (C) Phase-contrast pictures showing spheroid formation of *SETD2* (+/+) 786-0 and *SETD2* (KO) 786-0 and (-/-) A498 cells in response to treatment with vehicle (DMSO) and 500 nM inhibitor for 14 days grown in Matrigel. (D) Bar graph showing average colony number of *SETD2* (+/+) 786-0 and *SETD2* (KO) 786-0 and (-/-) A498 cells treated with MK2206 inhibitor. ****, $P < 0.0001$; ns, no statistical significance observed. Standard deviations were calculated and represented for all conditions. (E) Bright-field microscopy images showing living cells stained with 0.3% crystal violet solution. (F) Bar graph showing percentage (%) of wound closure compared to cells treated with vehicle (DMSO). (G) Western blot analysis of indicated proteins showing variations in phosphorylation levels in response to chemical inhibition with MK2206 (AKT-specific). Whole-cell protein lysates from cells treated with 1 μM inhibitor for 24 hours were resolved by SDS-PAGE. Actin is a loading control.

Discussion

ccRCC tumors are highly lethal and are characterized by resistance to chemotherapy, resulting in targeted therapies and immunotherapy emerging as the major mechanisms for treatment. Approximately 30% of ccRCC patients presenting with localized disease develop metastases after nephrectomy[216,233]. During the past decade, several therapeutic treatments for RCC have been developed, but treatment response is varied, and development of resistance is common, which underscores the urgent need to develop a broader panel of effective therapies for ccRCC. Here, we report a synthetic lethal interaction between targeted PI3Kβ-AKT axis and loss of *SETD2* both *in vitro* (ccRCC-derived cells) and *in vivo* (ccRCC cell line-derived xenografts).

In ccRCC tumors, *SETD2* is ubiquitously haploinsufficient (>95%) as a consequence of the loss of the short of arm of chromosome 3 (3p), a phenomenon widely accepted as an early event in ccRCC transformation[14]. *SETD2* bi-allelic loss occurs in at least 20% of primary human RCC tumors, which is associated with more advanced disease and the lethal metastatic phenotype[43]. Further, bi-allelic loss of *SETD2*, or mutations rendering the protein catalytically inactive, result in loss of H3K36me3 in ccRCC-derived cells and tumors[55,234,235]. Interestingly, a study of ccRCC intratumoral heterogeneity identified distinct *SETD2* mutations across subsections of an individual tumor, suggesting a selection bias for *SETD2* mutation in the course of ccRCC development[236]. This mutation is associated with the development of metastatic disease, and the mechanisms by which this mutational event supports cellular growth have been elusive to date. Cellular signaling and the remodeling of signaling pathways likely underscores the growth advantage that emerges downstream of the nuclear and cytoplasmic process

(chromatin remodeling, genomic instability, impaired DNA repair) that have been directly attributed to *SETD2* loss.

One of the more significantly activated pathways in ccRCC is the PI3K-AKT-mTOR axis[15]. PI3Ks are a family of lipid kinases that translate numerous environmental signals from growth factors, cytokines, and other cues into signaling pathways controlling diverse biological processes, such as cell proliferation, growth, and motility among others[77]. Multiple PI3K families are known in eukaryotes. Class IA PI3Ks are heterodimers containing a p110 catalytic subunit and a p85 regulatory subunit. The genes *PIK3CA*, *PIK3CB*, and *PIK3CD* encode three highly homologous catalytic isoforms: PI3K (p110)α, PI3K (p110)β, and PI3K (p110)δ, respectively. Of note, mainly class IA PI3Ks have been implicated in cancer[71]. Further, the PI3K-AKT axis is known to be activated by gene mutations and copy number alterations (CNAs) than any other altered molecular pathway in cancer[229]. When compared to other cancers, although the PI3K-AKT pathway presents a relatively low overall mutation rate in ccRCC, the overall activation (phosphorylation levels) of AKT and downstream substrates is high[63–65].

Supporting the critical role of the PI3K-AKT pathway in ccRCC and the emerging notion as a promising druggable target, a recent study demonstrated a connection between targeted PI3Kβ inhibition with the small-molecule inhibitor TGX221 and loss of *SETD2*[230]. In this study, ccRCC-derived cells deficient for both *VHL* and *SETD2* are significantly more sensitive to TGX221 than those deficient for *VHL* alone. They also demonstrated that TGX221-treated *VHL* and *SETD2* deficient ccRCC-derived cell lines have a significantly reduced migrating and invading capacity when compared to *VHL* deficient ccRCC-derived cell lines, suggesting a novel molecular connection between PI3Kβ and SETD2. However, the mechanism underlying the crosstalk between *SETD2* loss and the targeted PI3K-AKT axis remains unknown. Our combined

data demonstrating that *SETD2* deficient ccRCC-derived cells are significantly sensitive, less migratory, and less capable of forming spheroids and that tumor formation of *SETD2* mutant xenografts is abrogated, further underscore the biological relevance of this molecular connection between SETD2 and PI3Kβ. We also reveal the critical role that a functional AKT plays in supporting growth and migration specifically in *SETD2* mutant ccRCC-derived cells. Based on our findings, we propose that in ccRCC, which typically harbors inactivating *SETD2* mutations, the PI3Kβ-AKT axis is essential for growth and migration and that when targeted, is inhibitory to cells with *SETD2* loss, therefore revealing tantalizing therapeutic applications.

Materials and Methods

Cell culture and generation of *SETD2*-null human 786-0 and A498 cells

786-0 and A498 cell lines were acquired from the American Type Culture Collection (Manassas, VA). RCC-derived *SETD2*-null 786-0 cells were generated using TAL effector nucleases targeted to exon 3 of *SETD2*, as previously described[58]. Functional truncated SETD2 (tSETD2) with wild-type or SET domain mutant (R1625C) sequences were expressed in 786-0 *SETD2* deficient cells as previously described[234]. All cells undergo annual STR analysis for genetic confirmation. All cell lines were cultured in Dulbecco's Modified Eagle Medium (DMEM, Gibco/Life Technologies, Carlsbad, CA) supplemented with 10% FBS (Gemini Bio-Products, West Sacramento, CA), non-essential amino acids, L-glutamine, penicillin, and streptomycin. All cultures were maintained at 37°C in 5% CO2.

Dose-response assays

Cells were seeded in DMEM 10% FBS in 96-well plates. 1000 cells per well were plated in quadruplicate for each cell line (*SETD2* proficient and KO 786-0 and *SETD2* mutant A498 cells) and allowed to attach to bottom of plates overnight. The following day, cells were treated with different concentrations of inhibitors (10 μM was the highest concentration, which was subsequently diluted 6 times at a 1:3 ratio and control wells had only DMSO) for 7 days and then fix/stained with 0.3% crystal violet solution followed by image analysis of the plates using an Odyssey Infrared Imaging System (LI-COR Biosciences). IC_{50} values were determined after double log-transformation of dose response curves as previously described[237]. Alternatively, cell viability was assayed with CellTiter Glo according to the manufacturer's instructions (Promega).

Cell proliferation assays

Cells were seeded in DMEM 10% FBS for proliferation in two-dimensional (2D) growth assays and fixed/stained with crystal violet. 3000 cells per well were plated in quadruplicate for each cell line (*SETD2* proficient and KO 786-0 and *SETD2* mutant A498 cells) and then allowed to grow for 7 days. Each row of a 24-well plate (three rows/plate) contained a cell line and each plate represented a time point[238]. Media and inhibitors were replenished every 2 days during the 7-day assay; adherent cells were fixed/stained with 0.3% crystal violet solution followed by image analysis of 24-well plates using an Odyssey Infrared Imaging System (LI-COR Biosciences). Integrated densities from three independent experiments were calculated for all treatments and then normalized to control (DMSO-treated cells) to assess growth rate.

Cell viability assays

Cells were seeded in DMEM 10% FBS and allowed to grow in two-dimensional (2D) viability assays and counted or fixed/stained with crystal violet as described previously[232]. 3000 cells per well were plated in quadruplicate for each cell line (*SETD2* proficient and KO 786-0 and *SETD2* mutant A498 cells) and then allowed to grow for 7-10 days in the presence of 1μM inhibitor. Media and inhibitors were replenished every 2-3 days; after 7-10 days, adherent cells were trypsinized and counted using a Coulter Counter or fixed/stained with 0.3% crystal violet solution followed by image analysis of the plates using an Odyssey Infrared Imaging System (LI-COR Biosciences). Cell number (Coulter Counter) and cell density (Crystal Violet fix/stain) for all treatments were obtained from three independent experiments and normalized to control (DMSO-treated cells) to assess cell response to inhibitors.

siRNA transfections

Cells were transfected with human SMART pool ON-TARGETplus PIK3CB (L-003019-00-0005), PIK3CA (L-003018-00-0005), PIK3CD (L-006775-00-0005), and ON-TARGETplus Non-targeting pool (D-001810-10-05) siRNAs using DharmaFECT 1 transfection reagent (T-2-001-02) (GE Dharmacon) or with human PI3-Kinase p110α (sc-39127), PI3-Kinase p110β (sc-37269), PI3-Kinase p110δ (sc-39101), and Control siRNA-A (sc37007) siRNAs (Santa Cruz Biotechnology) using Lipofectamine RNAiMax Transfection Reagent (Invitrogen) according to the manufacturer's protocol. Transfections were performed in serum-reduced, antibiotic-free DharmaFECT Cell Culutre Reagent (DCCR) (B-004500-100) (GE Dharmacon).

3D growth assays

3D growth assays were conducted in growth factor-reduced Matrigel (BD Biosciences) as described previously[239]. In brief, cells were resuspended in a 1:1 ratio in 5% Matrigel containing medium supplemented with the drug treatments. For each drug condition, cell mixture (400μL of cell mixture containing 5000/cells and 500 nM of TGX221, AZD8186, BYL719, BKM120, Idelalisib, MK2206, or DMSO) was plated in triplicate wells of a 48-well plate containing solidified Matrigel. Fresh media containing 5% Matrigel and drugs (500 nM) or DMSO were replaced every 2-3 days. After 14 days, phase-contrast pictures were taken using an Olympus CK40 microscope and colonies were counted using the GelCount scanning software.

Scratch assays

Cells were seeded in triplicate in 24-well plates such that, after 24 hours of growth, cells would be ~70-80% confluent as a monolayer (25,000 cells/well for *SETD2* proficient and KO 786-0 cells; 50,000 cells/well for *SETD2* mutant A498). The following day, a "wound" was made with a new 1 ml pipette tip across the center of the well. A straight line was scratched in one direction and another straight line perpendicular to the first line to create a cross in each well. After scratching, each well was washed twice with medium to remove the detached cells and replenished with fresh medium containing drugs (1 μM). After 48 h of cell growth, cells were fixed and stained with 20% methanol/80% water/0.5% crystal violet for 30 min, washed with water, and dried. Photos for the original wound and for the stained monolayer were taken using an Olympus CK40 microscope. Gap distances from images were measured in 3 different areas in each well. The percent wound closure was calculated from the ratio of the current wound

area to the original wound area. Please refer to the following link https://bio-protocol.org/e100 for more details.

Immunoblot analysis

Adherent cells were first washed with 1X PBS, then thoroughly dried, and consequently frozen down at -20ºC overnight. The day after, frozen cells were scraped and lysed with RIPA buffer (150mM NaCl, 1.0% IGEPAL®, 0.5% sodium deoxycholate, 0.1% SDS, and 50mM Tris, pH 8.0. [Sigma], and 1x protease inhibitor cocktail [Roche]). Lysates (20 μg) were resolved by SDS-PAGE and transferred to nitrocellulose or PVDF membranes; these were first incubated with primary antibodies at 4°C overnight, followed by incubation with HRP-conjugated anti-rabbit or anti-mouse secondary antibodies (1:10,000) (Santa Cruz Biotechnology) for 1 hour at room temperature. Immunoreactive bands were visualized by enhanced chemiluminescence (Thermo Scientific). Antibodies and dilutions: phospho-AKT-S473 (Cell Signaling 9271, 1:500), AKT (Cell Signaling 9272, 1:1500), phospho-PRAS40 (Cell Signaling 2997, 1:500), phospho-S6-S235/236 (Cell Signaling 4858, 1:500), S6 (Cell Signaling 2217, 1:1500), β-Actin (Cell Signaling 4970, 1:5000), SETD2 (Sigma HPA042451, 1:500), Histone H3K36me3 (Active Motif 61101, 1:500), Histone H3 (Abcam ab10799, 1:500), p110α (Cell Signaling 4249, 1:500), p110β (Cell Signaling 3011, 1:500), p110δ (Cell Signaling 34050, 1:500).

Xenograft studies

Mouse experiments were approved by the Vanderbilt Institutional Animal Care and Use Committee. Female NOD *scid* gamma (NSG) mice (Jackson Laboratories) were used. A498 or 786-0 cells ($1x10^7$) were suspended in DMEM and Matrigel (BD Biosciences, San Jose, CA) at

1:1 ratio and injected subcutaneously (s.c.) into the right flank of each mouse. Approximately 4 weeks later, mice bearing tumors measuring ≥150 mm^3 were randomized to treatment with 1) vehicle (control) or 2) AZD8186 (30mg/kg/day via orogastric gavage). Animal weights (data not shown) and tumor diameters (with calipers) were measured twice weekly and tumor volume was calculated with the formula: volume = ($width^2$ x length)/2.

Statistical analyses

Unless otherwise indicated, significant differences ($p<0.05$) were determined by ANOVA using GraphPad Prism software.

CHAPTER IV

EXTRACELLULAR VESICLES IN CANCER

Abstract

Research in the area of extracellular vesicles (EVs) has grown exponentially in the past decade. These evolutionary conserved vesicles are now appreciated as important carriers of protein, nucleic acids, lipids, metabolites, and other biologically active molecules that mediate cell-to-cell communication. This review highlights the advancements made in EV biology in cancer. We discuss EV subtypes and their biogenesis before delving into key studies describing their multitude of roles in cancer and diagnostic potential. Ongoing studies to fully elucidate their functions will deepen our understanding of their contributions to tumorigenesis and inform the development of EV-based biomarkers and therapies.

Introduction

First described in the 1960s as 'platelet dust' released during the coagulation cascade[240], EVs represent a heterogenous population of vesicles each with their own distinct properties, sizes, and origins. Although they were originally thought to contain nonfunctional protein as a way for cells to get rid of waste products[241,242], emerging evidence suggests they represent a novel method by which cells can communicate with adjacent or distant cells[243]. Nearly all cells are known to secrete EVs, and their cargo is thought to directly reflect their cellular origins,

bringing up the tantalizing possibility of using EVs as liquid biomarkers for cancer[244]. EVs are commonly isolated from the conditioned medium of cultured cells, though they have also been obtained from patient biofluids such as serum and urine. Techniques for isolating these vesicles include ultracentrifugation, density gradient centrifugation, size exclusion chromatography, immunoprecipitation, polymer-based precipitation, and asymmetric flow field flow fractionation, to name a few[245].

In tumors, EVs perform many different functions that influence almost every hallmark of cancer[246]. EVs interact with tumor cells and non-tumor cells by a variety of mechanisms, including receptor-ligand binding, phagocytosis, clathrin-mediated endocytosis, and macropinocytosis[247], and delivery of their cargo requires endosomal acidification and membrane fusion[248]. Additionally, different signals and stresses can alter EV secretion and cargo from cancer cells, highlighting the therapeutic potential of targeting EVs. In the subsequent sections, we examine the perturbations induced by EVs in the tumor landscape and their potential as diagnostic biomarkers. Finally, we address the lingering barriers to studying and utilizing EVs for clinical applications.

Biogenesis and Secretion of Extracellular Vesicles

Many EVs have been characterized, though in general, they are divided into two groups based on size: small (sEVs) and large (lEVs) [Table 2]. Additionally, vesicles are often classified based on their subcellular origins and biogenesis mechanisms. The machinery that orchestrates the biogenesis and secretion of EVs is complex and is still being elucidated[249] [Figure 17].

Below, we discuss the current knowledge on the generation of exosomes and microvesicles, the two most popular studied types of vesicles.

Type of EV	Origin	Size Class	Diameter
Oncosome	Plasma Membrane	Large	1-10μm
Apoptotic Body	Apoptosis	Large	1-5μm
Exopher	Unknown	Large	3.5μm
Microvesicle/Ectosome	Plasma Membrane	Large	100nm -1μm
Exosome	Multivesicular Body	Small	30-150nm
Exomere	Unknown	Nanoparticle	30-50nm

Table 2. Types of extracellular vesicles

Table listing the types of extracellular vesicles, their biogenesis origin, size class, and diameter.

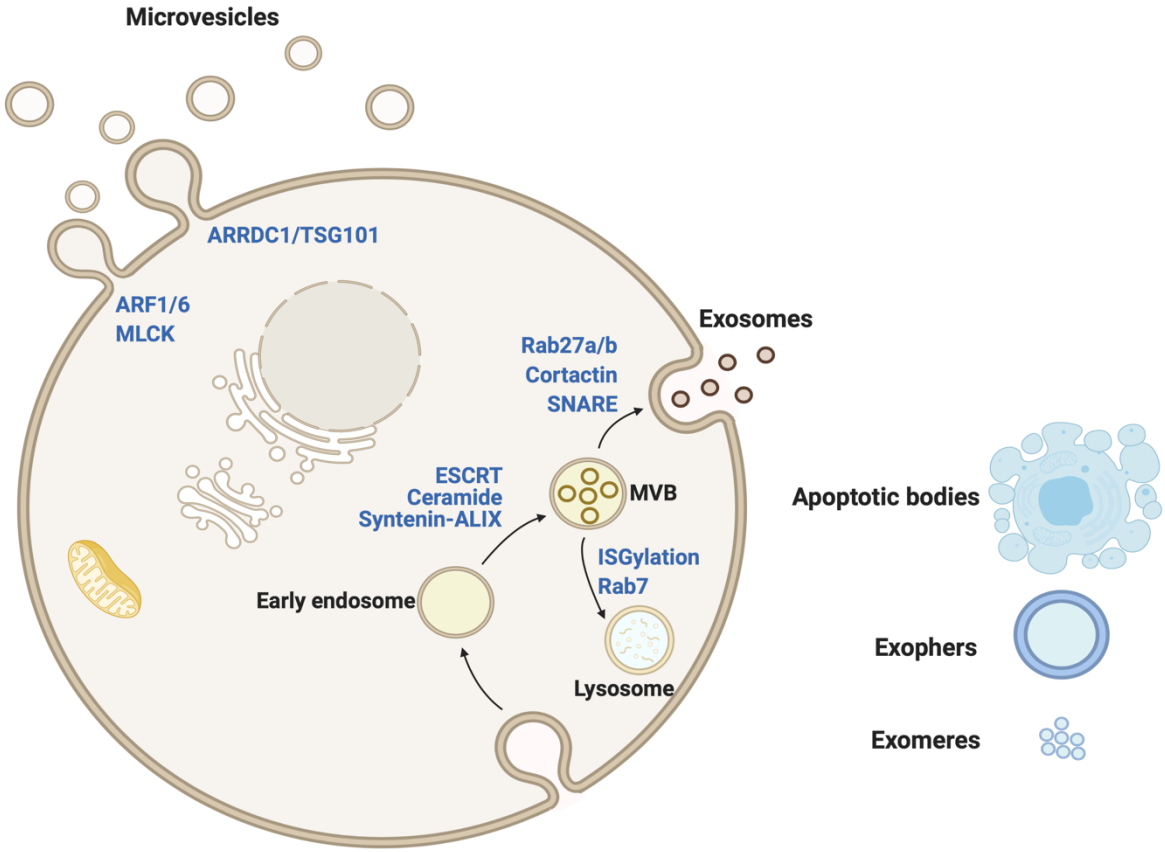

Figure 17. Biogenesis and secretion of extracellular vesicles

Microvesicles bud directly from the plasma membrane with the help of small GTPases ADP Ribosylation Factor 1 (ARF1) or ARF6, which activate myosin light chain kinase (MLCK) to induce scission of the vesicle. Another class of microvesicles uses Arrestin domain containing protein 1 (ARRDC1) to recruit tumor susceptibility gene 101 (TSG101) to the plasma membrane. On the other hand, exosomes are derived from the endosomal pathway. Intraluminal vesicles (ILV) bud inward from endosomes to form multivesicular bodies (MVBs). Several pathways have been described to induce ILV formation, including the Endosomal Sorting Complex Required for Transport (ESCRT), ceramide, and syndecan-syntenin-ALIX pathways. ISGylation of ESCRT proteins or activation of Rab7 promotes MVB trafficking to the lysosome, which degrades the contents of the MVB. However, MVBs can also traffic along the

cytoskeletal network to dock on the plasma membrane with the help of Rab27a/b and cortactin and fuse with the plasma membrane using SNARE proteins to release their ILVs into the extracellular milieu as exosomes. Apoptotic bodies are a type of large EV that form when a cell undergoes apoptosis, while the origins of exophers and exomeres are unknown.

Exosome biogenesis and secretion

Exosomes originate from intraluminal vesicles (ILVs) that bud inward from an early endosome, which matures into a late endosome or multivesicular body (MVB). Several exosome biogenesis pathways have been described. The best characterized pathway is the Endosomal Complex Required for Transport (ESCRT) pathway, the same pathway enveloped retroviruses use for egress[249], in which four ESCRT complexes act in sequential order[250]. ESCRT-0 recruits ubiquitinylated protein and clusters them to the limiting membrane of endosomes. ESCRT-I recognizes the ubiquitylated protein and activates ESCRT-II to induce budding. ESCRT-III, which cleaves the budding vesicle, is recruited by ALG-2 Interacting Protein X (ALIX). ALIX acts as an intermediary between ESCRT-III and ESCRT-I, binding the ESCRT-III protein charged MVB protein 4A (CHMP4A) and the ESCRT-I protein tumor susceptibility gene 101 (TSG101)[251]. Several studies revealed that ALIX can mediate exosome biogenesis in an alternative ESCRT pathway involving syndecan heparan sulfate proteoglycans and their cytoplasmic adaptor syntenin-1. In the syndecan-syntenin-ALIX pathway, ALIX interacts with the LYPX(n)L domain of syntenin to induce ILV formation[252] in a process regulated by heparanase, Src kinase, ADP Ribosylation Factor 6 (ARF6), and phospholipase D2[253–255]. Specifically, ARF6 activates phospholipase D2 to produce phosphatidic acid, which promotes inward curvature of the MVB limiting membrane[253].

However, even in the absence of the ESCRT pathway, exosomes have been found to be produced and released from cells[256]. ESCRT-independent pathways involving lipids and RAB proteins have since been described. Lipidomic studies found enrichment of sphingomyelin, ceramide, cholesterol, and phosphatidylserine in exosomes[257,258]. Ceramides concentrated in MVBs exert physical forces to induce inward budding of vesicles in MVBs[259]. Inhibition of

neutral sphingomyelinase 2 (nSMase2) with GW4869 reduces ILV budding and exosome secretion in an ESCRT-independent manner[260], though it also promotes a compensatory increase in microvesicles from the plasma membrane[261] and cell death in myeloma cells[262]. Thus, one should be cautious when interpreting experiments involving GW4869. A recent study implicated Rab31 in an ESCRT-independent pathway in which this GTPase clusters flotillins at lipid rafts to drive receptor tyrosine kinase sorting into ILVs[263]. It is unclear whether a single MVB can form exosomes through multiple mechanisms or whether there are unique MVB populations within a cell. Thus, future investigations will need to delineate how these pathways work in concert to control exosome secretion and whether each pathway generates different kinds of exosomes with unique cargoes.

MVBs can fuse with lysosomes for degradation or traffic to the plasma membrane where they dock with the help of Rab27a/b and cortactin and release their vesicles as exosomes into the extracellular space[264]. The regulatory processes determining whether a MVB is targeted for degradation or for secretion are still unclear, though they likely involve components of the ESCRT pathway and Rab proteins. A recent study showed Type I interferon signaling upregulates Interferon-Stimulated Gene 15 (ISG15), a ubiquitin-like protein that, when conjugated with ESCRT proteins, promotes lysosomal degradation of MVBs[265]. Small GTPases and synaptosomal-associated protein (SNAP) Receptor (SNARE) proteins also play critical roles in MVB trafficking and fusion with the plasma membrane to release exosomes. Rab31 inactivates Rab7, thus directing MVBs to the plasma membrane to release ILVs as exosomes instead of trafficking to the lysosome for degradation[263]. Calcium also stimulates exosome release via the calcium-binding protein Munc13-4, which regulates Rab11 trafficking of MVBs[266]. Ral GTPases have been found to regulate MVB formation and interact with the

SNARE protein syntaxin-5 at the plasma membrane to promote exosome secretion[267]. Finally, phosphorylation of SNARE protein SNAP23 at serine 110 induces fusion of MVB with plasma membrane[268].

Microvesicle biogenesis and secretion

In contrast to exosomes, microvesicles (also called ectosomes or oncosomes among other names) directly bud off the plasma membrane and range in size from 50-1000nm in diameter, and their biogenesis mechanisms are not as well characterized. Microvesicles are thought to be shed by outward budding and pinching of the plasma membrane, leading to release of these vesicles into the extracellular environment[269]. The regulation of microvesicle blebbing and fission involves redistribution of lipids, flippases, and contraction of actin and myosin cytoskeleton under the control of the small GTPase RhoA[270,271]. In melanoma, ARF6 regulates the secretion of microvesicles by recruiting ERK, which subsequently activates myosin light-chain kinase (MLCK)[272]. ARF6 also sorts specific cargo into melanoma-derived microvesicles, including β1 integrin and MHC class I[272]. However, in breast cancer, ARF1, and not ARF6, was shown to drive microvesicle secretion[273]. Why one cell type uses one ARF isoform over others and the applicability of this system in other cancer types is not well understood.

There is also evidence that microvesicle biogenesis involves ESCRT proteins, the same machinery described above in exosome biogenesis. Arrestin domain containing protein 1 (ARRDC1), which contains a PSAP domain similar to HIV-1 Gag protein's PTAP domain, localizes to the cytosolic side of the plasma membrane and recruits the ESCRT-1 protein TSG101 to initiate budding of vesicles called ARRDC1-mediated microvesicles (ARMMs)[274]. However, even though they use similar machinery and are of similar size, ARMMs are distinct

from exosomes and lack other endosomal markers typically found in exosomes[274]. This study suggests shared biogenesis machinery of exosomes and microvesicles, and further investigations are warranted to identify specific components of EV subtype biogenesis[275].

Due to the overlap in biogenesis mechanisms, it can be difficult to distinguish vesicle subtypes. Consequently, many studies unknowingly isolate a mixed population of EVs due to the limitation of current techniques to purify specific EV subtypes[276]. Thus, for the remaining sections describing the functions of EVs in tumors, we preferentially use the general terms "small extracellular vesicle" and "large extracellular vesicle"[277]. However, we will use the term "exosome" when a particular study identified their EVs as endosomal in origin, and the term "microvesicle" when their origin is from direct budding from the plasma membrane.

EVs Enhance Tumor Growth

EVs can deliver oncogenic cargo to cancer cells or other cells in the tumor microenvironment to promote tumor growth. For example, ectopic expression of EGFRvIII in U373 glioma cells led to the transfer of EGFRvIII and activation of the MAPK and Akt signaling pathways in U373 glioma cells that do not harbor this mutation[278]. Gain-of-function mutant p53 packaged in tumor-derived sEVs reprogrammed fibroblasts to a cancer-associated phenotype, enhancing tumor growth *in vitro* and *in vivo*[279]. In the reverse direction, cancer-associated fibroblasts (CAFs) were shown to secrete unshielded RNA into EVs that activate retinoic acid-inducible gene I (RIG-I) in breast cancer cells to enhance growth[280]. Furthermore, breast cancer-derived EVs, but not normal cells, were found to contain the RNA induced silencing complex (RISC)-loading complex proteins Dicer, TAR RNA Binding Protein (TRBP), and Ago2 to

process pre-miRNAs into mature miRNAs in a cell-independent manner[281]. Treating normal human mammary epithelial cells with these EVs altered their gene expression profile and promoted tumor formation in mice[281]. Breast cancer-derived EVs also contain tissue transglutaminase and fibronectin that can be delivered to normal epithelial cells and fibroblasts to induce anchorage-independent growth[282]. Finally, amphiregulin-containing sEVs altered EGFR trafficking and promoted intestinal tumor organoid growth[283]. Taken together, these data indicate that EVs can disseminate oncogenic cargo that significantly contribute to primary tumor growth.

EVs Promote Tumor Cell Migration and Metastatic Niche Formation

Cell migration is a complex and tightly coordinated process that allows cancer cells to spread away from the primary tumor. Recently, EVs have been shown to play critical roles in cell motility. Fibroblast EVs stimulated breast cancer cell motility and metastasis by activating Wnt-planar cell polarity (PCP) signaling[284]. Matrix metalloproteinases (MMPs) secreted in EVs can degrade the extracellular matrix (ECM) and facilitate cell invasion[285]. ECM proteins have also been found to be packaged in exosomes, which form an adhesive substrate that controls the speed and directional motility of cancer cells in an autocrine manner[286]. In live cell imaging experiments, fibrosarcoma cells were observed to secrete exosomes at the leading edge, make contact with them via filopodia, and migrate toward them[287]. In another recent study using an elegant *in vivo* Cre-LoxP system, malignant breast cancer cells were found to secrete EVs that reprogram less malignant cells with increased migratory and metastatic capacity[288]. Breast cancer

cells can also secrete sEVs that make normal mammary epithelial cells more migratory via mitochondrial reprogramming[289].

EVs have also been found to be key mediators in setting up a premetastatic niche to mediate metastatic disease. Peinado *et al.* demonstrated this functional role for EVs when they showed that tumor-derived EVs reprogrammed bone marrow-derived cells to express higher levels of MET, which promoted their migration to the lungs and lymph nodes to facilitate tumor colonization[290]. Another study showed that cell migration inducing and hyaluronan-binding protein (CEMIP) was enriched in breast and lung cancer EVs that were taken up by endothelial and microglial cells in the brain, leading to upregulation of pro-inflammatory cytokines known to remodel brain vasculature and facilitate metastasis[291]. Breast cancer cells can also take up astrocyte-derived EVs containing miR-19a, which downregulated *PTEN* in the breast cancer cells and promoted metastasis to the brain[292]. In addition, integrins packaged in EVs redirected cancer cells to organs where they normally do not metastasize to, and patient plasma EVs with these integrin profiles could predict sites of metastasis[293]. These EV-associated integrins were observed to interact with extracellular matrix components at the metastatic site, such as $\alpha_5\beta_1$ and $\alpha_6\beta_4$ binding to fibronectin and laminin-332, respectively. Finally, melanoma-derived EVs were shown to downregulate Type I interferon signaling in the lungs to establish a premetastatic niche[294]. Together, these findings highlight the ability of EVs to modulate cell migration and metastasis.

EVs Facilitate Angiogenesis

The generation of new blood vessels is a critical process in the tumor microenvironment in order to supply nutrients that support rapid tumor growth. Interestingly, a variety of different cargo packaged in tumor-derived EVs have been implicated in angiogenesis. For instance, different isoforms of vascular endothelial growth factor (VEGF), one of the most well characterized mediators of neovascularization, have been described on the surface of tumor-derived EVs that activated vascular endothelial growth factor receptor 2 (VEGFR2) on endothelial cells independent of uptake[295,296]. These variant isoforms of VEGF associated with EVs could not be neutralized by bevacizumab, suggesting that $VEGF^+$ EVs in the tumor microenvironment could promote angiogenesis even in the presence of anti-angiogenic agents and thus serve as a potential resistance mechanism[295,296]. In addition, EphB2 on head and neck cancer sEVs induced angiogenesis *in vitro* and *in vivo* by activating ephrin reverse signaling[297]. Although the ephrin signaling pathway is canonically thought of as a juxtacrine signaling pathway, this finding highlights a unique role for EVs to drive angiogenesis at a distance and independent of cell-to-cell contact.

EVs can also directly deliver cargo to induce blood vessel formation. EVs packaging microRNA that downregulate Kruppel-like factors 2 and 4[298] or prolyl-hydroxylase domain (PHD) proteins PHD1 and PHD2[299] promoted angiogenesis in multiple tumor models. TGFβ1 in prostate cancer-derived EVs induced the formation of myofibroblasts which were pro-angiogenic[300]. In breast cancer, annexin A2, which interacts with tissue plasminogen activator, was enriched in breast cancer-derived EVs that induced angiogenesis *in vitro* and *in vivo*[301]. Furthermore, glioblastoma secretes miRNA into EVs that induce angiogenesis[302], and these cells secreted EVs that further stimulated angiogenesis when grown under hypoxic conditions[303]. Together, these findings highlight the importance of tumor-derived EVs in angiogenesis, and

future studies investigating the synergy between EV cargo with secreted soluble factors during this process are warranted.

EVs in Immune Crosstalk

A main hallmark of cancer is evasion of the immune system, and it has been a long-term goal in oncology to harness the immune system to fight cancer. With the advent of immunotherapy, the treatment landscape for cancer has changed dramatically in the past decade. These highly efficacious agents can even lead to durable responses in patients, though there are numerous barriers in the tumor microenvironment to immune cell function[131], including EVs. Tumor-derived EVs were shown to downregulate the activating cell surface receptor NKG2D on NK and CD8 T cells[304]. Fas ligand (FasL) and tumor necrosis factor-related apoptosis-induced ligand (TRAIL) packaged in colorectal cancer EVs induced T cell death[305]. PD-L1, a main target of immune checkpoint blockade, on EVs abrogated activation of T cells and thus led to T cell anergy[198,199]. Reducing EV secretion with knockdown of Rab27a led to regression of tumors, which could be reversed by intravenous injection of exogenous PD-L1+ EVs[200]. Together, these findings reveal that EVs are a major mechanism by which tumors suppress the immune system, and inhibiting EV secretion can enhance anti-tumor immunity.

At the same time, EVs have also been shown to activate components of the immune system. Chimeric Antigen Receptor (CAR) T cells, which are genetically engineering T cells with specific receptors to target cancer antigens, were found to secrete CARs into sEVs that can induce anti-tumor immunity[306]. Tumor-derived EVs can also transfer antigens to dendritic cells, which present these antigens to and activate anti-tumor T cells[307]. Furthermore, melanoma cells

with poor metastatic potential secreted exosomes that elicited an innate immune response that abrogated lung metastasis[308]. A recent study showed inactivation of the Hippo pathway in multiple tumor models induced anti-tumor immunity by increasing secretion of EVs with nucleic acids that activated a type I interferon response[309].

EVs from immune cells can also directly impact cancer cells and cells in the tumor microenvironment. For example, DC-derived EVs were shown to contain mIR-186, which downregulated *MYCN, AURKA, TGFBR1* and *TGFBR2* in neuroblastoma cells to inhibit their growth[310]. Tumor-associated macrophages (TAMs) were shown to secrete a HIF-1α stabilizing long noncoding RNA that enhanced aerobic glycolysis in breast cancer cells[311]. In addition, alveolar macrophages secrete EVs with suppressor of cytokine signaling 3 (SOCS3) which inhibited STAT3 signaling and proliferation of lung cancer cells[312]. Thus, immune cells also communicate with tumor cells via EVs to influence their oncogenic properties.

EVs in Cancer Metabolism

Metabolism underlies every cellular process, and dysregulated cellular metabolism is an emerging hallmark of cancer[86,313]. There is increasing evidence that EVs are metabolically active and affect the metabolism of recipient cells[314]. For example, prostate cancer EVs were shown to perform glycolysis and generate ATP[315]. Furthermore, treatment with anti-angiogenic tyrosine kinase inhibitors increased $GLUT1^+$ EV secretion from RCC cells and modulated the glycolytic activity of sEVs [Lim *et al. Cancer Gene Therapy* under revision]. C13-labeling studies showed that EVs derived from CAFs inhibited oxidative phosphorylation while stimulating glycolysis and reductive carboxylation of glutamine in prostate and pancreatic cancer cells[316]. Metabolomic

studies revealed an enrichment of amino acids such as glutamine in these EVs, which could subsequently be transferred to tumor cells to fuel the TCA cycle in nutrient-deprived conditions. Finally, prostate cancer lEVs called large oncosomes, but not exosomes, were found to alter glutamine metabolism in recipient tumor cells by transferring the protein GOT1[317]. These data suggest that EVs can influence the nutrient composition of the tumor microenvironment and even alter metabolic programs in tumor cells.

EVs Mediate Drug Resistance

EVs have also been shown to key mediators of drug resistance in cancer. In a recent study, Qu *et al.* describe a long non-coding RNA packaged into EVs that were taken up by sensitive cells where they upregulated AXL and c-MET expression[318], which have previously been shown to mediate Sunitinib resistance[319]. Another study showed that TAMs secrete miRNA into EVs that were taken up by pancreatic cancer cells where they increased the triphospho-nucleotide pool and cytidine deaminase, which inactivates gemcitabine[320]. In breast cancer, EVs enriched with survivin promoted cell survival in breast cancer cells treated with paclitaxel[321]. In addition, transient receptor potential channel 5 (TrpC5) packaged in chemo-resistant breast cancer EVs traps Adriamycin in EVs[322]. Furthermore, stromal cells can package RNA into EVs that activate RIG-I and STAT1 signaling, which cooperate with NOTCH signaling to induce radiation and chemotherapy resistance in breast cancer cells[323]. These studies collectively demonstrate that EVs can facilitate resistance against multiple anti-cancer therapies.

EVs as Cancer Biomarkers

Since tumor cells behave differently from normal cells, it is thought that the cargo of EVs derived from malignant tissue is different from EVs secreted from non-malignant tissue. This idea has been demonstrated in several studies. Serum from EGFRvIII-mutated glioblastoma patient serum, but not healthy donor serum, were found to contain EVs that harbor this mutated protein[324]. Moreover, these EGFRvIII^{+} EVs were not detected two weeks after patients had their tumor resected, indicating that EGFRvIII in EVs could potentially be used for disease surveillance[324]. Pancreatic cancer-derived sEVs were shown to be enriched with a proteoglycan Glypican-1, which may identify early pancreatic cancer lesions[325]. However, this was challenged with a subsequent study, which used liquid chromatography-tandem mass spectrometry (LC-MS) to show that Glypican-1 was not significantly elevated in pancreatic cancer sEVs – rather, an EV miRNA signature outperformed glypican-1 EV levels as a marker for pancreatic cancer[326]. This discrepancy may stem from variations in cohorts and differences in methodology for analyzing protein cargo in the EVs (antibody capture versus LC-MS). In a landmark study, Hoshino *et al.* performed proteomic analysis on EVs from over four hundred human tissue, blood, and other bodily fluid sample types spanning eighteen different cancer types[327]. They distinguished tumor-derived EV markers from non-malignant EVs and even defined unique EV signatures across different cancer types. Their findings indicate that EVs could be leveraged as a screening tool for early detection for cancer, though validation in subsequent cohorts of patients with and without cancer is needed.

Conclusion

A growing body of EV research over the past two decades has unraveled the diverse roles these vesicles play across multiple cancer types. With the explosion of interest in EVs, the future of the field holds great promise, though there are plenty of knowledge gaps still left to be filled. Efforts aimed at uncovering their contributions to tumorigenesis will be crucial to understanding how tumors behave and potentially allow us to harness EVs for therapeutic and diagnostic purposes.

However, significant barriers must be addressed in order to advance the EV field. For example, there is still a great need to develop better tools for tracking and studying EVs *in vivo*. The Cre-LoxP system described earlier to track EV uptake[288,328] cannot distinguish what type of EV was taken up by recipient cells nor distinguishes EV uptake from other transfer mechanisms. Recently, a brighter, more stable pHLuorin-CD63 tag was described to visualize exosome secretion and uptake in live cells[287]. Utilization of this reporter in future studies to track the exosome life cycle in diverse cancer types offers new avenues for elucidating their cellular effects. In addition, several groups have drawn attention to the heterogeneity of vesicles that are isolated with multiple techniques[329], highlighting that current purification methods need to be refined without sacrificing yield. Due to this heterogeneity, fluorescent reporters used in EV studies will miss EV subpopulations that lack the particular marker. Improvements in technologies such as flow cytometry[330] will bring us closer to achieving single EV resolution and unveiling molecular signatures that define EV subtypes.

Although there is great interest in harnessing EVs for clinical applications, biodistribution studies of EVs indicate that they are rapidly cleared *in* vivo by the liver, spleen, and

kidneys[331,332]. Moreover, the mechanisms governing EV cargo sorting, uptake, and organotropism are still poorly understood. However, their presence in easily accessible bodily fluids, such as blood and urine, may one day replace or supplement invasive procedures in order to diagnose or monitor tumor progression. The landmark study by the Lyden group has led us closer to realizing the potential of using EVs for cancer surveillance, though the results of this study, as well as others looking at the diagnostic role for EVs, still require larger validation studies. Additionally, studies comparing the diagnostic value of EVs to that of cell-free DNA, circulating tumor cells, or other cancer biomarkers are lacking. Finally, the practicality of isolating EVs from patient samples, which is hampered by low yields and costly equipment such as ultracentrifuges, remains to be seen, though highly sensitive methods to detect circulating tumor EVs are in the development pipeline[333].

CHAPTER V

SUNITINIB AND AXITINIB INCREASE SECRETION AND GLYCOLYTIC ACTIVITY OF SMALL EXTRACELLULAR VESICLES IN RENAL CELL CARCINOMA

Aaron R. Lim[1,2], Benjamin G. Vincent[3], Alissa M. Weaver[2,4,5], W. Kimryn Rathmell[1,6,7]

[1]Department of Medicine, Division of Hematology and Oncology, Vanderbilt University Medical Center, Nashville, TN 37232, [2]Program in Cancer Biology, Vanderbilt University School of Medicine, Nashville, TN 37232, [3]Lineberger Comprehensive Cancer Center; Department of Medicine Division of Hematology and Oncology, Department of Microbiology and Immunology, Curriculum in Bioinformatics and Computational Biology, Computational Medicine Program, University of North Carolina at Chapel Hill, Chapel Hill, NC 27599, [4]Department of Pathology, Microbiology, and Immunology, Vanderbilt University Medical Center, Nashville, TN 37232, [5]Department of Cell and Developmental Biology, Vanderbilt University School of Medicine, Nashville, TN 37232, [6]Vanderbilt-Ingram Cancer Center, Vanderbilt University Medical Center, Nashville, TN 37232, [7]Vanderbilt Center for Immunobiology, Vanderbilt University Medical Center, Nashville, TN 37232

The work presented in this section was accepted for publication in *Cancer Gene Therapy* and has been reproduced with the permission of the journal and my co-authors.

Abstract

Extracellular vesicles (EVs) encompass a wide range of vesicles that are released by all cell types. They package protein, nucleic acids, metabolites, and other cargo that can be delivered to recipient cells and affect their phenotypes. However, little is known about how pharmaceutical agents can alter EV secretion, protein and metabolic cargo, and the active biological processes taking place in these vesicles. In this study, we isolated EVs from human renal cell carcinoma (RCC) cells treated with tyrosine kinase inhibitors (TKIs) Sunitinib and Axitinib. We found these TKIs increase the number of large (lEVs) and small extracellular vesicles (sEVs) secreted from RCC cells in a dose-dependent manner. In addition, quantitative proteomics revealed that metabolic proteins are enriched in sEVs secreted from Sunitinib-treated cells. In particular, the glucose transporter GLUT1 was enriched in sEVs purified from TKI-treated cells. These sEVs displayed increased glucose uptake and glycolytic metabolism compared to sEVs released from vehicle-treated cells. Overexpression of GLUT1 in RCC cells augmented GLUT1 levels in sEVs, which subsequently displayed higher glucose uptake and glycolytic activity. Together, these findings suggest that these TKIs alter metabolic cargo and activity in RCC sEVs.

Introduction

The incidence of kidney cancer continues to rise in the United States, with over 70,000 new cases diagnosed last year[334]. Greater than 90% of kidney cancers are classified as renal cell carcinoma (RCC), with clear cell (ccRCC) being the most common histologic subtype[14]. The

majority of ccRCC tumors lose the tumor suppressor von Hippel-Lindau (VHL), leading to constitutive activation of downstream hypoxia-inducible factor (HIF) signaling pathways. Among the canonical targets of HIF transcriptional activation include glucose transporter type 1 (GLUT1), hexokinase, and lactate dehydrogenase, fueling glycolytic metabolism[335], and vascular endothelial growth factor (VEGF), driving regional angiogenesis in a paracrine manner[336] and promoting tumor progression via both paracrine and autocrine signals[337].

Based on this molecular understanding of RCC, the first tyrosine kinase inhibitor (TKI) targeting vascular endothelial growth factor receptor (VEGFR) was approved in 2005 to treat RCC patients[9]. Today, the FDA has approved several TKIs that are currently in clinical use. These agents are high potency ATP analogues that competitively inhibit tyrosine kinases and are selected for their activity toward VEGFR, although several kinases are targeted by each of these agents[338]. Notable examples include the small molecule TKIs Sunitinib and Axitinib. Responses to Sunitinib and Axitinib have led to their approval as single agents or, in the case of Axitinib, in combination with immunotherapy in the first line treatment of RCC[338]. Unfortunately, the emergence of resistance to these agents is nearly universal[121]. Additionally, although some patients show durable responses with combination VEGFR TKI and immune checkpoint blockade regimens, such as Axitinib and Pembrolizumab, responses are unpredictable and many will not respond to this treatment[125,126]. In fact, up to 12% of patients demonstrate intrinsic resistance to dual VEGFR TKI and immunotherapy regimens[125,126]. Thus, revealing the effects of anti-angiogenic targeted agents on tumor cells and in the tumor microenvironment will have real world implications for future enhancements to front line single agent therapy and for understanding effects that could influence immune combinations.

Several resistance mechanisms to anti-angiogenic TKIs have been proposed in RCC[121]. Interestingly, it was recently shown that extracellular vesicles (EVs) from RCC cells can transfer resistance to Sunitinib by delivering a long non-coding RNA that increases AXL and c-MET expression[318]. Originally thought to package "junk" secreted from cells, EVs have now been implicated in several areas of tumor biology, including cell migration and metastasis, angiogenesis, tumor immunity, and metabolism[243]. EVs are recognized as a distinct form of cell-to-cell communication by delivering their cargo to recipient cells[243], and they can also perform cell-independent functions including energy metabolism[339]. EVs can be loosely categorized into two main groups: large extracellular vesicles (lEVs) and small extracellular vesicles (sEVs)[249]. lEVs are larger in size (50 nm to 1 micron in diameter) and bud outward from the plasma membrane[269]. sEVs range in size between 30-150 nm in diameter and may include both small microvesicles that bud from the plasma membrane as well as exosomes that originate from intraluminal vesicles (ILVs) formed within late endosomal multivesicular bodies (MVBs)[249].

The regulation of EV secretion and cargo packaging likely depends on the physiologic state of the cell[340]. External stimuli, in particular hypoxia and acidic environments, have been shown to increase EV secretion from tumors[341–344]. Pharmacologic agents affecting EV secretion are emerging, and the spectrum of TKI effects, especially on EV secretion and cargo, is not fully understood, despite the widespread use of these agents for RCC and other tumor types.

In this study, we explore the effects of anti-angiogenic TKIs on EV metabolism and secretion from RCC cells. We observed that treatment with Sunitinib or Axitinib fundamentally alters the extent of vesicle secretion as well as the metabolic protein cargo and overall metabolic activity of the sEVs. Our results demonstrate a previously unknown consequence on EV biology

when anti-angiogenic TKIs are used to treat RCC and reveal a potential role for EVs to modulate the metabolic composition of the tumor microenvironment in RCC.

Materials and Methods

Cell culture

786-0, A498, and 293FT cell lines were acquired from the American Type Culture Collection (ATCC). 786-0 cells were cultured in RPMI 1640 (Corning, Catalog #10040CV), whereas A498 and 293FT cells were cultured in DMEM (Gibco, Catalog #11965118). Both RPMI 1640 and DMEM were supplemented with 10% FBS (Gemini Bio-Products, Catalog #100106), penicillin, and streptomycin (Corning, Catalog #30002CI). Cells were maintained at 37°C in 5% CO_2. All cells underwent annual short tandem repeat analysis (ATCC) for genetic confirmation and monthly mycoplasma testing (Applied Biological Materials, Catalog #G238).

Virus production and infection

Empty vector and hGLUT1 expression constructs were purchased from Genecopoeia. Constructs were maxiprepped with NucleoBond Xtra Maxi Endotoxin-Free (Macherey-Nagel, Catalog #740424.10), and then transfected into 293FT cells with pMD2.G and psPAX2. pMD2.G and psPAX2 were gifts from Didier Trono (Addgene plasmids #12259 and #12260, respectively). Lentivirus was collected, filtered through a 0.45 μm filter, and then 786-0 cells were infected with lentivirus plus polybrene. Cells were treated with puromycin to select for positive clones.

Isolation of extracellular vesicles

Extracellular vesicles were isolated as described previously[286]. Briefly, cells were plated into T-225 flasks and allowed to reach 60-70% confluence overnight. The cells were washed with PBS three times, and then Opti-MEM media with DMSO or Sunitinib or Axitinib (Selleckchem, Catalog #S1042 and S1005, respectively) was added. After incubation at 37°C in 5% CO_2 for 48 hours, the cell count and viability were assessed with trypan blue in a TC20 automated cell counter (Bio-Rad). Only samples with cell viability greater than 95% were used for further studies. The media was collected and sequentially spun at 300*g* for 10 minutes, 2000*g* for 20 minutes, 10,000*g* for 30 minutes, and 100,000*g* for 18 hours at 4°C in a 45 Ti rotor to pellet live cells, dead cells and debris, lEV, and ultracentrifuged (UC)-sEV, respectively. After the 10,000*g* spin, the pellet was resuspended in sterile PBS and spun at 10,000*g* for one hour in a TLA-110 fixed angle rotor in a tabletop ultracentrifuge (Beckman). The resulting lEV pellet was then resuspended in sterile PBS. To purify the UC-sEVs from protein aggregates and lipoproteins, the 100,000*g* pellets were washed with sterile PBS and spun in a TLA-110 fixed angle rotor in a tabletop ultracentrifuge at 100,000*g* for 6 hours, and the subsequent pellet was resuspended in sterile PBS and loaded onto an iodixanol gradient. The iodixanol gradient was prepared by diluting OptiPrep (60% w/v aqueous iodixanol, Millipore Sigma, Catalog #D1556) with 0.25M sucrose/10mM Tris, pH 7.5 to form 40% w/v, 20% w/v, 10% w/v, and 5% w/v from the bottom to the top of a 14 x 95 mm Ultra-clear tube (Beckman, Catalog #344060). A continuous gradient was made by spinning at 100,000*g* in a SW40 Ti rotor for 18 hours. Twelve 1mL fractions were collected from the top and washed in sterile PBS, and the fractions were subsequently pelleted in a TLA-110 fixed angle rotor in a tabletop ultracentrifuge at 100,000*g* for 3.5 hours. The resulting pellets were resuspended in sterile PBS. The ZetaView analyzer

(Particle Metrix GmbH) was used to analyze the size and concentration of particles in EV samples.

Transmission electron microscopy

Transmission electronic microscopy was utilized to visualize purified EV samples by negative staining as previously described[297]. Briefly, formvar carbon film-coated grids (FCF-200-Cu; Electron Microscopy Sciences) were washed with water and then with 100% ethanol. 7-10 µL of sample was pipetted onto parafilm, and the formvar carbon film-coated grids were placed on top of the sample for 1-5 minutes at room temperature. The grids were then stained with 2% phosphotungistic acid, pH 6.1 for 10-20 seconds at room temperature and imaged with a FEI Tecnai T12 transmission electron microscope (120 kV LaB6 source), Gatan cryotransfer stage, and AMT XR41-S side mounted 2Kx2K CCD camera, 2102 SC.

Quantitative proteomics

Samples were reduced with 5 µL of 200 mM TCEP at 55°C for 1 hour and were carbamidomethylated by addition of 375 mM Iodoacetamide for 30 minutes in the dark at room temperature. Protein samples were then precipitated with ice-cold acetone overnight at -20°C. Following precipitation, samples were centrifuged at 18,000*g* at 4°C, and precipitates were washed with cold acetone, dried, and reconstituted in 100 mM TEAB (pH 8.0). Samples were digested with sequencing-grade trypsin (Promega) overnight at 37°C. Quantitative proteomics analysis was performed using isobaric tags for relative and absolute quantification (iTRAQ). For 25 µg of protein, 1 unit of iTRAQ labeling reagent (SCIEX) was used. The peptides from the control sample were labeled with iTRAQ reagent 115, and peptides from the treated sample were

labeled with iTRAQ reagent 117. Labeling reagent was reconstituted in ethanol such that each protein sample was labeled at a final concentration of 90% ethanol, and labeling was performed for 2 hours. After labeling was complete, labeled peptides were combined and fractionation was performed using the Thermo Scientific Pierce High pH Reversed-Phase Peptide Fractionation Kit (Product No. 84868) similar to the manufacturer's recommended protocol for TMT-labeled peptides. Elution steps consisted of the following: 7.5% 10%, 12.5%, 15%, 17.5%, 20%, 22.5%, 25%, 30%, 35%, 50%, and 80% Acetonitrile with 0.1% Triethylamine. Eluted fractions were dried via vacuum centrifugation in a SpeedVac concentrator, and peptides were reconstituted in 0.1% formic acid for analysis by LC-coupled tandem mass spectrometry (LC-MS/MS). An analytical column was packed with 35cm of C18 reverse phase material (Jupiter, 3µm beads, 300Å, Phenomenox) directly into a laser-pulled emitter tip. Peptides were loaded on the capillary reverse phase analytical column (360µm O.D. x 100µm I.D.) using a Dionex Ultimate 3000 nanoLC and autosampler. The mobile phase solvents consisted of 0.1% formic acid, 99.9% water (solvent A) and 0.1% formic acid, 99.9% acetonitrile (solvent B). For the peptide fractions eluted from the high pH reverse phase column with 7.5% - 25% acetonitrile, peptides were analyzed via LC-MS/MS at a flow rate of 400 nL/min, using a 180-minute gradient. The gradient consisted of the following: 5-30%B in 140 min, 30-50%B in 10 min, 50-70%B in 5 min, 70%B in 5 min; 70-5%B in 4 min, followed by column equilibration for the next sample. A Q Exactive Plus mass spectrometer (Thermo Scientific), equipped with a nanoelectrospray ionization source, was used to mass analyze the eluting peptides using a data-dependent method. The instrument method consisted of MS1 using an MS AGC target value of 3e6, followed by up to 15 MS/MS scans of the most abundant ions detected in the preceding MS scan with an MS2 AGC target of 1e5. Dynamic exclusion was set to 20s, HCD collision energy was set to 30 nce, and peptide match

and isotope exclusion were enabled. For the high pH column fraction eluted with 30% acetonitrile, the peptides were analyzed by LC-MS/MS using a gradient of 5-30%B in 85 min, 30-50%B in 10 min, 50-70%B in 5 min, 70%B for 5 min, 70-5%B in 4 min, followed by column re-equilibration. For the remaining fractions, the peptides were combined eluted from the reverse phase analytical column using a gradient of 5-50%B in 70 min, 50-98%B in 35 min, 98%B for 2 min, 98-5%B in 2 min.

Protein identification and quantitative analysis

Peptide/protein identifications and quantitative analysis were performed using Spectrum Mill (Agilent) as previously described[345]. MS/MS spectra were searched against a subset of the UniProt KB protein database containing *Homo sapiens* protein sequences. Autovalidation procedures in Spectrum Mill were used to filter the data to <1% false discovery rates at the protein and peptide level. Quantified proteins were then filtered to include those proteins for which a minimum of two unique peptides were identified. Log_2 protein ratios were fit to a normal distribution using non-linear (least squares) regression. The calculated mean derived from the Gaussian fit was used to normalize individual log_2 ratios for each quantified protein. The normalized log_2 ratios were then also fit to a normal distribution, and the mean and standard deviation values derived from the Gaussian fit of the normalized ratios were used to calculate p values. Subsequently, p values were corrected for multiple comparisons by the Benjamini-Hochberg method[346]. Gene Ontology analysis was performed using WebGestalt.

Immunoblot analysis

Cells were washed with ice cold 1X PBS three times, collected by scrapping in ice cold 1X PBS, and then pelleted at 300*g* for 5 minutes at 4°C. The pellets were lysed with RIPA buffer (Millipore Sigma, Catalog #R0278) supplemented with Halt protease and phosphatase inhibitor cocktail (Thermofisher, Catalog #78440). Samples were incubated on ice for 5 minutes and then sonicated for 30 seconds on, 30 seconds off in the cold room for a total of three times. Samples were subsequently incubated on ice for 20 minutes before spinning at 20,000*g* at 4°C for 20 minutes. The supernatant was transferred to new microcentrifuge tubes. EVs were lysed with 1% SDS to isolate their protein. Protein concentration was quantified with a Pierce BCA assay (Thermofisher, Catalog #23227). 10-20 µg of protein was then run on a 4-20% SDS-PAGE Gel and transferred onto polyvinylidene difluoride (PVDF) membranes. The membranes were blocked for at least 30 minutes with 5% bovine serum albumin in TBST or 5% milk in TBST. The membranes were then probed overnight at 4°C with the following primary antibodies: Rabbit anti-GLUT1 (1:1000, Cell Signaling Technology, Catalog #12939), Rabbit anti-GM130 (1:1000, Cell Signaling Technology, Catalog #12480), Mouse anti-ALIX (1:1000, Cell Signaling Technology, Catalog #2171), Mouse anti-GAPDH (1:500, Santa Cruz Biotechnology, Catalog #365062), Rabbit anti-TSG101 (1:10,000, Abcam, Catalog #125011), Mouse anti-HSP70 (1:10,000, Santa Cruz Biotechnology, Catalog #32239), Mouse anti-Flotillin-1 (1:10,000, BD Biosciences, Catalog #610820). After three ten-minute washes with TBST, the membranes were probed with either goat anti-mouse IgG-HRP (Promega, Catalog #W4021) or goat anti-rabbit IgG-HRP (Promega, Catalog #W4011) for 30 minutes. After three ten-minute washes with TBST, the membranes were incubated for 5 minutes with SuperSignal West Pico Plus Chemiluminescent Substrate (Thermofisher, Catalog #34577) or SuperSignal West Femto

Maximum Sensitivity Substrate (Thermofisher, Catalog #34096) and imaged with the ChemiDoc MP Imaging System (BioRad, Catalog #12003154). Images were analyzed with Image Lab software (BioRad).

Metabolic studies of EVs

EVs were immediately used after isolation for metabolic assays. For the bioluminescent glucose uptake assay (Promega, Catalog #J1341), an equal number of vesicles for each condition were plated in 96-well opaque plates. 1 mM of 2-deoxyglucose was added to each well for 60 minutes at room temperature. The reaction was stopped with the provided Stop and Neutralization buffers, and the 2DG6P detection reagent (consisting of glucose-6-phosphate dehydrogenase, NADP+, luciferase, reductase, prolucferin, and luciferase) was added for 30 minutes[347]. For the GAPDH activity assay (Millipore Sigma, Catalog #MAK277), equal number of vesicles were homogenized in the kit's GAPDH assay buffer on ice for 10 minutes. The samples were then spun at 10,000*g* for 5 minutes at 4°C, and the supernatant was plated into 96-well plates. The provided GAPDH developer and substrate reagents were then added to the well and incubated for 10-30 minutes. For the ATP measurement assay (Millipore, Catalog #MAK135), an equal number of vesicles per condition was incubated in 5 mM of glucose for 10 minutes at 37°C, and then ATP was measured according to the manufacturer's protocol. For the lactate measurement assay (Promega, Catalog #J5021), equal number of vesicles were incubated in 5 mM glucose for 48 hours at 37°C, and then lactate was measured according to the manufacturer's protocol. Luminescence (Glucose uptake, ATP, and lactate assays) and 450nm absorbance (GAPDH activity assay) values were measured using a Promega GloMax Plate Reader. Luminescence values were normalized to the DMSO or empty vector sEVs conditions.

GAPDH activity was calculated using the following formula: B / (T*V), where B represents the amount of NADH generated, T represents the time of the reaction, and V represents the sample volume. GAPDH activity was then normalized to the DMSO or empty vector sEVs conditions.

Cell-titer glo viability assay

6000 cells were seeded in 96-well dishes. The next day, the cells were washed three times with PBS and incubated with Opti-MEM + VEGFR TKIs at different concentrations. Forty-eight hours later, the Cell-Titer Glo viability assay was performed according to manufacturer's protocol. Luminescence values were measured using a Promega GloMax Plate Reader.

UALCAN portal analysis of the cancer genome atlas and clinical proteomic tumor Analysis consortium datasets

TCGA and CPTAC datasets was analyzed on UALCAN (http://ualcan.path.uab.edu) as previously described[348,349]. SLC2A1 (GLUT1) mRNA expression, proteomic expression profile, and survival correlation were analyzed in clear cell renal cell carcinoma.

GLUT1 expression analysis in Pazopanib-treated RCC tumors

GLUT1 transcriptomic data from RCC patients receiving Pazopanib therapy prior to nephrectomy were obtained from a phase II study (NCT01361113) as described in Wood *et al*[350]. Upper quartile normalized gene counts were log2 transformed, and GLUT1 expression in pre-treatment and post-treatment tumors was normalized to the mean GLUT1 expression in normal kidney tissue. Full expression data is located in a MINSEQE-compliant public database (dbGap;

accession hon. phs002053.v1.p1; https://www.ncbi.nlm.nih.gov/projects/gap/cgi-bin/study.cgi?study_id=phs002053.v1.p1).

Statistical analysis

All graphs and statistical tests were made in GraphPad Prism 8. Sample sizes were determined by previous experiments and sufficient for determination of statistical significance between groups. Cells were randomly assigned to experimental groups. Data were excluded only for systematic quality control purposes, such as if cells were ill-appearing or dead. Statistical significance between two groups was calculated using a two-sided unpaired Student's t-test. Multiple groups were compared with a one-way ANOVA with Tukey post hoc test. The Shapiro-Wilk test was used to test for normality. The P value for the Kaplan-Meier survival plot was calculated with log-rank test[348]. P values less than 0.05 were considered significant. A simple linear regression was performed for the sEV dose curve in the glucose uptake assay, and r^2 was calculated to measure the goodness-of-fit of the best-fit line. The sample size (n) for each experimental condition is plotted as individual data points in bar graphs as described in each figure legend. Bars represent the mean, and error bars represent the SEM. The minimum, first quartile, median, third quartile, and maximum are showed in boxplots. Experiments were performed three times unless otherwise stated in the figure legend.

Results

Sunitinib and Axitinib increase secretion of EVs from human RCC cells

We first characterized the EVs secreted from 786-0 human RCC cells in accordance with established guidelines[351]. Vesicles were isolated from the cell culture media with differential ultracentrifugation—the lEVs were obtained from the 10,000*g* pellet, whereas the sEVs were obtained from the 100,000*g* pellet followed by density gradient centrifugation for further purification according to previously established protocols[286]. Western blot analysis revealed that fractions 6 and 7 of the density gradient contained sEV markers such as Heat Shock Protein 70 (HSP70), Tumor Susceptibility Gene 101 (TSG101), and Flotillin-1, and lacked the negative marker GM130 [Figure 18A], confirming these fractions were enriched with sEVs. In addition, nanoparticle tracking analysis of the fractions 6 and 7 vesicles showed they had a peak diameter of 129nm, which is within a distribution typical of sEVs [Figure 18B]. Finally, transmission electron microscopy revealed small, round structures with a cup-shaped morphology [Figure 18C]. Henceforth, the term "sEV" will be used to refer to vesicles purified from fractions 6 and 7 of the density gradient.

Although TKIs have played a significant role in treating RCC for over a decade, their tumor cell-intrinsic effects have been challenging to establish. Given that hypoxia signaling has been shown to increase EV secretion from cancer[341–344], we hypothesized that these pharmaceutical agents, which influence the activity of multiple hypoxia targets, could affect the secretion of tumor-derived EVs. To test this hypothesis, we treated 786-0 cells with Sunitinib or Axitinib. Neither inhibitor significantly changed 786-0 cell viability using concentrations up to 10 μM [Figure 19A-B]. However, 786-0 cells treated with either Sunitinib or Axitinib exhibited a dose-dependent increase in their lEV and sEV secretion on a per cell basis compared to their DMSO-treated counterparts [Figure 20A-B, D-E]. Nanoparticle tracking analysis showed that

neither of these inhibitors altered the size distribution of the 786-0 EVs [Figure 20C, F]. We selected 5 μM of TKI as our standard dose based on previous work[352]. Transmission electron microscopy revealed that the sEVs from Sunitinib-treated cells were similar in morphology to sEVs from vehicle-treated cells [Figure 20G-H]. To validate these findings, we tested a second RCC cell line, A498, and observed that Sunitinib and Axitinib treatment also led to an increase in EV secretion from these cells without affecting cell viability or the size distribution of their vesicles [Figure 21A-H]. Collectively, these studies reveal that Sunitinib and Axitinib augment vesicle secretion from human RCC cells *in vitro*.

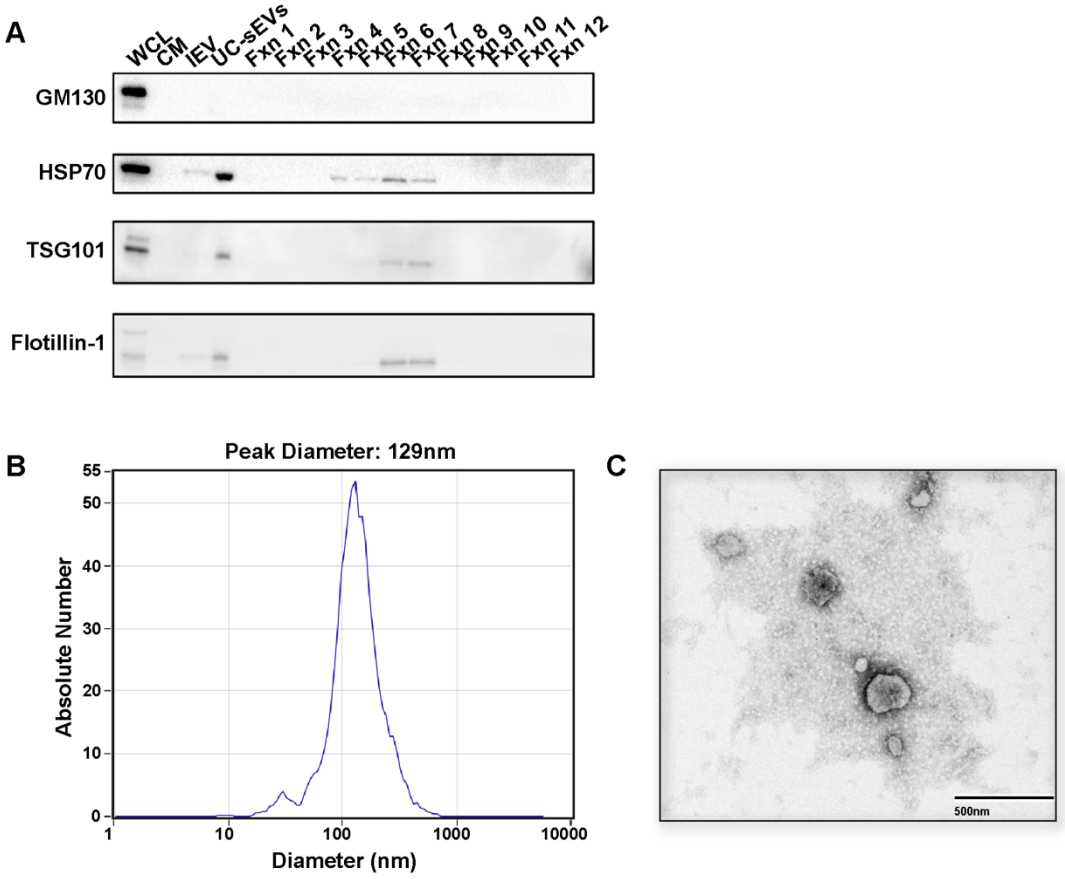

Figure 18. Characterization of extracellular vesicles from 786-0 human renal cell carcinoma cells

A. Representative immunoblots of the whole cell lysate (WCL), conditioned media (CM), large EV (lEV), ultracentrifuged sEV (UC-sEV), and the twelve fractions (fxn) of density gradient sEVs isolated from 786-0 cells from two independent experiments (n = 2). B. Representative nanoparticle tracking analysis showing the size distribution of particles isolated from density gradient fractions 6 and 7 from 786-0 cells from three independent experiments (n = 3). Peak diameter is 129nm (typical size of sEVs is 30-150 nm). C. A negative stained transmission electron microscopy image of 786-0 sEVs from one independent experiment (n = 1).

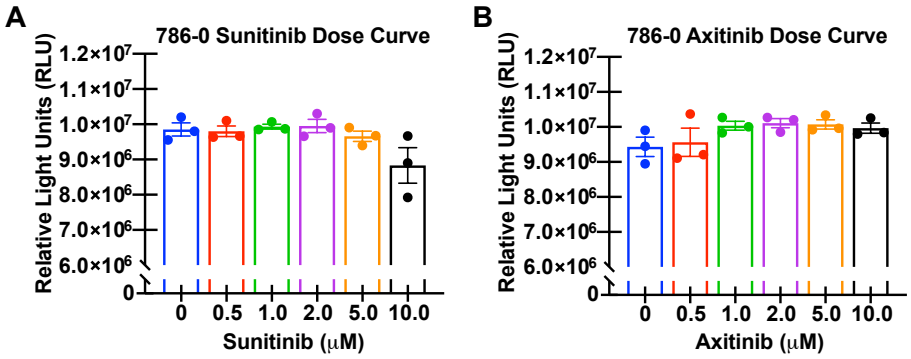

Figure 19. Sunitinib and Axitinib do not affect 786-0 cell viability

A-B. CellTiter-Glo viability assay of 786-0 cells treated with 0-10 μM of (A) Sunitinib or (B) Axitinib. The differences in cell viability were not statistically significant by one-way ANOVA. Results are from 3 independent experiments (n = 3). Data points represent values from independent experiments. Bars represent the mean of the plotted data points, and error bars represent the standard error of the mean (SEM).

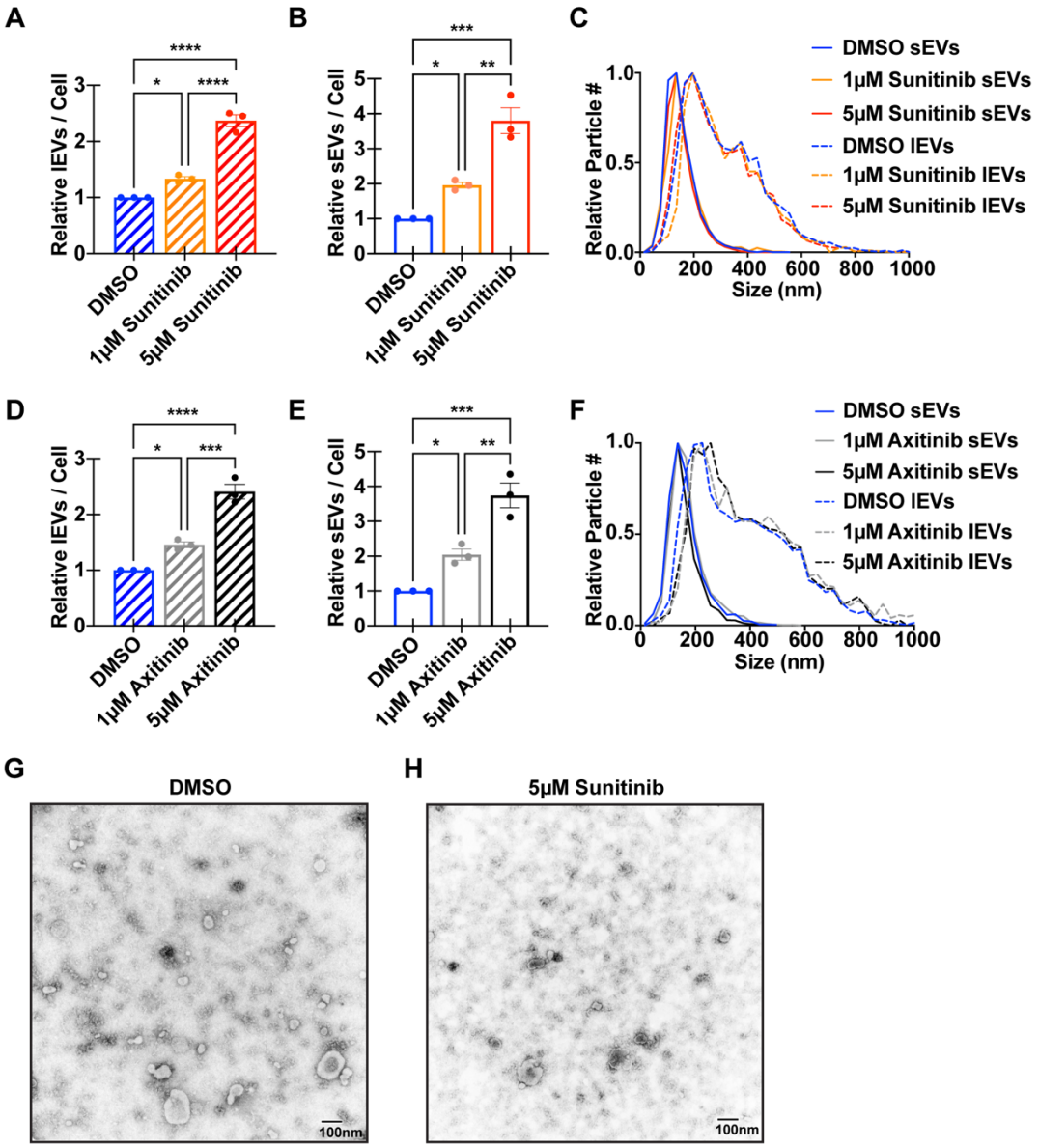

Figure 20. Tyrosine kinase inhibitors Sunitinib and Axitinib augment EV secretion

A-B. Relative secretion of (A) large extracellular vesicles (lEVs) or (B) small extracellular vesicles (sEVs) per 786-0 cell after treatment with DMSO, 1 μM Sunitinib, or 5 μM Sunitinib. Results are from 3 independent experiments (n = 3). C. Average nanoparticle tracking analysis traces from 3 independent experiments (n = 3) showing the size distribution of lEVs (dotted lines) and sEVs (solid lines) isolated from 786-0 cells treated with DMSO, 1 μM Sunitinib, or 5

μM Sunitinib. D-E. Relative secretion of (D) lEVs or (E) sEVs per 786-0 cell after treatment with DMSO, 1 μM Axitinib, or 5 μM Axitinib. Results are from 3 independent experiments (n = 3). F. Average nanoparticle tracking analysis traces from 3 independent experiments (n = 3) showing the size distribution of lEVs (dotted lines) and sEVs (solid lines) isolated from 786-0 cells treated with DMSO, 1 μM Axitinib, or 5 μM Axitinib. G-H. Representative transmission electron microscopy images of sEVs isolated from 786-0 cells treated with (G) DMSO or (H) 5 μM Sunitinib from one independent experiment (n = 1). Bars represent the mean of the plotted data points (n = 3). Error bars are standard error of the mean (SEM). P values were calculated using a two-sided unpaired Student's t-test for the other panels. * $p < 0.05$, ** $p < 0.01$, *** $p < 0.001$, **** $p < 0.0001$.

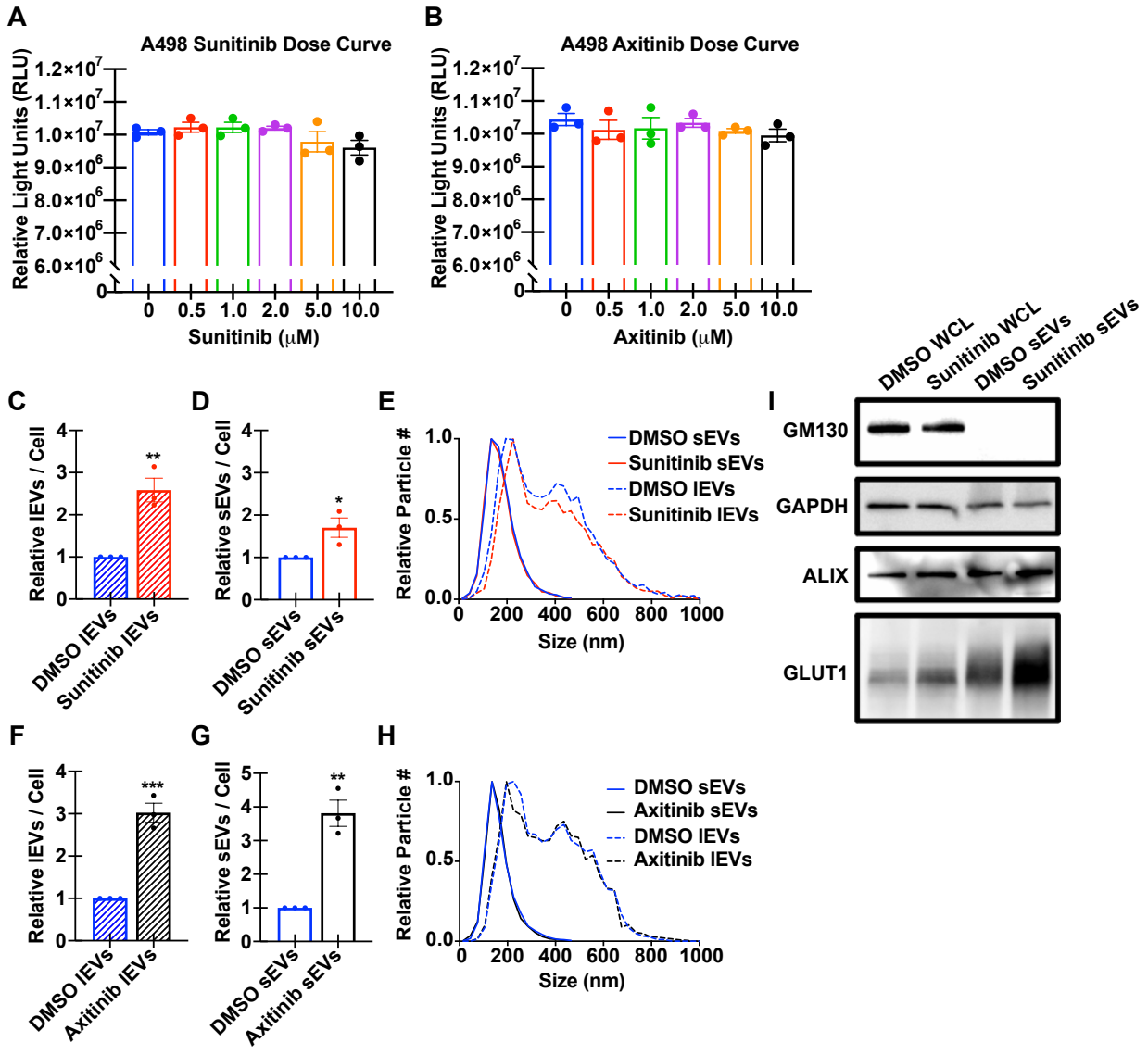

Figure 21. Tyrosine kinase inhibitors increase GLUT1$^+$ EV secretion from A498 cells

A-B. CellTiter-Glo viability assay of A498 cells treated with 0-10 μM of (A) Sunitinib or (B) Axitinib. The differences in cell viability were not statistically significant. Results are from 3 independent experiments (n = 3). C-D. Relative secretion of (C) large extracellular vesicles (lEVs) or (D) small extracellular vesicles (sEVs) per A498 cell after treatment with DMSO or 5 μM Sunitinib from three independent experiments (n = 3). E. Average nanoparticle tracking analysis traces from 3 independent experiments (n = 3) showing the size distribution of lEVs

(dotted lines) and sEVs (solid lines) isolated from A498 cells treated with DMSO or 5 μM Sunitinib. F-G. Relative secretion of (F) lEVs or (G) sEVs per A498 cell after treatment with DMSO or 5 μM Axitinib from three independent experiments (n = 3). H. Average nanoparticle tracking analysis traces from 3 independent experiments (n = 3) showing the size distribution of lEVs (dotted lines) and sEVs (solid lines) isolated from A498 cells treated with DMSO or 5 μM Axitinib. I. Western blot analysis of whole cell lysates (WCLs) and sEVs secreted from A498 cells treated with DMSO or 5 μM Sunitinib from one independent experiment (n = 1). Data points represent values from independent experiments. Bars represent the mean of the plotted data points, and error bars represent the standard error of the mean (SEM). P values were calculated using a one-way ANOVA for A-B or a two-sided unpaired Student's t-test for the other panels. * $p < 0.05$, ** $p < 0.01$, *** $p < 0.001$.

Sunitinib-treated 786-0 cells packaged more GLUT1 into sEVs

Sunitinib treatment has previously been shown to alter protein expression in RCC tumors[353] as well as the RNA content of EVs released from these cells[318]. We next sought to determine whether the protein cargo of RCC EVs changes upon Sunitinib treatment. Since the yield of lEVs was considerably lower than the yield of sEVs, we decided to focus the rest of our studies on sEVs. Using isobaric tags for relative and absolute quantification (iTRAQ)-liquid chromatography tandem mass spectrometry, we analyzed differences in protein cargo of sEVs secreted from vehicle- and Sunitinib-treated 786-0 cells [Figure 22A]. A total of 337 proteins with greater than a 1.5-fold increase were identified in the Sunitinib sEVs. Gene ontology analysis revealed over half of these proteins were involved with metabolic processes [Figure 22B]. Interestingly, glucose transporters, such as GLUT1, were among the top proteins enriched in sEVs purified from Sunitinib-treated cells [Figure 22A]. To validate this finding, we ran a western blot with whole cell lysates and sEVs from 786-0 cells treated with DMSO or Sunitinib. While there was an increase in cellular GLUT1 protein levels upon treatment with Sunitinib, the increase of GLUT1 in Sunitinib sEVs was striking [Figure 22C]. We also observed a similar increase in GLUT1 levels in A498 cells and in their sEVs after treatment with Sunitinib [Figure 21I]. These data reveal that Sunitinib alters the protein composition of human RCC sEVs, especially those involved in metabolism.

A

iTRAQ Proteomics: 786-0 Sunitinib vs. DMSO sEVs

Protein	Fold Change
Glucose transporter member 3 (GLUT3)	2.68
Thymosin beta-10	2.58
Rho GTPase-activating protein 23	2.53
Transmembrane protein 163	2.53
LDL receptor-related protein 10	2.43
GABA receptor-associated protein-like 2	2.39
Sodium-coupled neutral amino acid transporter 1	2.34
Scavenger receptor class B member 1	2.32
Trans-Golgi network integral membrane protein 2	2.28
Serine incorporator 3	2.26
Protein TFG	2.20
Glucose transporter member 1 (GLUT1)	2.17
Tubulin-specific chaperone A	2.13
Transmembrane prostate androgen-induced protein	2.12
Vesicle-associated membrane protein 8	2.11

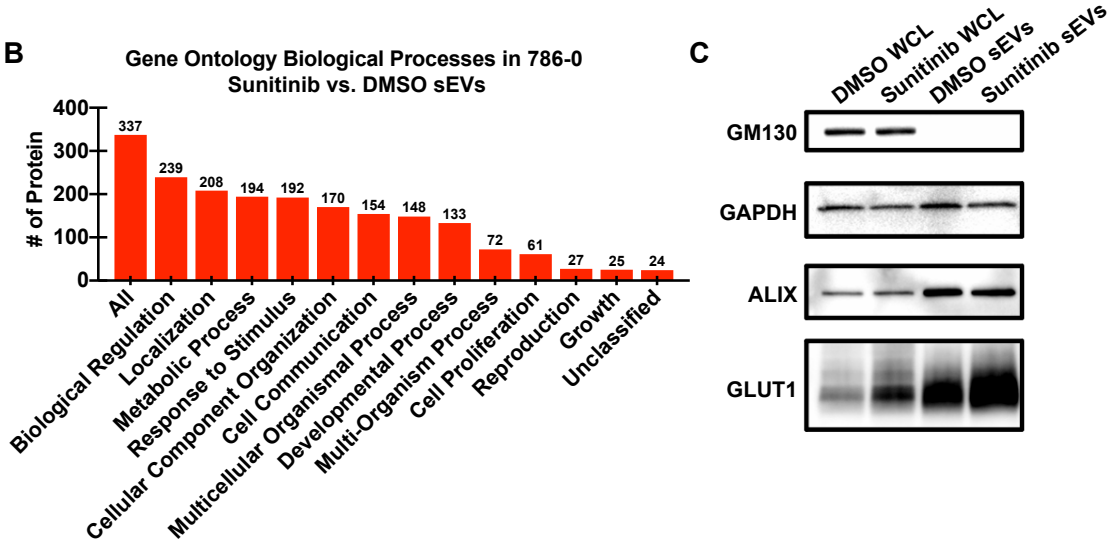

Figure 22. Sunitinib increases GLUT1 packaging into RCC sEVs

A. The top 15 proteins enriched in Sunitinib sEVs and their fold change values in the iTRAQ proteomics analysis are listed. Results are from one independent experiment (n = 1). B. Biological processes identified in a gene ontology analysis of proteins with greater than 1.5-fold change in Sunitinib vs. DMSO sEVs. Results are from one independent experiment (n = 1). C.

Representative immunoblots of whole cell lysates (WCLs) and sEVs secreted from 786-0 cells treated with DMSO or 5 μM Sunitinib from two independent experiments (n = 2).

GLUT1 expression correlates with poor survival and increases after TKI treatment in RCC patients

The increase in GLUT1 cellular and sEV protein levels after TKI treatment led us to examine GLUT1 expression in patient tumors. RCC undergoes metabolic reprogramming with a high dependence on GLUT1 for glycolysis and ATP production[96,335]. Using TCGA data, we observed that RCC tumors have higher mRNA transcript levels of GLUT1, which translates into higher GLUT1 protein levels than in normal tissue [Figure 23A-B]. In addition, higher GLUT1 expression correlated with worse survival in RCC patients [Figure 23C]. We also analyzed GLUT1 expression data from RCC patients enrolled in a multi-institution, single-arm phase II study who received Pazopanib, a multi-targeted TKI, prior to planned nephrectomy[350]. In concordance with TCGA data, the pre- and post-treatment tumors exhibited higher GLUT1 expression compared to normal kidney tissue [Figure 23D]. Post-treatment specimens also demonstrated an increase in GLUT1 expression compared to their pre-treatment counterparts, although the difference was not statistically significant ($p = 0.14$) [Figure 23D]. These data indicate RCC tumors express higher levels of GLUT1, which portends a poor prognosis in these patients, and point toward further increased GLUT1 expression following systemic exposure to an anti-angiogenic TKI.

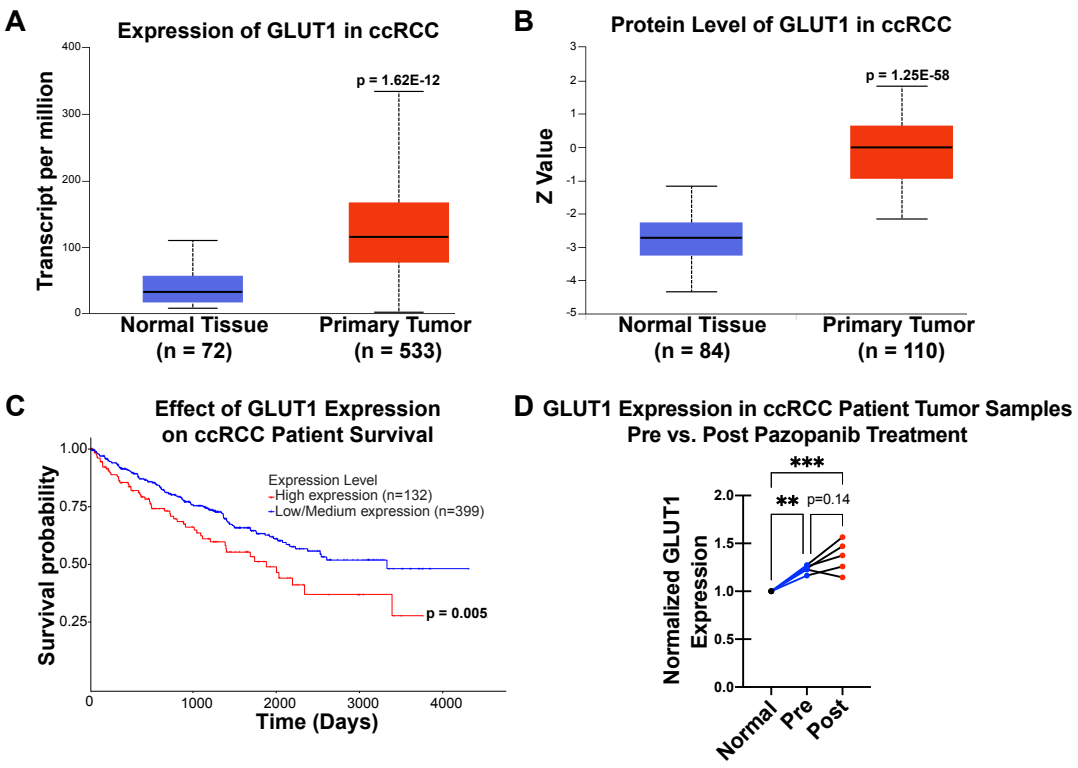

Figure 23. GLUT1 expression is higher and correlates with poor patient survival in RCC

A. TCGA analysis from UALCAN of GLUT1 transcript levels in clear cell renal cell carcinoma (ccRCC) vs. normal tissue. Significance of difference was calculated by a two-sided unpaired t-test considering unequal variance. B. CPTAC analysis from UALCAN of GLUT1 protein levels in ccRCC vs. normal tissue. Z-values represent standard deviations from the median across samples. Significance of difference was calculated by a two-sided unpaired t-test considering unequal variance. C. Analysis of ccRCC patient survival from UALCAN based on high (red) or low (blue) GLUT1 expression. High expression patients show expression value greater than the third quartile. Significance of survival impact was measured by a log-rank test. D. GLUT1 expression in five pre- and post-Pazopanib treated RCC tumors normalized to normal kidney tissue. Significance was calculated with a one-way ANOVA with Tukey post hoc test. ** $p < 0.01$, *** $p < 0.001$.

sEVs from TKI-treated RCC cells take up more glucose and have increased glycolytic activity

Given that GLUT1 expression increases in RCC tumors after TKI treatment and was enriched in Sunitinib sEVs, we hypothesized that these vesicles would, themselves, take up glucose, and do so proportionally to the level of GLUT1 present in the sEVs. To test this hypothesis, we used a bioluminescent assay to measure uptake of the glucose analog 2-deoxyglucose (2-DG)[347]. We found that RCC vesicles take up 2-DG in a dose-dependent manner [Figure 24A]. Further, treating 786-0 cells with either Sunitinib or Axitinib led to the secretion of sEVs that took up two-fold more 2-DG than sEVs from vehicle-treated cells [Figure 24B-C]. These results indicate that RCC sEVs actively take up glucose from their environment, and TKI-treatment of the parental cells can enhance sEV glucose uptake capacity commensurately with an increase in their glucose transporter levels.

To determine whether these vesicles utilize glucose in downstream glycolytic reactions, we applied a colorimetric-based GAPDH activity assay and found that sEVs released from Sunitinib- and Axitinib-treated 786-0 cells also displayed higher GAPDH activity [Figure 24D-E]. In addition, upon addition of 5 mM glucose, the sEVs from Axitinib- and Sunitinib-treated cells produced more ATP and secreted more lactate than those from vehicle-treated cells [Figure 24F-I]. The increases in glucose uptake, GAPDH activity, ATP content, and lactate production were also observed in sEVs secreted from A498 cells treated with Sunitinib [Figure 25A-D]. Together, these results suggest that TKIs increase the glucose uptake into RCC sEVs, and glucose can subsequently undergo glycolytic reactions in sEVs to produce the end products ATP and lactate.

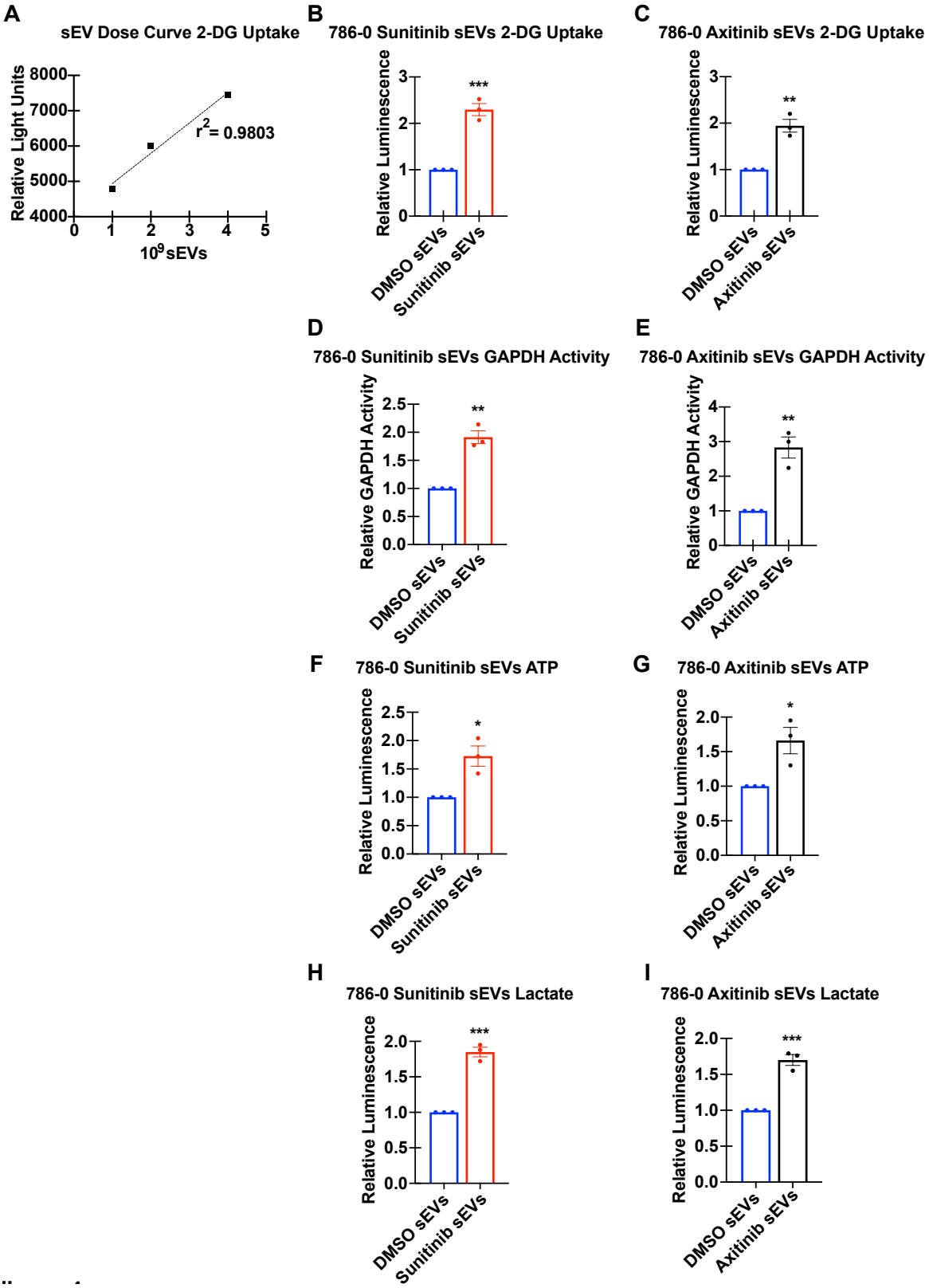
A
sEV Dose Curve 2-DG Uptake
Relative Light Units
8000
7000
6000
5000
4000
0
1
2
3
4
5
10^9sEVs
r^2= 0.9803
B
786-0 Sunitinib sEVs 2-DG Uptake
Relative Luminescence
***
DMSO sEVs
Sunitinib sEVs
C
786-0 Axitinib sEVs 2-DG Uptake
Relative Luminescence
**
DMSO sEVs
Axitinib sEVs
D
786-0 Sunitinib sEVs GAPDH Activity
Relative GAPDH Activity
**
DMSO sEVs
Sunitinib sEVs
E
786-0 Axitinib sEVs GAPDH Activity
Relative GAPDH Activity
**
DMSO sEVs
Axitinib sEVs
F
786-0 Sunitinib sEVs ATP
Relative Luminescence
*
DMSO sEVs
Sunitinib sEVs
G
786-0 Axitinib sEVs ATP
Relative Luminescence
*
DMSO sEVs
Axitinib sEVs
H
786-0 Sunitinib sEVs Lactate
Relative Luminescence
***
DMSO sEVs
Sunitinib sEVs
I
786-0 Axitinib sEVs Lactate
Relative Luminescence
***
DMSO sEVs
Axitinib sEVs

Figure 24. sEVs secreted from tyrosine kinase inhibitor-treated cells have increased glucose uptake and glycolytic activity

A. Relative light units measured in a 2-deoxyglucose (2-DG) bioluminescent uptake assay (n = 1) for an increasing number of 786-0 sEVs. The best-fit line is graphed. A simple linear regression was performed, and r^2 was calculated to measure the goodness-of-fit of the best-fit line. B. Relative 2-DG uptake of 786-0 DMSO vs. Sunitinib sEVs from 3 independent experiments (n = 3). C. Relative 2-DG uptake of 786-0 DMSO vs. Axitinib sEVs from 3 independent experiments (n = 3). D. Relative GAPDH Activity of 786-0 DMSO vs. Sunitinib sEVs from 3 independent experiments (n = 3). E. Relative GAPDH Activity of 786-0 DMSO vs. Axitinib sEVs from 3 independent experiments (n = 3). F. Relative ATP produced by 786-0 DMSO vs. Sunitinib sEVs after addition of 5 mM glucose for ten minutes from 3 independent experiments (n = 3). G. Relative ATP produced by 786-0 DMSO vs. Axitinib sEVs after addition of 5 mM glucose for ten minutes from 3 independent experiments (n = 3). H. Relative lactate secretion of 786-0 DMSO vs. Sunitinib sEVs after addition of 5 mM glucose for 48 hours from 3 independent experiments (n = 3). I. Relative lactate secretion of 786-0 DMSO vs. Axitinib sEVs after addition of 5 mM glucose for 48 hours from 3 independent experiments (n = 3). Data points represent values from independent experiments. Bars represent the mean of the plotted data points, and error bars represent the standard error of the mean (SEM). P values were calculated using a two-sided unpaired Student's t-test. * $p < 0.05$, ** $p < 0.01$, *** $p < 0.001$.

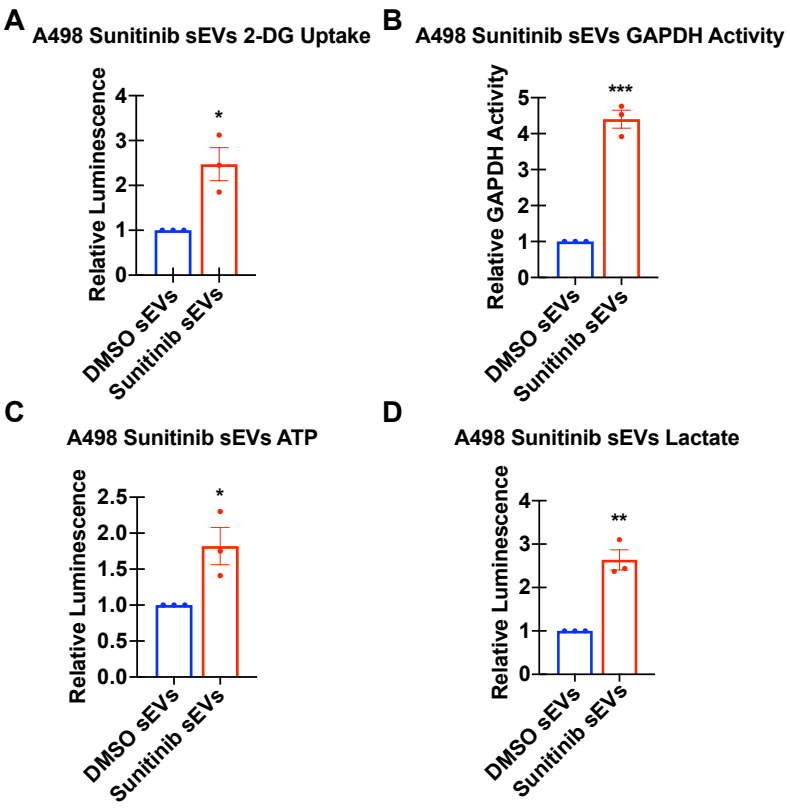

Figure 25. Sunitinib increases glucose uptake and glycolytic activity of A498 sEVs

A. Relative 2-DG uptake of A498 DMSO vs. Sunitinib sEVs from three independent experiments (n = 3). B. Relative GAPDH Activity of A498 DMSO vs. Sunitinib sEVs from three independent experiments (n = 3). C. Relative ATP produced by A498 DMSO vs. Sunitinib sEVs after addition of 5 mM glucose for ten minutes from three independent experiments (n = 3). D. Relative lactate secretion of A498 DMSO vs. Sunitinib sEVs after addition of 5 mM glucose for 48 hours from three independent experiments (n = 3). Data points represent values from independent experiments. Bars represent the mean of the plotted data points, and error bars represent the standard error of the mean (SEM). P values were calculated using a two-sided unpaired Student's t-test. * $p < 0.05$, ** $p < 0.01$, *** $p < 0.001$.

sEVs with more GLUT1 have increased glycolytic activity

To investigate whether higher GLUT1 expression in RCC cells leads to changes in the metabolic activity of sEVs, we overexpressed GLUT1 in 786-0 cells and isolated sEVs from the culture media. By Western blot analysis, we found that the increase in GLUT1 levels in the cells led to more GLUT1 packaging into sEVs [Figure 26A]. There was no significant change in the number of sEVs secreted per cell upon overexpression of GLUT1 [Figure 26B]. To determine whether sEVs containing higher levels of GLUT1 show increased glucose uptake and metabolic activity, we performed the same metabolic assays as we did for the TKI-treated vesicles. We found that the sEVs from the GLUT1 overexpressing (OE) cells indeed exhibited higher 2-DG uptake and increased GAPDH activity [Figure 26C-D]. The GLUT1 OE sEVs also produced more ATP and secreted more lactate upon addition of 5 mM glucose [Figure 26E-F]. Thus, RCC cells with higher GLUT1 expression secrete more GLUT1 into their sEVs, which is sufficient to augment glucose uptake and metabolism in sEVs.

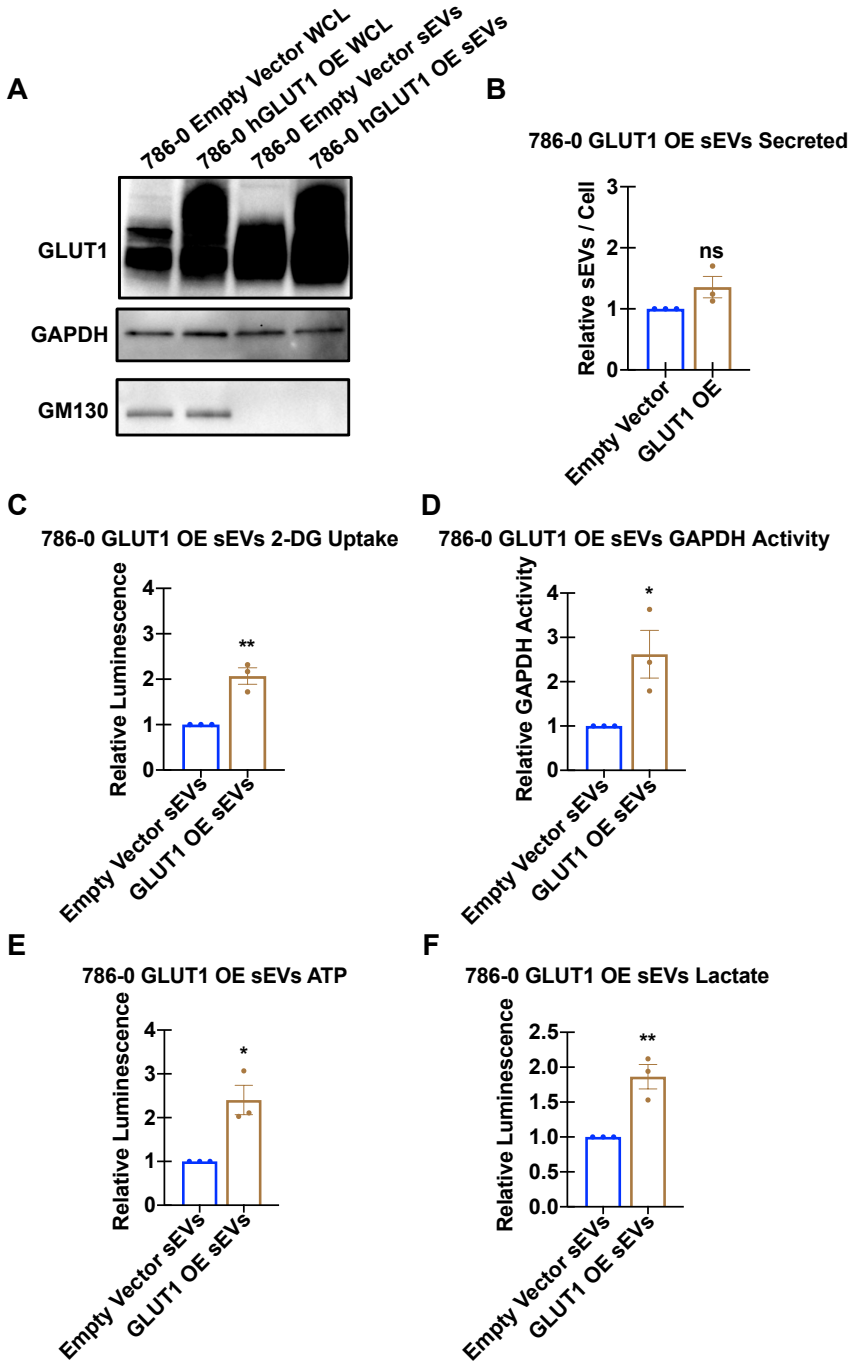

Figure 26. sEVs from cells overexpressing GLUT1 have increased glycolytic activity

A. Immunoblots of 786-0 whole cell lysates (WCL) infected with empty vector or GLUT1 overexpression (OE) lentiviral constructs and their secreted sEVs from one independent experiment (n = 1). B. Relative number of sEVs secreted per cell from 786-0 empty vector and

786-0 GLUT1 OE cells from 3 independent experiments (n = 3). Difference was not significant by a two-sided unpaired Student's t-test. C. Relative 2-DG uptake of 786-0 empty vector vs. GLUT1 OE sEVs from 3 independent experiments (n = 3). D. Relative GAPDH activity of 786-0 empty vector vs. GLUT1 OE sEVs from 3 independent experiments (n = 3). E. Relative ATP produced by 786-0 empty vector vs. GLUT1 OE sEVs after addition of 5 mM glucose for 10 minutes from 3 independent experiments (n = 3). F. Relative lactate secretion of 786-0 empty vector vs. GLUT1 OE sEVs after addition of 5 mM glucose for 48 hours from 3 independent experiments (n = 3). Data points represent values from independent experiments. Bars represent the mean of the plotted data points, and error bars represent the standard error of the mean (SEM). P values were calculated using a two-sided unpaired Student's t-test. ns = not significant, * $p < 0.05$, ** $p < 0.01$.

Discussion

VHL loss is an early genetic event characteristic of ccRCC, leading to a "pseudohypoxic" state with constitutive HIF signaling[14]. Previous data indicate that hypoxia can drive EV secretion from cancer cells[341–344]. We report here for the first time that the TKIs Sunitinib and Axitinib can also augment EV secretion from tumor cells with known *VHL* loss. Loss of *VHL* leads to the accumulation of HIF-1α and HIF-2α, both of which upregulate GLUT1 expression[24,354]. Our results support previous data demonstrating that GLUT1 can be packaged and enriched in EVs in response to different conditions[203,315]. In fact, protein databases show that some of the most commonly identified cargo in EVs include proteins involved in glycolysis[355].

Although EVs were first thought to carry junk protein, our study supports previous evidence showing EVs are metabolically active. For example, EVs containing adenylate cyclase synthesize cyclic AMP to direct the migration of *Dictyostelium discoideum*[356]. Prostate cancer EVs also contain glycolytic enzymes that can carry out glycolytic functions[315]. In addition, GLUT1-containing EVs secreted from hepatic stellate cells can induce glycolysis in recipient cells[202]. Similarly, glioma cells that take up exosomes from glioma stem cells exhibit increased glycolytic activity *in vitro*[357]. Our findings supplement these data, adding that Sunitinib and Axitinib can impact the metabolic cargo and glycolytic metabolism of EVs in RCC.

This study introduces several new questions for the field to tackle. First, although there was an increase in cellular GLUT1 protein levels after TKI treatment of RCC tumor cells, the mechanism behind TKIs increasing GLUT1 packaging into EVs, and whether this effect also occurs *in vivo* or in other tumor types, is a topic for future investigation. Another unresolved question is the role of hypoxia and HIF signaling in EV secretion upon treatment with TKIs. It is

possible that these TKIs may also contribute to increased EV secretion by inducing hypoxia in the tumor microenvironment, though this would require an *in vivo* system to test. However, anti-angiogenic therapies have also been known to induce "vessel normalization" and thus paradoxically improve blood flow to the tumor[358]. Therefore, the pseudohypoxic state characteristic of ccRCC may be regulating EV secretion through HIF signaling. In ccRCC, it is thought that HIF-1α plays a tumor suppressor role[28] whereas HIF-2α is an oncoprotein[359]. In fact, 71% of metastatic cases of ccRCC exhibit loss of chromosomes 9q and 14q, on which the *HIF1a* gene resides[360], and loss of 14q was associated with decreased overall survival in ccRCC[361]. Previous studies have explored the roles of both HIF-1α and HIF-2α in regulating EV secretion and cargo under hypoxia. For example, in breast cancer, which is known to be driven by HIF-1α[362], knockdown of HIF-1α was found to decrease EV secretion under hypoxic conditions[343]. Furthermore, it was found that knockdown of either HIF isoform reduced secretion of certain microRNA into pancreatic cancer and head and neck cancer EVs[201,363]. Another report demonstrated that knockdown of either HIF-1α or HIF-2α reduced *RAB22A* expression, leading to decrease microvesicle secretion from hypoxic breast cancer cells[364]. In our study, the 786-0 and A498 cells both lack HIF-1α expression, suggesting the possibility that HIF-2α may be driving the increased EV secretion upon TKI treatment. However, there are likely other factors mediating EV release after TKI treatment, and additional studies are necessary to differentiate these mediators of EV secretion.

Whether these vesicles from TKI-treated cells alter the metabolic phenotype of selected cells in the tumor microenvironment *in vivo* was not investigated in our study and needs to be addressed in the future. A recent report showed that cardiomyocytes package mitochondria into lEVs called exophers that are subsequently released and cleared by macrophages[365]. Impaired

clearance of these exophers led to metabolic abnormalities and cardiac dysfunction[365]. In contrast to the RCC sEVs that were able to take up glucose and subsequently carry out downstream glycolytic metabolism in our studies, the cardiac-derived exophers were not observed to exhibit metabolic activity[365]. In another report, glutamine metabolism was altered in cells upon uptake of prostate cancer large oncosomes, which are large tumor-derived microvesicles, but not by their exosomes[317]. It would be prudent to investigate the metabolic effects of vesicle subtypes on the different populations of cells in the tumor microenvironment given the renewed interest in these interactions with the advent of immunotherapy in solid tumor oncology.

It is interesting to note that other glucose transporters were also identified in our iTRAQ proteomics study as highly enriched proteins in Sunitinib sEVs. Glut3 was highly enriched with a 2.68-fold increase in Sunitinib sEVs [Figure 22A], and likely further contributes to the metabolic activity of these vesicles. Although Glut3 was previously identified in prostate cancer EVs[315], only GLUT1, and not GLUT2, GLUT3, or GLUT4, could be detected in mutant KRAS exosomes in colorectal cancer[203]. Thus, which glucose transporter in EVs is the most important for their metabolic activity, or whether all types of glucose transporters play an equal role, remains unanswered. Besides glucose transporters, other metabolic regulators were identified in our iTRAQ proteomics, including sodium-coupled neutral amino acid transporter 1 (SNAT1), which was the 7th highest protein enriched in Sunitinib sEVs [Figure 22A]. We speculate that TKIs may affect vesicle uptake of metabolites other than glucose, with subsequent widespread and diverse impacts on their metabolism.

Finally, since RCC sEVs take up glucose in an autonomous manner, an intriguing possibility exists that these vesicles may be competing with cells for glucose and other metabolites in the tumor microenvironment. The observation of increased ATP production and

lactate secretion from TKI-treated sEVs indicate that cells are not the only sources of these important metabolites. Therefore, these sEVs may be altering the metabolic composition and metabolism of a variety of cell types in the RCC tumor microenvironment, such as tumor infiltrating lymphocytes that require glucose for activation[366]. This is a particularly important question to investigate because anti-angiogenic therapies are increasingly being combined with immunotherapy to treat RCC as well as other cancer types[129]. EVs may thus play an important role in response or resistance to this combination therapy in patients. Further research about the metabolic interface of EVs and cells is critical to understand how tumors adapt to these therapies.

In summary, we report that RCC cells treated with anti-angiogenic TKIs increase their secretion of EVs. In particular, sEVs released from these cells contain more GLUT1 transporters, which results in increased glucose uptake and glycolytic activity in the sEVs. Moreover, higher GLUT1 levels is sufficient to increase the glucose uptake and glycolytic activity of sEVs. Thus, our study reveals a novel effect of TKIs commonly used to treat RCC: they alter vesicle secretion and enhance the metabolic activity taking place in EVs [Figure 27]. Our findings provide the first evidence that TKIs can affect tumor cells in this way, and this metabolic enhancement to sEVs potentially confer metabolic alterations to regional cells.

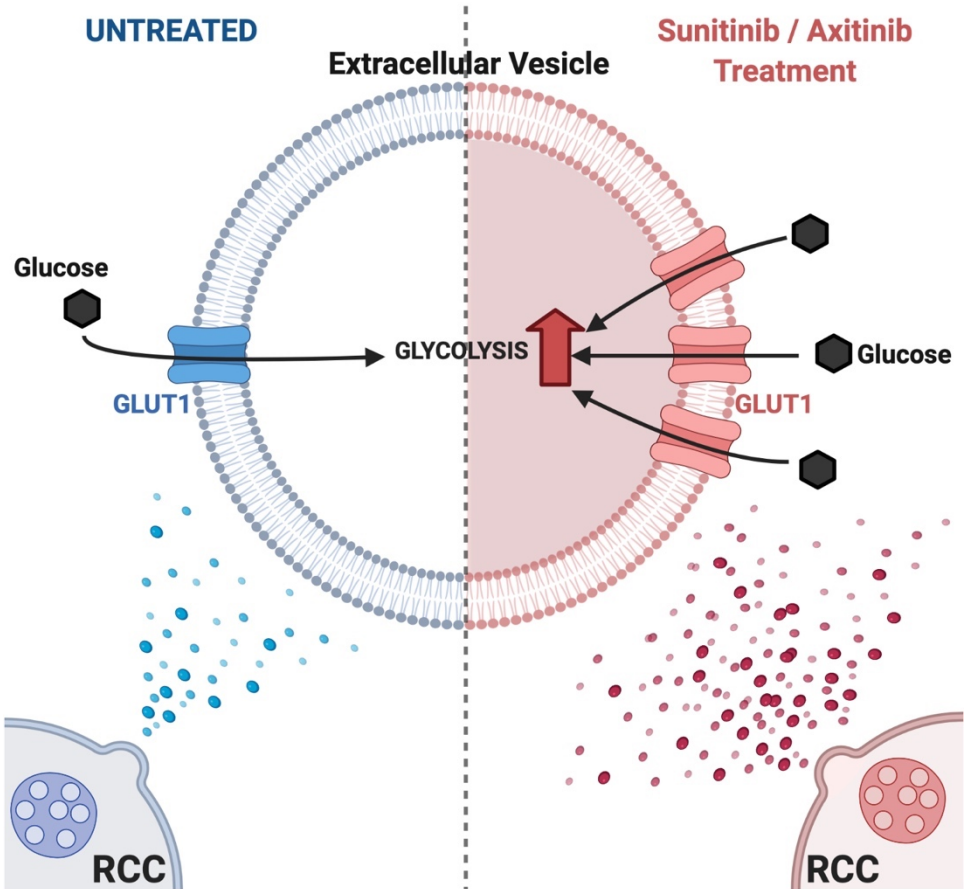

Figure 27. Proposed model of the effect of Sunitinib and Axitinib on extracellular vesicle secretion and metabolism

Upon treatment with Sunitinib or Axitinib, RCC cells secrete more extracellular vesicles that contain GLUT1, leading to increased glycolytic metabolism in their vesicles. Figure created with BioRender.com

CHAPTER VI

CONCLUSION, CLINICAL RELEVANCE, AND FUTURE DIRECTIONS

Conclusion and Clinical Relevance

Cancer remains the second leading cause of death in the United States, with over half a million deaths each year. Although data from the past two years demonstrate a decline in cancer deaths, most of the decrease in deaths is accounted for by lung, breast, and colon cancer, likely due to reductions in smoking, better detection, and more effective therapies[367]. Although this is significant progress, the incidence of other cancers such as kidney cancer continues to rise. Additionally, this progress is currently being severely threatened by the COVID-19 pandemic, which forced hundreds of laboratories and clinical trials to shut down or work at reduced capacities[368]. The direct impact of the pandemic on scientific progress are concerning and will likely persist for several years, and its adverse effects will not be fully appreciated for a long time.

However, there is hope on the horizon. With the rapid development of COVID-19 vaccines, laboratories are re-opening and getting back up to speed. Improvements in technologies, including faster and cheaper sequencing methods and integration of multi-omics data, will permit better understanding of the molecular underpinnings of cancer that can be leveraged for diagnostic and therapeutic benefit. Consequently, the rapid development of several new therapies over the past two decades have extended patient survival for numerous tumor

types including ccRCC, which has historically been refractory to traditional chemotherapies and radiation therapy.

In the early days of cancer research, the majority of studies focused on the characteristics of the tumor cells themselves. When it was discovered that cancer is a genetic disease, studying the DNA mutations and molecular signaling pathways that drive cancer growth became the cornerstone of cancer research. Groundbreaking research describing the effects of chromosome 3p loss, HIF signaling, and chromatin modifiers have significantly improved our understanding of ccRCC in the past few decades. More recently, there has been a greater appreciation that cancer is not one disease – it is a heterogenous disease. Many subclones can be found within a single patient tumor, and this has been delineated in numerous reports including the TRACERx studies in ccRCC. This insight into tumor heterogeneity gave birth to the field of precision medicine in oncology, where treatments can be tailored for individual cancer patients based on the genetic and molecular characteristics of their tumor. Chapter III explored a synthetic lethal interaction between *SETD2* loss and PI3Kβ inhibition, opening up the possibility of treating patients with *SETD2* mutations with targeted PI3Kβ and AKT inhibitors. Novel therapeutic targets and biomarkers to monitor patients' tumors are likely to emerge as more genomic studies of ccRCC are performed.

Importantly, cancer researchers and oncologists are increasingly recognizing the importance of the tumor microenvironment on tumorigenesis. Cancer growth can be influenced by the other cells in proximity to the tumor, including immune cells, fibroblasts, blood vessels, and others. In particular, significant headway has been made in the field of immuno-oncology. The advent of immune checkpoint blockade has revolutionized cancer treatment – cancers that were once thought to be incurable are now showing prolonged survival rates with

immunotherapy. In Chapter II, we reviewed important metabolic barriers to T cells and immunotherapy in the tumor microenvironment. These metabolic alterations are critical to consider as we utilize immunotherapies to treat more tumors types, and they are particularly important in ccRCC which harbors many metabolic alterations that were reviewed in Chapter I. We even found metabolic activity within the EVs they secrete, and their glycolytic activity increases upon TKI treatment as described in Chapter V. As discussed in Chapter IV, interest in these vesicles has exploded as an increasing number of reports have demonstrated their important contributions to tumorigenesis in the tumor microenvironment and even at distant sites. Fully elucidating how all of these complex components of tumor biology interact, from tumor heterogeneity to the tumor microenvironment to metabolism to EVs, will yield insights into the molecular make-up of cancer that will permit expansion of our therapeutic arsenal.

Future Directions

The important work described in this dissertation reveal new aspects of ccRCC that lay the foundation for future studies. They have opened up many questions for the field to address, some of which are discussed below.

What are the potential mechanisms of TKI-driven EV secretion?

Our results in Chapter V showing increased EV secretion from ccRCC cells treated with Sunitinib and Axitinib raise the question of which HIF isoform is more important in driving EV secretion. Hypoxia is known to promote the release of EVs in several tumor types[343,363]. However, the cell lines used in our study are HIF-1α deficient, suggesting that HIF-2α could be

driving EV secretion under TKI treatment in our model. Differentiating the role of HIF-1α vs. HIF-2α in TKI-induced EV secretion from ccRCC cells warrants further investigation.

However, it is also important to consider other regulators of EV secretion, which are discussed extensively in Chapter IV. For example, activation of the Ras/Raf/ERK pathway has been implicated in exosome biogenesis and secretion[369]. A previous study showed that 786-0 cells treated with Sunitinib undergo kinome reprogramming, including increased activation of multiple RTK pathways such as MAPK signaling[353]. We also observe an increase in phospho-ERK levels, but not Rab27a or Alix, after Sunitinib treatment by western blot [Figure 28]. Thus, MAPK signaling, as well as other signaling pathways, may be contributing to the increased EV secretion with anti-angiogenic TKI treatment.

Another regulator of exosome secretion is the ceramide pathway, as discussed in Chapter IV. Are anti-angiogenic TKIs increasing EV secretion from ccRCC cells via this other pathway? Does the ESCRT pathway or the ceramide pathway play a bigger role in exosome secretion from ccRCC tumors? It would be prudent to treat ccRCC cells with GW4869, a sphingomyelinase inhibitor known to suppress exosome secretion, in conjunction with Sunitinib or Axitinib to observe whether this compound abrogates the augmentation of EV secretion with TKIs. Defining the mechanisms of EV secretion will bring us closer to potentially targeting these EVs for future therapeutic applications.

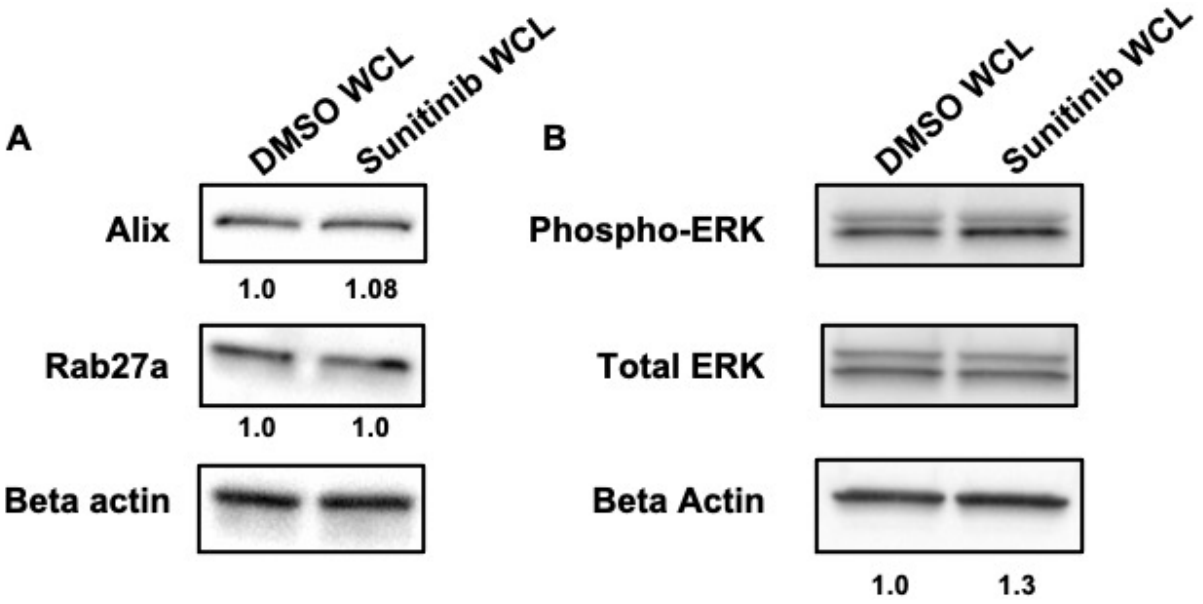

Figure 28. Sunitinib treatment increases levels of phospho-ERK, but not Alix and Rab27a

Representative western blots from 2 independent experiments (n = 2) showing levels of (A) Alix and Rab27a and (B) Phospho-ERK and total ERK after 786-0 cells were treated with 5 μM Sunitinib for 48 hours in Opti-MEM media. Band intensities were first normalized to β-actin loading control, and the subsequent normalized Phospho-ERK band intensities were then normalized to the normalized Total ERK band intensities.

What are the cellular targets and functions of EVs performing glycolysis?

Another interesting future area of research entails investigating the biological purpose of metabolically active sEVs. As reviewed in Chapter IV, EVs represent a novel form of cell-to-cell communication implicated in many areas of cancer biology. A recent study showed that viral infection increases release of iron-containing EVs from respiratory epithelial cells, and the iron carried by EVs can be transferred to promote biofilm growth of the bacteria *Pseudomonas aeruginosa*[370]. Furthermore, there is increasing evidence indicating that EVs perform cell-independent metabolic activities[315,356], suggesting that these vesicles are not simply delivery messengers but rather are actively carrying out biochemical reactions. These findings link the metabolites carried in EVs to important physiological effects with other cells in the environment.

We wondered whether the metabolic activity of EVs affects the metabolism of adjacent tumor cells or adjacent normal kidney epithelial cells. We tested this hypothesis by overexpressing a fluorescent-tagged GLUT1 (mCherry-GLUT1) in 786-0 cells. We observe with western blot that the mCherry-GLUT1 was incorporated into sEVs secreted from 786-0 cells overexpressing this construct [Figure 29A]. After quantifying the number of sEVs with nanoparticle tracking analysis, we treated $3x10^5$ wild-type 786-0 cells or $3x10^5$ HKC normal kidney epithelial cells for twenty-four hours with $2.0x10^9$ sEVs in 3mL of serum-free media. This dose of sEVs represented the maximum amount of sEVs purified from one round of isolation in order to give us the highest probability of seeing uptake. We subsequently washed the cells three times with PBS and then collected the cells by scrapping and analyzed for mCherry fluorescence using a Tali image-based flow cytometer. A ‘negative’ gate was set by using a sample of wild-type 786-0 cells treated with PBS [Figure 29B], while a ‘positive’ gas was set by using a sample of mCherry-GLUT1 expressing 786-0 cells [Figure 29C].

Unfortunately, neither the 786-0 nor the HKC cells treated with mCherry-GLUT1 sEVs exhibited any mCherry florescence [Figure 29D-E].

There are several possible explanations for these results. First, it is possible that the cells took up the sEVs containing mCherry-GLUT1 but not enough to meet the limits of detection by the Tali image-based flow cytometer. Another possibility is the cells took up the sEVs with mCherry-GLUT1, but then quickly degraded the cargo in lysosomes. Finally, the cells and sEVs may not have compatible receptors or honing molecules to allow uptake by these particular cells. Future studies are currently in the pipeline to investigate the different cargo and cellular receptors that permit EVs to preferentially target certain cells.

Another tantalizing speculation is that EVs preceded the first single-cell organisms as early primordial particles[371]. Indeed, there are many similarities between retroviruses and EVs, and it is difficult to distinguish EVs derived from virus-infected cells versus the virus itself[372]. In Chapter V, we demonstrated that EVs can perform glycolysis and generate ATP when glucose is provided, which supports previous studies that EVs are metabolically active. But can EVs grow and divide? What other autonomous biochemical reactions can they perform? Future biochemical studies that uncover their cell-independent functions may reveal the evolutionary history of EVs.

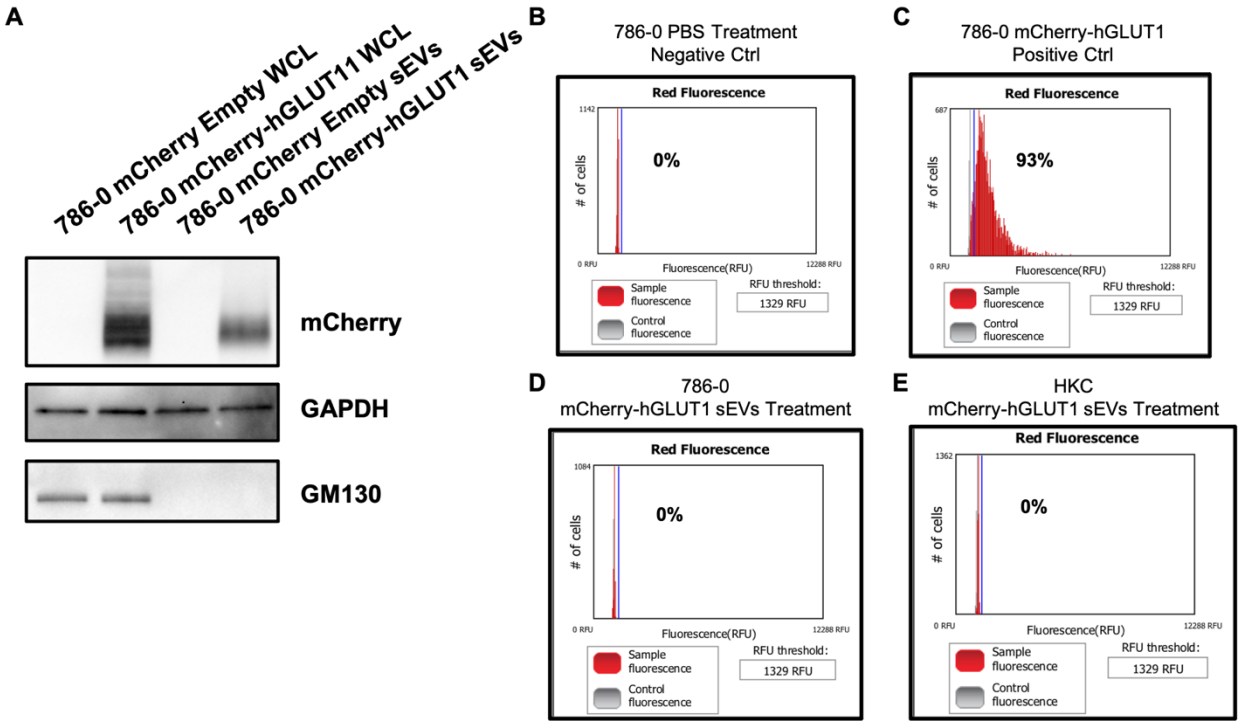

Figure 29. 786-0 sEVs do not transfer GLUT1 to 786-0 or HKC cells

(A) Immunoblot of WCLs and sEVs isolated from 786-0 cells expressing mCherry-Glut1. The mCherry-GLUT1^{+} sEVs were then used to treat wild-type 786-0 cells or HKC cells for 24 hours, and a Tali imaging-based flow cytometer was used to quantify mCherry positive cells. (B) Wild-type 786-0 cells treated with PBS served as a negative control to set the "negative" gate. (C) 786-0 cells expressing mCherry-GLUT1 served as a positive control to set the "positive" gate. mCherry positive cells were not detected in (D) wild-type 786-0 cells or (E) HKC normal kidney epithelial cells after 24 hours of treatment with 2.0 x 10^{9} mCherry-GLUT1^{+} sEVs in 3mL of serum-free media. The data presented above is from one independent experiment (n = 1).

Do metabolically active EVs modulate immune cell metabolism and function in the tumor microenvironment?

Another possible function of these metabolically active EVs is to alter the metabolism of immune cells. As discussed in Chapter II, immune cells are important components of the tumor microenvironment, and each immune cell has a unique metabolic program. T cells in particular are known to require high levels of glucose and other nutrients to fully activate[131]. Previous reports indicate that EVs can suppress T cell activity. For example, PD-L1^{+} exosomes have been shown to interact with PD-1 on T cells, inducing T cell exhaustion and anergy[198,200].

Can metabolic sEVs compete for metabolites with T cells? It has previously been suggested that tumor cells can compete with T cells for important nutrients, leading to their dysfunction and immune evasion[186]. In addition, lactic acid accumulation in the tumor microenvironment was previously shown to inhibit T cell function and proliferation[172,373]. Does the lactate produced by these metabolically active sEVs antagonize T cell function? Answering these questions would define a novel metabolic mechanism by which tumor-derived EVs could modulate immune cell function. Given the importance of immune function to current therapeutic strategies, comprehensively understanding these interactions are paramount to advancing immunotherapies.

We tested these hypotheses by isolating peripheral blood mononuclear cells (PBMCs) from healthy human donor blood by Ficoll separation and plating two million PBMCs into each well of a 48-well dish. PBMCs were the treated for three days with increasing numbers of sEVs isolated from DMSO or Sunitinib-treated 786-0 cells under activating conditions (anti-CD3, anti-CD28, and IL-2). Compared to PBMCs treated with IL-7 control or under activating conditions with PBS, the median fluorescence intensity (MFI) of the activation markers CD71 and C25 on

$CD4^+$ T cells [Figure 30] and $CD8^+$ T cells [Figure 31] in sEV treatment groups varied considerably from donor to donor, likely due to the inherent variability found between donors. $CD4^+$ and $CD8^+$ T cell activation did not display a dose-dependent response to DMSO or Sunitinib sEVs [Figure 30]. We hypothesize that the variability observed in T cell activation to different EV numbers could be due to different EV cargo exerting their predominant effect at different doses. It is also possible that T cells are not the main targets of these EVs – others have reported, for example, that macrophages can have their metabolic phenotype altered by tumor-derived EVs[201]. Our group recently reported that myeloid cells preferentially take up glucose whereas tumor cells preferentially take up glutamine[374].

Tracking EV uptake by different immune cell populations would also provide valuable information about their metabolic effects on these cells. An initial experiment to address this question would be to add the mCherry-tagged GLUT1 sEVs or DiD-labeled sEVs to healthy human donor PBMCs and use flow cytometry to determine which immune cell populations take up the tagged sEVs. One can also intravenously inject the mCherry-tagged GLUT1 sEVs into mice harboring tumors, and then perform flow cytometry to characterize the cell populations that took up these vesicles. Following these studies, we can isolate the populations of cells that took up $GLUT1^+$ sEVs and investigate alterations in their metabolism with glucose uptake assays and glycolytic flux assays using the Seahorse Bioanalyzer machine.

A

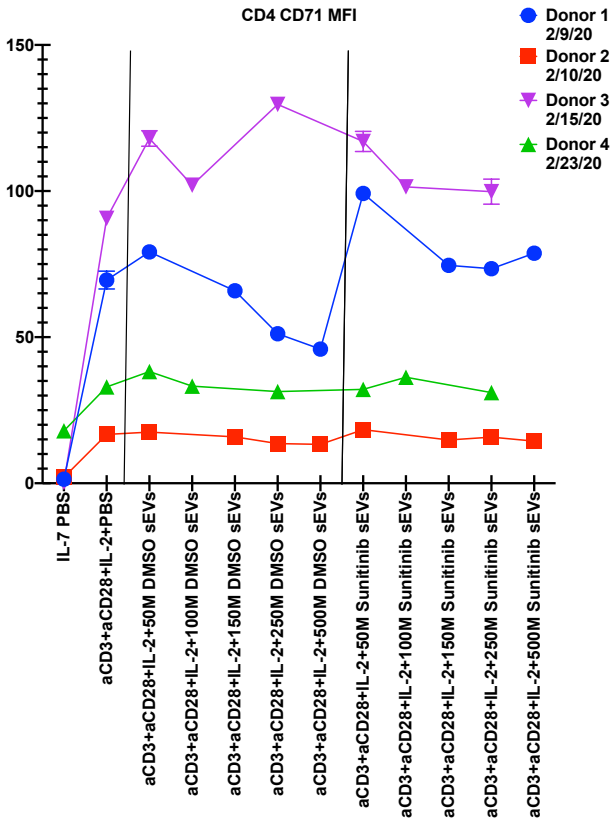
CD4 CD71 MFI
Donor 1 2/9/20
Donor 2 2/10/20
Donor 3 2/15/20
Donor 4 2/23/20
150
100
50
0
IL-7 PBS
aCD3+aCD28+IL-2+PBS
aCD3+aCD28+IL-2+50M DMSO sEVs
aCD3+aCD28+IL-2+100M DMSO sEVs
aCD3+aCD28+IL-2+150M DMSO sEVs
aCD3+aCD28+IL-2+250M DMSO sEVs
aCD3+aCD28+IL-2+500M DMSO sEVs
aCD3+aCD28+IL-2+50M Sunitinib sEVs
aCD3+aCD28+IL-2+100M Sunitinib sEVs
aCD3+aCD28+IL-2+150M Sunitinib sEVs
aCD3+aCD28+IL-2+250M Sunitinib sEVs
aCD3+aCD28+IL-2+500M Sunitinib sEVs

B

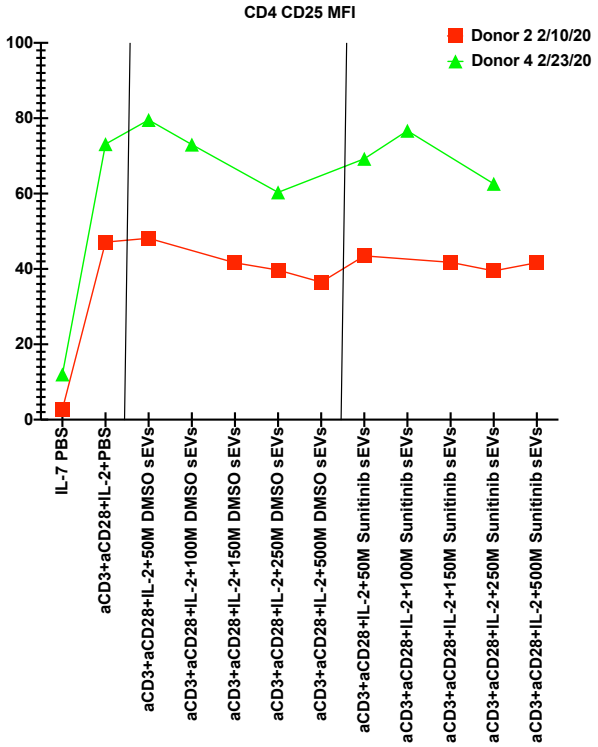
CD4 CD25 MFI
Donor 2 2/10/20
Donor 4 2/23/20
100
80
60
40
20
0
IL-7 PBS
aCD3+aCD28+IL-2+PBS
aCD3+aCD28+IL-2+50M DMSO sEVs
aCD3+aCD28+IL-2+100M DMSO sEVs
aCD3+aCD28+IL-2+150M DMSO sEVs
aCD3+aCD28+IL-2+250M DMSO sEVs
aCD3+aCD28+IL-2+500M DMSO sEVs
aCD3+aCD28+IL-2+50M Sunitinib sEVs
aCD3+aCD28+IL-2+100M Sunitinib sEVs
aCD3+aCD28+IL-2+150M Sunitinib sEVs
aCD3+aCD28+IL-2+250M Sunitinib sEVs
aCD3+aCD28+IL-2+500M Sunitinib sEVs

Figure 30. 786-0 DMSO or Sunitinib sEVs have varying effects on activation of $CD4^+$ T cells from healthy donor blood

PBMCs were treated with IL-7 control with PBS, activating conditions (anti-CD3, anti-CD28, and IL-2) with PBS, or increasing numbers of sEVs from 786-0 DMSO or Sunitinib treated cells under activating conditions. Flow cytometry was used to quantify the median fluorescence intensity (MFI) of (A) CD71 expression from 4 donors (n = 4) and (B) CD25 expression from 2 donors (n = 2) on $CD4^+$ T cells. Data was not significant by two-way ANOVA with post hoc tukey test comparing to the anti-CD3, anti-CD28, and IL-2 with PBS positive control group.

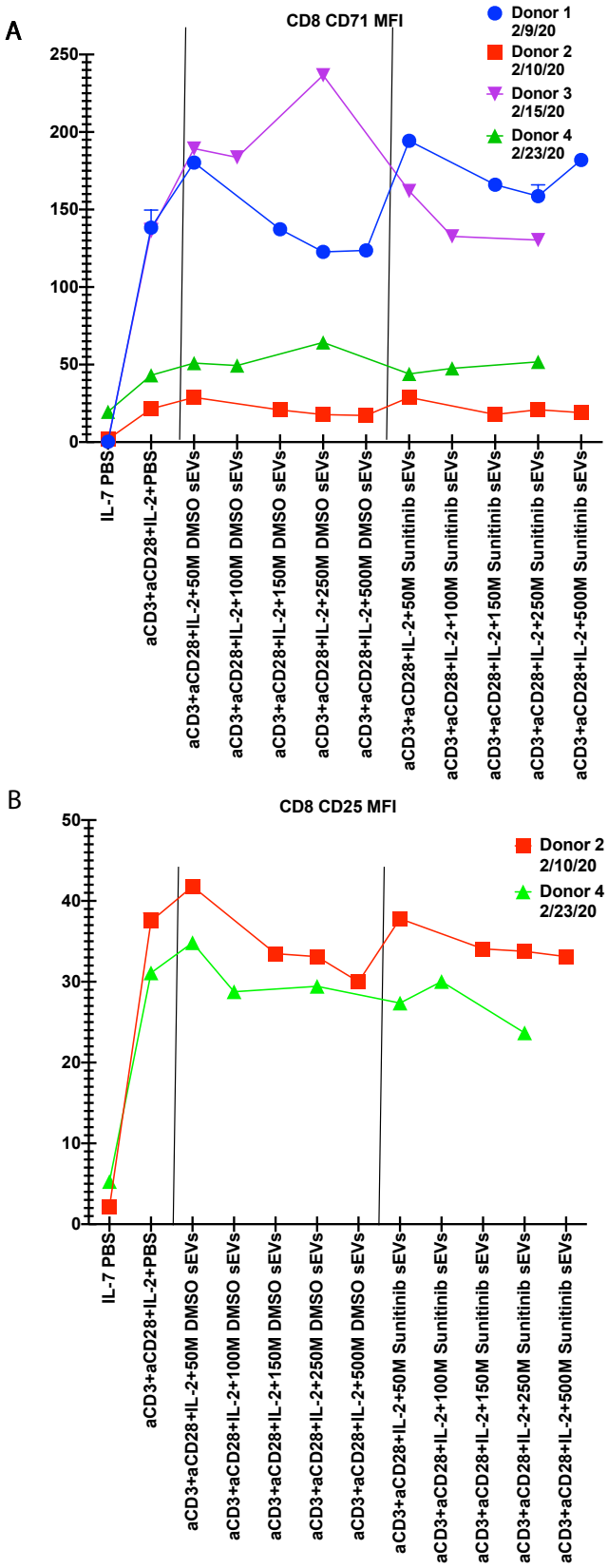
A
CD8 CD71 MFI
Donor 1 2/9/20
Donor 2 2/10/20
Donor 3 2/15/20
Donor 4 2/23/20
250
200
150
100
50
0
IL-7 PBS
aCD3+aCD28+IL-2+PBS
aCD3+aCD28+IL-2+50M DMSO sEVs
aCD3+aCD28+IL-2+100M DMSO sEVs
aCD3+aCD28+IL-2+150M DMSO sEVs
aCD3+aCD28+IL-2+250M DMSO sEVs
aCD3+aCD28+IL-2+500M DMSO sEVs
aCD3+aCD28+IL-2+50M Sunitinib sEVs
aCD3+aCD28+IL-2+100M Sunitinib sEVs
aCD3+aCD28+IL-2+150M Sunitinib sEVs
aCD3+aCD28+IL-2+250M Sunitinib sEVs
aCD3+aCD28+IL-2+500M Sunitinib sEVs
B
CD8 CD25 MFI
Donor 2 2/10/20
Donor 4 2/23/20
50
40
30
20
10
0
IL-7 PBS
aCD3+aCD28+IL-2+PBS
aCD3+aCD28+IL-2+50M DMSO sEVs
aCD3+aCD28+IL-2+100M DMSO sEVs
aCD3+aCD28+IL-2+150M DMSO sEVs
aCD3+aCD28+IL-2+250M DMSO sEVs
aCD3+aCD28+IL-2+500M DMSO sEVs
aCD3+aCD28+IL-2+50M Sunitinib sEVs
aCD3+aCD28+IL-2+100M Sunitinib sEVs
aCD3+aCD28+IL-2+150M Sunitinib sEVs
aCD3+aCD28+IL-2+250M Sunitinib sEVs
aCD3+aCD28+IL-2+500M Sunitinib sEVs

Figure 31. 786-0 DMSO or Sunitinib sEVs have varying effects on activation of $CD8^+$ T cells from healthy donor blood

PBMCs were treated with IL-7 control with PBS, activating conditions (anti-CD3, anti-CD28, and IL-2) with PBS, or increasing numbers of sEVs from 786-0 DMSO or Sunitinib treated cells under activating conditions. Flow cytometry was used to quantify the median fluorescence intensity (MFI) of (A) CD71 expression from 4 donors (n = 4) and (B) CD25 expression from 2 donors (n = 2) on $CD8^+$ T cells. Data was not significant by two-way ANOVA with post hoc tukey test comparing to the anti-CD3, anti-CD28, and IL-2 with PBS positive control group.

Can EVs serve as biomarkers for RCC?

Currently, no reliable biomarker is available for accurate RCC detection in the clinic. Tour de force work led by Dr. Charles Swanton and the TRACERx group revealed that loss of chromosome 3p occurs early in life (in adolescence or even in childhood)[18]. Since the average age of diagnosis of ccRCC is 64 years, that leaves ample time (~50 years) from the first foundational mutational event until ccRCC is diagnosed later in adult life to detect a tumor. The idea of using circulating EVs for clinical applications such as biomarkers for cancer diagnosis has generated considerable excitement in the EV field[244]. Can EVs, either from serum, urine, or other readily accessible bodily fluids, serve as early biomarkers of 3p loss and therefore higher preponderance for development of ccRCC? Furthermore, can EVs from ccRCC patients be used to monitor progression or predict disease outcome?

We have begun investigating the protein cargo of ccRCC cells in order to identify potential biomarkers. sEVs were isolated 786-0 cells cultured in Opti-MEM media with density gradient centrifugation. Protein was then isolated from the sEVs by adding 1% SDS, and Multidimensional Protein Identification Technology (MudPIT) was performed [Table 3]. Unsurprisingly, the top hits included proteins were extracellular matrix proteins such as versican, heparan sulfate, and fibronectin, as well as exosome markers such as ALIX and flotillin-1. These results are consistent with previous proteomics data on sEVs which showed enrichment for proteins involved in exosome biogenesis machinery, cell-matrix adhesion, and cell-cell junctions[375].

An interesting protein that displayed high abundance in 786-0 sEVs was fatty acid synthase – it was the 11th most abundant protein identified in our MudPIT analysis [Table 3]. As discussed in Chapter I, fatty acid synthase expression was shown to predict poor prognosis in

ccRCC patients[108]. The fact that fatty acid synthase was identified in 786-0 sEVs brings up the intriguing idea of using fatty acid synthase levels in sEVs as a biomarker for aggressive disease. Furthermore, we showed in Chapter V that RCC-derived sEVs are glycolytically active. Therefore, it would be interesting to test if fatty acid synthase is actively performing lipid synthesis in 786-0 sEVs. We also are interested in performing comparative proteomics to differentiate protein enriched in sEVs from ccRCC cell lines versus normal kidney cell lines. We also receive blood from RCC patients on a weekly or biweekly basis – it would be prudent to isolate EVs from their blood and compare their cargo to EVs from normal donor blood. These ongoing efforts to unveil the unique cargo of tumor-derived EVs will expand our diagnostic toolkit in oncology.

Identified Proteins	Accession Number	Spectral Count
Versican core protein OS=Homo sapiens GN=VCAN PE=1 SV=3	sp|P13611|CSPG2_HUMAN	396
Basement membrane-specific heparan sulfate proteoglycan core protein OS=Homo sapiens GN=HSPG2 PE=1 SV=4	sp|P98160|PGBM_HUMAN	309
Fibronectin OS=Homo sapiens GN=FN1 PE=1 SV=4	sp|P02751|FINC_HUMAN (+1)	249
Serotransferrin OS=Homo sapiens GN=TF PE=1 SV=3	sp|P02787|TRFE_HUMAN	140
Hemopexin OS=Homo sapiens GN=HPX PE=1 SV=2	sp|P02790|HEMO_HUMAN	117
Galectin-3-binding protein OS=Homo sapiens GN=LGALS3BP PE=1 SV=1	sp|Q08380|LG3BP_HUMAN	116
|prf||754920A albumin [Bos primigenius taurus]	gi|229552	112
Programmed cell death 6-interacting protein OS=Homo sapiens GN=PDCD6IP PE=1 SV=1	sp|Q8WUM4|PDC6I_HUMAN	101
|gb|AAG41947.1| keratin 1 [Homo sapiens]gi|17318569|ref|NP_006112.2| keratin 1 [Homo sapiens]gi|39794653|gb|AAH63697.1| Keratin 1 [Homo sapiens]	gi|11935049 (+1)	92
Fatty acid synthase OS=Homo sapiens GN=FASN PE=1 SV=3	sp|P49327|FAS_HUMAN	81
|sp|P00761|TRYP_PIG TRYPSIN PRECURSOR.	gi|136429	79
Heat shock cognate 71 kDa protein OS=Homo sapiens GN=HSPA8 PE=1 SV=1	sp|P11142|HSP7C_HUMAN	78
Syndecan binding protein (Syntenin), isoform CRA_a OS=Homo sapiens GN=SDCBP PE=4 SV=1	tr|G5EA09|G5EA09_HUMAN	76
Agrin OS=Homo sapiens GN=AGRN PE=1 SV=4	sp|O00468|AGRIN_HUMAN	70
|ref|NP_000217.2| keratin 9 [Homo sapiens]	gi|55956899 (+1)	62
|ref|NP_000412.2| keratin 10 [Homo sapiens]gi|21961605|gb|AAH34697.1| Keratin 10 [Homo sapiens]	gi|40354192 (+3)	58
Myoferlin OS=Homo sapiens GN=MYOF PE=1 SV=1	sp|Q9NZM1|MYOF_HUMAN (+1)	57
Sodium/potassium-transporting ATPase subunit alpha-1 OS=Homo sapiens GN=ATP1A1 PE=1 SV=1	sp|P05023|AT1A1_HUMAN	57
Flotillin-1 OS=Homo sapiens GN=FLOT1 PE=1 SV=3	sp|O75955|FLOT1_HUMAN	55
Actin, cytoplasmic 1 OS=Homo sapiens GN=ACTB PE=1 SV=1	sp|P60709|ACTB_HUMAN (+1)	47

|gb|AAC83410.1| epidermal cytokeratin 2 [Homo sapiens]gi|2565257|gb|AAB81946.1| keratin 2e [Homo sapiens]gi|482387|pir||A44861 keratin, 67K type II epidermal - humangi|547754|sp|P35908|K22E_HUMAN Keratin, type II cytoskeletal 2 epidermal (Cytokeratin 2e) (K2e) (CK 2e)	gi|181402 (+2)	45
Polyubiquitin-B OS=Homo sapiens GN=UBB PE=1 SV=1	sp|P0CG47|UBB_HUMAN (+18)	45
4F2 cell-surface antigen heavy chain OS=Homo sapiens GN=SLC3A2 PE=1 SV=3	sp|P08195|4F2_HUMAN (+2)	36
Clathrin heavy chain 1 OS=Homo sapiens GN=CLTC PE=1 SV=5	sp|Q00610|CLH1_HUMAN	36
Ras-related protein Rab-7a OS=Homo sapiens GN=RAB7A PE=1 SV=1	sp|P51149|RAB7A_HUMAN	35
Heat shock 70 kDa protein 1A/1B OS=Homo sapiens GN=HSPA1A PE=1 SV=5	sp|P08107|HSP71_HUMAN	34
Flotillin-2 OS=Homo sapiens GN=FLOT2 PE=1 SV=2	sp|Q14254|FLOT2_HUMAN	30
Collagen alpha-1(XVIII) chain OS=Homo sapiens GN=COL18A1 PE=1 SV=5	sp|P39060|COIA1_HUMAN	29
Cytoplasmic dynein 1 heavy chain 1 OS=Homo sapiens GN=DYNC1H1 PE=1 SV=5	sp|Q14204|DYHC1_HUMAN	29
Epidermal growth factor receptor OS=Homo sapiens GN=EGFR PE=1 SV=2	sp|P00533|EGFR_HUMAN (+1)	29
Pyruvate kinase isozymes M1/M2 OS=Homo sapiens GN=PKM PE=1 SV=4	sp|P14618|KPYM_HUMAN	29
CD63 antigen OS=Homo sapiens GN=CD63 PE=1 SV=2	sp|P08962|CD63_HUMAN (+6)	27
Elongation factor 2 OS=Homo sapiens GN=EEF2 PE=1 SV=4	sp|P13639|EF2_HUMAN	27
Thrombospondin-1 OS=Homo sapiens GN=THBS1 PE=1 SV=2	sp|P07996|TSP1_HUMAN	27
Transforming growth factor-beta-induced protein ig-h3 OS=Homo sapiens GN=TGFBI PE=1 SV=1	sp|Q15582|BGH3_HUMAN (+1)	27
Ephrin type-A receptor 2 OS=Homo sapiens GN=EPHA2 PE=1 SV=2	sp|P29317|EPHA2_HUMAN	26
Integrin beta-1 OS=Homo sapiens GN=ITGB1 PE=1 SV=2	sp|P05556|ITB1_HUMAN	25
Myosin-9 OS=Homo sapiens GN=MYH9 PE=1 SV=4	sp|P35579|MYH9_HUMAN	24
Prostaglandin F2 receptor negative regulator OS=Homo sapiens GN=PTGFRN PE=1 SV=2	sp|Q9P2B2|FPRP_HUMAN	24

EGF-like repeat and discoidin I-like domain-containing protein 3 OS=Homo sapiens GN=EDIL3 PE=1 SV=1	sp|O43854|EDIL3_HUMAN	23
Solute carrier family 2, facilitated glucose transporter member 1 OS=Homo sapiens GN=SLC2A1 PE=1 SV=2	sp|P11166|GTR1_HUMAN	23

Table 3. List of proteins identified in 786-0 sEVs in MudPIT proteomics analysis

786-0 cells were cultured in Opti-MEM media for 48 hours, and their sEVs from the culture media were subsequently isolated by density gradient ultracentrifugation. Protein was isolated from sEVs and underwent MudPIT proteomic analysis. Only proteins with a spectral count of 23 or higher are listed. Results are from one independent experiment (n = 1).

Can SETD2 regulate EV secretion?

Several groups have discovered non-histone targets of SETD2's methylation activity, including cytoskeletal proteins such as actin and tubulin[57,58]. Loss of SETD2 led to the reduction in actin lysine 68 trimethylation and thus impairment of cell migration in ccRCC cells, suggesting that SETD2 is a critical regulator of actin polymerization/depolymerization dynamics[57]. Chapter IV briefly discussed the role of cytoskeletal proteins in vesicle trafficking and exosome release. For example, MVBs travel along microtubules to reach the plasma membrane. MVBs subsequently dock and fuse with the plasma membrane to release exosomes, a process mediated by RABs, actin, and SNARE proteins[249]. Pharmacological inhibition of Neural Wiskott-Aldrich Syndrome Protein (N-WASp), which is critical for actin polymerization at invadopodia, reduced exosome secretion by 70-80%[376]. Thus, an intriguing idea is mutations in *SETD2* may alter EV secretion from ccRCC cells by de-regulating microtubule and/or actin polymerization/depolymerization dynamics.

We tested this hypothesis by isolating sEVs from *SETD2* knockdown (KD) normal kidney HKC cells and wild-type HKC cells using density gradient centrifugation. With western blot, we confirmed knockdown of *SETD2* [Figure 32A], and with nanoparticle tracking analysis, we observed a reduction in sEVs secretion from knockdown cells compared to wild-type cells [Figure 32B].

A critical future direction will be to determine whether defects in actin polymerization or microtubule formation from *SETD2* loss abrogates sEVs secretion. One may potentially use the recently developed pHluo_M153R-CD63-mScarlett construct[287] to visualize MVB trafficking and fusion in live cells with and without *SETD2* loss or catalytically-dead SET-domain mutants (tSETD2-R1625C). In addition, determining any changes in the MVB life cycle in cells

expressing mutant actin K68A, which is insensitive to methylation by SETD2, would be interesting to see.

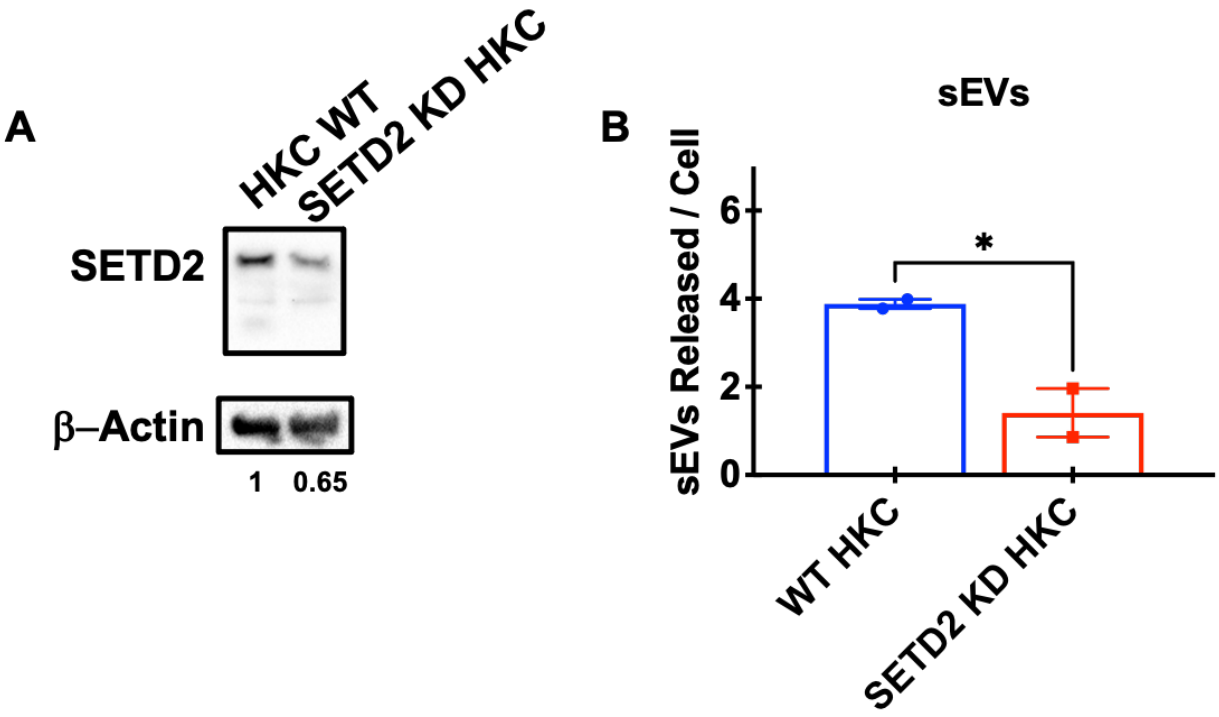

Figure 32. SETD2 loss in HKC cells promotes sEV secretion and HRS expression

(A) Representative western blots from two independent experiments (n = 2) showing levels of SETD2 protein levels in wild-type (WT) HKC cells vs. *SETD2* knock-down (KD) HKC cells. Band intensities were first normalized to β-actin loading control. (B) Nanoparticle tracking analysis quantification of sEVs secreted from WT HKC cells vs. *SETD2* KD HKC cells. Bars represent the mean of two independent experiment (n = 2), and the error bars represent the SEM. * $p < 0.05$ two-sided unpaired Student's t-test.

Appendix A

CHROMOPHOBE RENAL CELL CARCINOMA

Aaron R. Lim and W. Kimryn Rathmell, M.D., Ph.D.

The work presented in this section is republished with permission from a chapter in *Rare Kidney Tumors: Comprehensive Multidisciplinary Management and Emerging Therapies*[377] written to expand my knowledge about the scope of RCC; permission conveyed through Copyright Clearance Center.

Defining Chromophobe Renal Cell Carcinoma

Chromophobe renal cell carcinoma (ChRCC) makes up approximately 5% of all cases of renal cell carcinoma (RCC)[378]. First described in 1985, this rare subtype of RCC was originally thought to arise from the intercalated cells of the collecting ducts. This disease is challenging to diagnose, and on biopsy this malignancy can share histologic similarities with benign oncocytomas using conventional evaluation, or even be misclassified as the more common clear cell RCC[379–381]. Therefore, careful histologic attention is needed to appropriately capture these cases. Histologically, two variants of ChRCC are recognized: classic ChRCC and an eosinophilic variant[382]. The classic type is more common and is characterized by large cells with pale "chromophobe" cytoplasm and a perinuclear halo or clearing. On the other hand, the tumor cells

in the eosinophilic variant display a dense eosinophilic cytoplasm and perinuclear halos [Figure 33].

Karyotyping studies have recognized for some time that there is a characteristic pattern of chromosome loss that is recurrent in this disease[383,384]. The high frequency loss of one copy of chromosomes 1, 2, 6, 10, 13, and 17 remains a conundrum that will be discussed in detail below. Recent genetic analysis of ChRCC by The Cancer Genome Atlas (TCGA) confirmed this unique genomic landscape that distinguishes this rare subtype from clear cell renal cell carcinoma (ccRCC) and papillary renal cell carcinoma (pRCC). In addition to the large-scale loss of multiple chromosomes, this disease is also characterized by high frequency of mutations in *TP53* and *PTEN*[385]. Although most cases of ChRCC occur sporadically, a subset of patients with Tuberous Sclerosis Complex and Birt-Hogg-Dubé syndrome develop a renal neoplasm consistent with a chromophobe histology[386,387].

Clinical staging of ChRCC is derived from other forms of RCC. However, Fuhrman grading, which is used for grading ccRCC, does not provide prognostic value for ChRCC[388,389]. Although other grading systems for ChRCC have been developed, these other systems have not been rigorously tested[390]. Thus, the International Society of Urologic Pathology recommends that ChRCC should be not be graded[391].

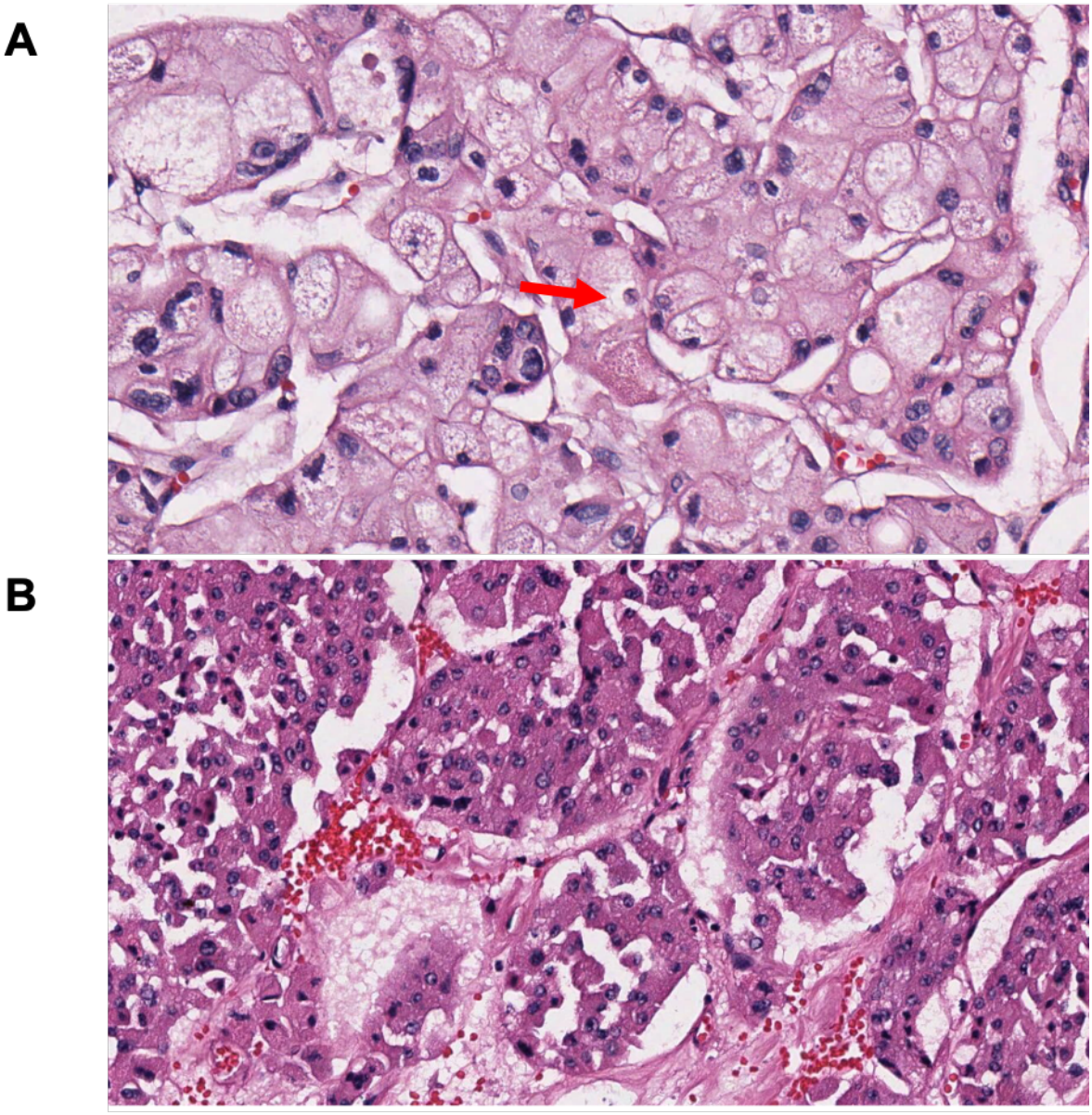

Figure 33. Pathology of classic and eosinophilic ChRCC

(A) A representative H&E stain of a classic ChRCC highlighting cells with pale cytoplasm and a perinuclear halo (red arrow). (B) A representative H&E stain of an eosinophilic variant of ChRCC showing crowded cells with eosinophilic cytoplasm. Images obtained from http://cancer.digitalslidearchive.net, TCGA-KL-8324-01Z-00-DX1, TCGA-KN-8436-01Z-00-DX1, and reproduced with permission.

Genomic Landscape of Chromophobe Renal Cell Carcinoma

An important genetic feature of ChRCC, introduced above, is the loss of numerous chromosomes [Figure 34]. Copy number analysis of 66 ChRCC samples in the TCGA showed frequent loss of chromosomes 1, 2, 6, 10, 13, and 17[385]. Less frequently, but still at significantly higher frequency than observed in other tumors, chromosomes 3, 5, 8, 9, 11, 18, and 21 show evidence of loss[385]. The reason behind the extensive loss of genomic material remains unknown.

Using whole exome sequencing, the TCGA demonstrated that *TP53* is the most commonly mutated gene in ChRCC. It is notable that this common tumor suppressor is rarely mutated in ccRCC and pRCC[385]. Along with frequent loss of chromosome 17, frequent *TP53* mutation suggests that deficiency of p53 may be one feature driving ChRCC tumorigenesis. The second most commonly mutated gene in ChRCC identified by the TCGA is *PTEN*.[385] In combination with frequent loss of chromosome 10, complete absence of PTEN points to constitutive activation of the PI3K/AKT/mTOR signaling pathway in ChRCC, which may explain the efficacy of mTOR inhibitors in ChRCC[385].

Interestingly, a subset of tumors in the TCGA showed increased expression of telomerase, which is encoded by the *TERT* gene. Unexpectedly, whole genome sequencing revealed that the tumors with the highest telomerase expression had genomic breakpoints within the *TERT* promoter leading to structural rearrangement[385]. This finding has spawned a new search for structural variants due to mutations outside the TERT open reading frame that can alter TERT protein levels.

In addition to these distinctions, expression based profiling has demonstrated that these tumors share transcriptional features most consistent with a distal tubule origin, when compared

with microdissected kidney tubule segments[66,392]. This is in contrast to both clear cell and papillary type RCC, which map more closely to the proximal tubule segments. Taken together, these genomic features unique to ChRCC support the argument that ChRCC is a completely different cancer, derived from a separate geographic region of the nephron and with a distinct mutational profile, that distinguishes this malignancy from the other RCC subtypes[393].

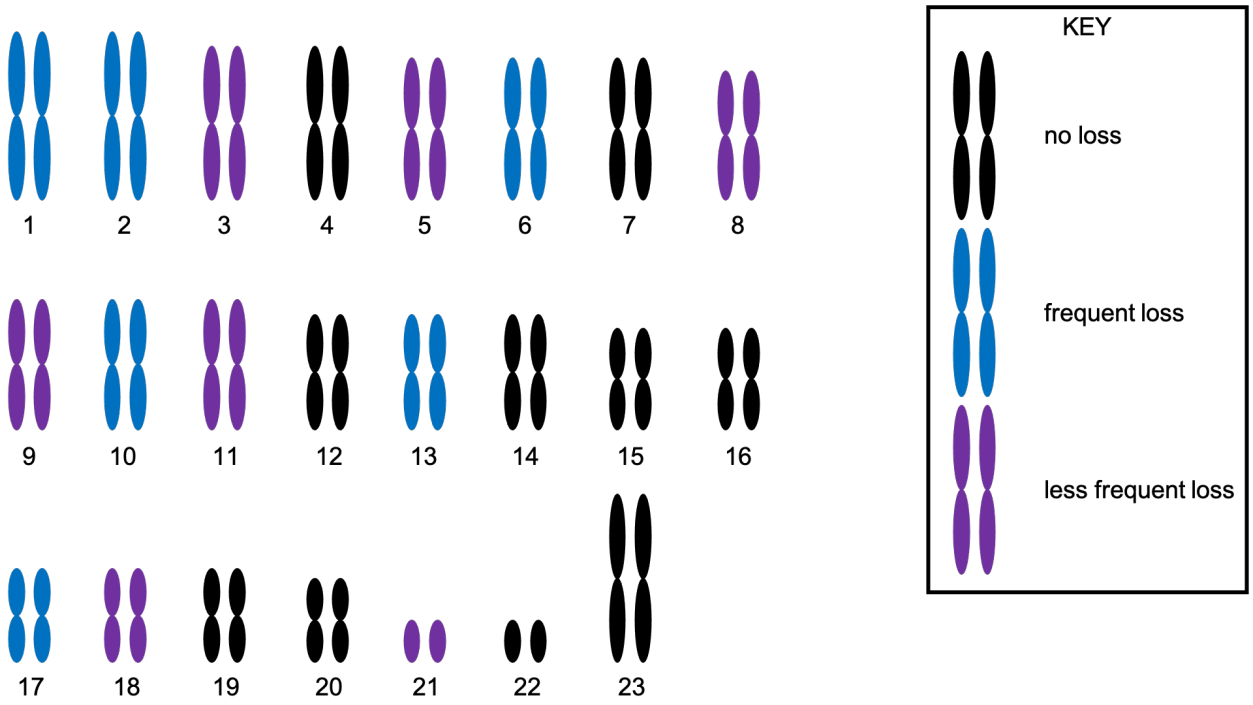

Figure 34. Hypodiploidy in ChRCC

Chromosomes 1, 2, 6, 10, 13, and 17 are frequently lost in ChRCC (blue chromosomes). Chromosomes 3, 5, 8, 9, 11, 18, and 21 are less frequently lost in ChRCC (purple chromosomes), though still at an elevated rate compared to other tumors.

Hereditary Forms of Chromophobe Renal Cell Carcinoma

Several genetic conditions have been associated with the development of ChRCC, including Birt-Hogg-Dubé (BHD) syndrome and Tuberous Sclerosis Complex (TSC). Named after three physicians who described it in a Canadian family in 1977, BHD syndrome is an autosomal dominant condition characterized by fibrofolliculomas, pulmonary cysts, spontaneous pneumothorax, and kidney neoplasms[394,395]. Approximately 12-34% of BHD patients will develop a renal neoplasm, 40% of which are ChRCC[387,396,397]. Other renal tumors found in this syndrome include oncocytomas, hybrid oncocytic/chromophobe tumors, and ccRCC[398]. Genetically, patients with BHD syndrome harbor germline mutations in the tumor suppressor gene *FLCN*, which is rarely mutated in sporadic cases of ChRCC[399–401]. The majority of these mutations result in truncation of the folliculin protein[396,402]. Numerous functions of folliculin have been proposed, including regulating AKT/mTOR and TGFβ signaling, sequestering transcription factor E3 in the cytoplasm, and facilitating cell-cell adhesion[403–407]. However, further studies are needed to elucidate the connection between the functions of this tumor suppressor and the manifestations of BHD syndrome.

TSC is an autosomal dominant condition that results from mutations in either *TSC1* or *TSC2,* causing severe neurologic dysfunction and tumors in the brain, kidney, skin, heart, and lung[408,409]. Inactivating either of these tumor suppressor genes leads to increased activation of mTOR signaling and cellular proliferation[410]. Renal disease in TSC, which is the second leading cause of death in these patients, includes renal angiomyolipomas, renal cysts, and RCC[411]. Although patients with TSC have a similar incidence of RCC as the general population (2-3%), they tend to develop these tumors at a median age of 28 years, which is 25 years younger than

the general population[411,412]. A recent study of 46 renal tumors from TSC patients showed that 33% contained a hybrid oncocytic/chromophobe phenotype, though it is important to note that TSC-associated RCCs encompass other histologic subtypes including ccRCC and pRCC[412–414].

Metabolism of Chromophobe Renal Cell Carcinoma

It had previously been shown that mitochondrial DNA was altered in both oncocytomas and the eosinophilic variant of ChRCC, both of which have been known to contain an abundance of mitochondria[415,416]. The TCGA extended their analysis of ChRCC to include mitochondrial DNA and found that 18% of their ChRCC tumors had mutations leading to inactivation of the electron transport chain (ETC) complex I[385]. *MT-ND5*, which encodes an essential component of ETC complex I called NADH dehydrogenase 5, was the most frequently altered mitochondrial gene and correlated strongly with the eosinophilic ChRCC variant[385,417]. However, mutations in ETC complex I did not correlate with loss of oxidative phosphorylation[385]. It remains to be determined whether inactivation of ETC complex I triggers increased mitochondrial abundance as a compensatory mechanism or if it leads to an alternative metabolic route to support ChRCC.

Clinical Aspects and Management of Chromophobe Renal Cell Carcinoma

ChRCC has a more favorable prognosis than ccRCC and pRCC, with five-year survival rates ranging from 78% to 100%[418]. This beneficial survival stems largely from the overall better prognosis for localized disease, which generally shows low risk for metastatic spread. Although most cases of ChRCC remain localized, metastatic cases of ChRCC have been known to

occur[419,420]. However, only 1.3% of patients with ChRCC present with metastatic disease, and they usually have a better prognosis compared to patients with other metastatic RCC subtypes[421,422]. Factors that predict worse prognosis include sarcomatoid dedifferentiation, microscopic necrosis, and advanced stage[418].

Due to the rarity of ChRCC, studies on how to manage patients with ChRCC are scarce. ChRCC patients are usually managed similarly to ccRCC patients, with localized disease being treated with surgical resection. Surgical guidelines for the management of this cancer are applied from those developed for ccRCC. Advanced ChRCC remains difficult to treat, and it is strongly recommended to enroll these patients into chromophobe-specific clinical trials[423]. Most studies that investigate treatment for RCC exclude non-ccRCC patients, and those that include non-ccRCC subtypes are usually made up of mostly pRCC patients with a small number of ChRCC patients.

Historical therapies such as interferon and IL-2 have not been shown to be efficacious in advanced ChRCC. For example, in a study of 64 patients with metastatic non-ccRCC, only one of the twelve patients with metastatic ChRCC responded to interferon alpha 2a, IL-2, or combination of interferon alpha 2a and IL-2 therapy[422]. Chemotherapy is of limited use in the renal cell carcinomas, as discussed elsewhere in this text. A phase II trial showed that only one out of seven patients with ChRCC had a complete response to capecitabine monotherapy[424]. Thus, systemic chemotherapy is not currently recommended for advanced ChRCC, although the new data demonstrating the strong association with TP53 mutations is rekindling interest in the possibility for chemotherapy to be re-investigated in this disease.

On the other hand, patients with advanced ChRCC have been shown to respond to the targeted therapies that are widely used in ccRCC, such as vascular endothelial growth factor

receptor (VEGFR) inhibitors and mTOR inhibitors. One study showed that 25% of metastatic ChRCC patients in five US and French institutions had clinical response to VEGFR inhibitors sunitinib and sorafenib compared to only 5% of metastatic pRCC patients[425]. Similar results were demonstrated in a recent phase II trial which showed that metastatic ChRCC patients treated with sunitinib had a 40% response rate and a median progression free survival of 12.7 months[426]. Since *PTEN* mutations and loss of chromosome 10 have been found in ChRCC, mTOR inhibitors have a strong biological rationale and have been investigated as potential therapies for ChRCC patients. A subtype group analysis from the phase III global advanced renal cell carcinoma (ARCC) trial demonstrated that temsirolimus had superior efficacy compared to interferon in non-ccRCC subtypes[427]. In addition, ChRCC patients in a recent phase II Korean study had a median progression-free survival of 13.1 months on everolimus, whereas pRCC patients had a median progression-free survival of only 3.4 months[428]. In the ESPN trial comparing everolimus and sunitinib, neither drug showed superiority as a first-line therapy for metastatic non-ccRCC[429]. However, the ASPEN trial, which included more patients than the ESPN trial, concluded that metastatic ChRCC patients treated with everolimus had longer median progression-free survival compared to those treated with sunitinib, which was the opposite result they saw for pRCC patients[430]. Taken together, these trials show that both VEGFR and mTOR inhibitors may provide therapeutic benefit to patients with advanced ChRCC, though future studies should investigate molecular biomarkers that can predict response to targeted therapies.

Other therapies such as radiation therapy and immune checkpoint blockade have not been extensively studied in ChRCC. There is no clear role for using radiation to treat ChRCC except as a means for palliative care. Although immune checkpoint inhibitors such as Nivolumab, a

monoclonal antibody targeting PD-1, have demonstrated efficacy in ccRCC, their efficacy in ChRCC remains unknown. Choueiri *et al.* recently characterized PD-L1 expression in non-ccRCC tumors and found that patients with PD-L1^{+} tumors have worse prognoses[431]. In addition, there is currently a clinical trial investigating Nivolumab's efficacy and safety in advanced non-ccRCC patients (ClinicalTrials.gov Identifier: NCT02596035). Thus, immune checkpoint blockade represents an interesting area of future study for ChRCC.

Conclusion

ChRCC is a rare subtype of RCC that is usually indolent compared to the other RCC subtypes. With the TCGA's recent comprehensive genetic analysis of ChRCC, we have learned that ChRCC has distinct genomic features, including an unprecedented loss of numerous chromosomes, mutations in *TP53* and *PTEN*, rearrangements in the *TERT* promoter, and mutations in mitochondrial DNA. BHD syndrome and TSC are two examples of genetic syndromes that predispose individuals to developing ChRCC, though most ChRCC cases are sporadic. These unique genomic characteristics underscore the importance of distinguishing ChRCC from the other RCC subtypes. Even though there is strong evidence to consider ChRCC as a separate disease from ccRCC, we currently do not have separate treatment guidelines for ChRCC. Although recent clinical trials have shown that advanced ChRCC patients may respond to targeted therapy such as VEGFR and mTOR inhibitors, current studies that have non-ccRCC patients are dominated by pRCC patients and simply do not enroll enough ChRCC patients due to its rarity. Thus, it is prudent to further our understanding of its molecular biology and establish

clinical trials that include more ChRCC patients in order to develop better therapies for this distinct disease entity.

REFERENCES

1. American Cancer Society. Cancer Facts & Figures 2021. (2021).
2. Saad, A. M. *et al.* Trends in renal cell carcinoma incidence and mortality in the united states in the last 2 decades: a SEER-based study. *Clin. Genitourin. Cancer* **17**, 46-57.e5 (2019).
3. King, S. C., Pollack, L. A., Li, J., King, J. B. & Master, V. A. Continued increase in incidence of renal cell carcinoma, especially in young patients and high grade disease: United States 2001 to 2010. *J. Urol.* **191**, 1665–1670 (2014).
4. Padala, S. A. *et al.* Epidemiology of Renal Cell Carcinoma. *World J. Oncol.* **11**, 79–87 (2020).
5. Jonasch, E., Gao, J. & Rathmell, W. K. Renal cell carcinoma. *BMJ* **349**, g4797 (2014).
6. Sims, J. N. *et al.* Racial Disparities and Preventive Measures to Renal Cell Carcinoma. *Int. J. Environ. Res. Public Health* **15**, (2018).
7. Srigley, J. R. *et al.* The International Society of Urological Pathology (ISUP) Vancouver Classification of Renal Neoplasia. *Am. J. Surg. Pathol.* **37**, 1469–1489 (2013).
8. Moch, H., Cubilla, A. L., Humphrey, P. A., Reuter, V. E. & Ulbright, T. M. The 2016 WHO Classification of Tumours of the Urinary System and Male Genital Organs-Part A: Renal, Penile, and Testicular Tumours. *Eur. Urol.* **70**, 93–105 (2016).
9. Choueiri, T. K. & Motzer, R. J. Systemic therapy for metastatic renal cell carcinoma. *N. Engl. J. Med.* **376**, 354–366 (2017).
10. Motzer, R. J. *et al.* Molecular Subsets in Renal Cancer Determine Outcome to Checkpoint and Angiogenesis Blockade. *Cancer Cell* (2020). doi:10.1016/j.ccell.2020.10.011
11. Huang, J. J. & Hsieh, J. J. The Pan-Omics Landscape of Renal Cell Carcinoma and Its

Implication on Future Clinical Practice. *Kidney cancer (Clifton, Va.)* **4**, 121–129 (2020).

12. Clark, D. J. *et al.* Integrated Proteogenomic Characterization of Clear Cell Renal Cell Carcinoma. *Cell* **179**, 964-983.e31 (2019).
13. Turajlic, S. *et al.* Deterministic Evolutionary Trajectories Influence Primary Tumor Growth: TRACERx Renal. *Cell* **173**, 595-610.e11 (2018).
14. Cancer Genome Atlas Research Network. Comprehensive molecular characterization of clear cell renal cell carcinoma. *Nature* **499**, 43–49 (2013).
15. Sato, Y. *et al.* Integrated molecular analysis of clear-cell renal cell carcinoma. *Nat. Genet.* **45**, 860–867 (2013).
16. Linehan, W. M., Lerman, M. I. & Zbar, B. Identification of the von Hippel-Lindau (VHL) gene. Its role in renal cancer. *JAMA* **273**, 564–570 (1995).
17. Gossage, L., Eisen, T. & Maher, E. R. VHL, the story of a tumour suppressor gene. *Nat. Rev. Cancer* **15**, 55–64 (2015).
18. Mitchell, T. J. *et al.* Timing the Landmark Events in the Evolution of Clear Cell Renal Cell Cancer: TRACERx Renal. *Cell* **173**, 611-623.e17 (2018).
19. Lonser, R. R. *et al.* von Hippel-Lindau disease. *Lancet* **361**, 2059–2067 (2003).
20. Kaelin, W. G. The von Hippel–Lindau Tumor Suppressor Protein. *Annu. Rev. Cancer Biol.* **2**, 91–109 (2018).
21. Kaelin, W. G. J. The VHL tumor suppressor gene: insights into oxygen sensing and cancer. *Trans. Am. Clin. Climatol. Assoc.* **128**, 298–307 (2017).
22. Kaelin, W. G. J. & Ratcliffe, P. J. Oxygen sensing by metazoans: the central role of the HIF hydroxylase pathway. *Mol. Cell* **30**, 393–402 (2008).
23. Maxwell, P. H. *et al.* The tumour suppressor protein VHL targets hypoxia-inducible

factors for oxygen-dependent proteolysis. *Nature* **399**, 271–275 (1999).

24. Keith, B., Johnson, R. S. & Simon, M. C. HIF1α and HIF2α: sibling rivalry in hypoxic tumour growth and progression. *Nat. Rev. Cancer* **12**, 9–22 (2011).

25. Kaelin, W. G. J. The von Hippel-Lindau tumour suppressor protein: O2 sensing and cancer. *Nat. Rev. Cancer* **8**, 865–873 (2008).

26. Kondo, K., Kim, W. Y., Lechpammer, M. & Kaelin, W. G. J. Inhibition of HIF2alpha is sufficient to suppress pVHL-defective tumor growth. *PLoS Biol.* **1**, E83 (2003).

27. Kondo, K., Klco, J., Nakamura, E., Lechpammer, M. & Kaelin, W. G. J. Inhibition of HIF is necessary for tumor suppression by the von Hippel-Lindau protein. *Cancer Cell* **1**, 237–246 (2002).

28. Shen, C. *et al.* Genetic and functional studies implicate HIF1α as a 14q kidney cancer suppressor gene. *Cancer Discov.* **1**, 222–35 (2011).

29. Klatte, T. *et al.* Cytogenetic profile predicts prognosis of patients with clear cell renal cell carcinoma. *J. Clin. Oncol.* **27**, 746–753 (2009).

30. Maranchie, J. K. *et al.* The contribution of VHL substrate binding and HIF1-alpha to the phenotype of VHL loss in renal cell carcinoma. *Cancer Cell* **1**, 247–255 (2002).

31. Raval, R. R. *et al.* Contrasting properties of hypoxia-inducible factor 1 (HIF-1) and HIF-2 in von Hippel-Lindau-associated renal cell carcinoma. *Mol. Cell. Biol.* **25**, 5675–5686 (2005).

32. Hoefflin, R. *et al.* HIF-1α and HIF-2α differently regulate tumour development and inflammation of clear cell renal cell carcinoma in mice. *Nat. Commun.* **11**, 4111 (2020).

33. Courtney, K. D. *et al.* HIF-2 Complex Dissociation, Target Inhibition, and Acquired Resistance with PT2385, a First-in-Class HIF-2 Inhibitor, in Patients with Clear Cell

Renal Cell Carcinoma. *Clin. Cancer Res.* **26**, 793–803 (2020).

34. Chen, W. *et al.* Targeting renal cell carcinoma with a HIF-2 antagonist. *Nature* **539**, 112–117 (2016).

35. Harlander, S. *et al.* Combined mutation in Vhl, Trp53 and Rb1 causes clear cell renal cell carcinoma in mice. *Nat. Med.* **23**, 869–877 (2017).

36. Frew, I. J. *et al.* pVHL and PTEN tumour suppressor proteins cooperatively suppress kidney cyst formation. *EMBO J.* **27**, 1747–1757 (2008).

37. Albers, J. *et al.* Combined mutation of Vhl and Trp53 causes renal cysts and tumours in mice. *EMBO Mol. Med.* **5**, 949–964 (2013).

38. Allis, C. D. & Jenuwein, T. The molecular hallmarks of epigenetic control. *Nat. Rev. Genet.* **17**, 487–500 (2016).

39. Strahl, B. D. & Allis, C. D. The language of covalent histone modifications. *Nature* **403**, 41–45 (2000).

40. Carril-Ajuria, L., Santos, M., Roldán-Romero, J. M., Rodriguez-Antona, C. & de Velasco, G. Prognostic and Predictive Value of PBRM1 in Clear Cell Renal Cell Carcinoma. *Cancers (Basel).* **12**, (2019).

41. Hakimi, A. A. *et al.* Clinical and pathologic impact of select chromatin-modulating tumor suppressors in clear cell renal cell carcinoma. *Eur. Urol.* **63**, 848–854 (2013).

42. Joseph, R. W. *et al.* Clear Cell Renal Cell Carcinoma Subtypes Identified by BAP1 and PBRM1 Expression. *J. Urol.* **195**, 180–187 (2016).

43. Ho, T. H. *et al.* Loss of histone H3 lysine 36 trimethylation is associated with an increased risk of renal cell carcinoma-specific death. *Mod. Pathol.* **29**, 34–42 (2016).

44. Pawłowski, R. *et al.* Loss of PBRM1 expression is associated with renal cell carcinoma

progression. *Int. J. cancer* **132**, E11-7 (2013).

45. Kadoch, C. & Crabtree, G. R. Mammalian SWI/SNF chromatin remodeling complexes and cancer: Mechanistic insights gained from human genomics. *Sci. Adv.* **1**, e1500447 (2015).

46. Gao, W., Li, W., Xiao, T., Liu, X. S. & Kaelin, W. G. J. Inactivation of the PBRM1 tumor suppressor gene amplifies the HIF-response in VHL-/- clear cell renal carcinoma. *Proc. Natl. Acad. Sci. U. S. A.* **114**, 1027–1032 (2017).

47. Peña-Llopis, S. *et al.* BAP1 loss defines a new class of renal cell carcinoma. *Nat. Genet.* **44**, 751–759 (2012).

48. de Cubas, A. A. & Rathmell, W. K. Epigenetic modifiers: activities in renal cell carcinoma. *Nat. Rev. Urol.* **15**, 599–614 (2018).

49. Faber, P. W. *et al.* Huntingtin interacts with a family of WW domain proteins. *Hum. Mol. Genet.* **7**, 1463–1474 (1998).

50. Li, J. *et al.* SETD2: an epigenetic modifier with tumor suppressor functionality. *Oncotarget* **7**, 50719–50734 (2016).

51. Fahey, C. C. & Davis, I. J. SETting the Stage for Cancer Development: SETD2 and the Consequences of Lost Methylation. *Cold Spring Harb. Perspect. Med.* **7**, (2017).

52. Dalgliesh, G. L. *et al.* Systematic sequencing of renal carcinoma reveals inactivation of histone modifying genes. *Nature* **463**, 360–363 (2010).

53. Carvalho, S. *et al.* SETD2 is required for DNA double-strand break repair and activation of the p53-mediated checkpoint. *Elife* **3**, e02482 (2014).

54. Kanu, N. *et al.* SETD2 loss-of-function promotes renal cancer branched evolution through replication stress and impaired DNA repair. *Oncogene* **34**, 5699–5708 (2015).

55. Simon, J. M. *et al.* Variation in chromatin accessibility in human kidney cancer links H3K36 methyltransferase loss with widespread RNA processing defects. *Genome Res.* **24**, 241–250 (2014).

56. Neri, F. *et al.* Intragenic DNA methylation prevents spurious transcription initiation. *Nature* **543**, 72–77 (2017).

57. Seervai, R. N. H. *et al.* The Huntingtin-interacting protein SETD2/HYPB is an actin lysine methyltransferase. *Sci. Adv.* **6**, (2020).

58. Park, I. Y. *et al.* Dual Chromatin and Cytoskeletal Remodeling by SETD2. *Cell* **166**, 950–962 (2016).

59. Chiang, Y.-C. *et al.* SETD2 Haploinsufficiency for Microtubule Methylation Is an Early Driver of Genomic Instability in Renal Cell Carcinoma. *Cancer Res.* **78**, 3135–3146 (2018).

60. Chen, K. *et al.* Methyltransferase SETD2-Mediated Methylation of STAT1 Is Critical for Interferon Antiviral Activity. *Cell* **170**, 492-506.e14 (2017).

61. Yuan, H. *et al.* SETD2 Restricts Prostate Cancer Metastasis by Integrating EZH2 and AMPK Signaling Pathways. *Cancer Cell* **38**, 350-365.e7 (2020).

62. Lawrence, M. S. *et al.* Discovery and saturation analysis of cancer genes across 21 tumour types. *Nature* **505**, 495–501 (2014).

63. Akbani, R. *et al.* A pan-cancer proteomic perspective on The Cancer Genome Atlas. *Nat. Commun.* **5**, 3887 (2014).

64. Guo, H. *et al.* The PI3K/AKT Pathway and Renal Cell Carcinoma. *J. Genet. Genomics* **42**, 343–353 (2015).

65. Li, J. *et al.* TCPA: a resource for cancer functional proteomics data. *Nature methods* **10**,

1046–1047 (2013).

66. Chen, F. *et al.* Multilevel genomics-based taxonomy of renal cell carcinoma. *Cell Rep.* **14**, 2476–2489 (2016).

67. Hager, M. *et al.* Increased activated Akt expression in renal cell carcinomas and prognosis. *J. Cell. Mol. Med.* **13**, 2181–2188 (2009).

68. Fruman, D. A. *et al.* The PI3K Pathway in Human Disease. *Cell* **170**, 605–635 (2017).

69. Hoxhaj, G. & Manning, B. D. The PI3K-AKT network at the interface of oncogenic signalling and cancer metabolism. *Nat. Rev. Cancer* **20**, 74–88 (2020).

70. Bilanges, B., Posor, Y. & Vanhaesebroeck, B. PI3K isoforms in cell signalling and vesicle trafficking. *Nat. Rev. Mol. Cell Biol.* **20**, 515–534 (2019).

71. Engelman, J. A. Targeting PI3K signalling in cancer: opportunities, challenges and limitations. *Nat. Rev. Cancer* **9**, 550–562 (2009).

72. Fritsch, R. *et al.* RAS and RHO families of GTPases directly regulate distinct phosphoinositide 3-kinase isoforms. *Cell* **153**, 1050–1063 (2013).

73. Dbouk, H. A. *et al.* G protein-coupled receptor-mediated activation of p110β by Gβγ is required for cellular transformation and invasiveness. *Sci. Signal.* **5**, ra89 (2012).

74. Auger, K. R., Serunian, L. A., Soltoff, S. P., Libby, P. & Cantley, L. C. PDGF-dependent tyrosine phosphorylation stimulates production of novel polyphosphoinositides in intact cells. *Cell* **57**, 167–175 (1989).

75. Lee, Y.-R., Chen, M. & Pandolfi, P. P. The functions and regulation of the PTEN tumour suppressor: new modes and prospects. *Nat. Rev. Mol. Cell Biol.* **19**, 547–562 (2018).

76. Song, M. S., Salmena, L. & Pandolfi, P. P. The functions and regulation of the PTEN tumour suppressor. *Nat. Rev. Mol. Cell Biol.* **13**, 283–296 (2012).

77. Thorpe, L. M., Yuzugullu, H. & Zhao, J. J. PI3K in cancer: divergent roles of isoforms, modes of activation and therapeutic targeting. *Nat. Rev. Cancer* **15**, 7–24 (2015).

78. Manning, B. D. & Toker, A. AKT/PKB Signaling: Navigating the Network. *Cell* **169**, 381–405 (2017).

79. Vadlakonda, L., Dash, A., Pasupuleti, M., Anil Kumar, K. & Reddanna, P. The Paradox of Akt-mTOR Interactions. *Front. Oncol.* **3**, 165 (2013).

80. Manning, B. D. & Cantley, L. C. AKT/PKB signaling: navigating downstream. *Cell* **129**, 1261–1274 (2007).

81. Kim, L. C., Cook, R. S. & Chen, J. mTORC1 and mTORC2 in cancer and the tumor microenvironment. *Oncogene* **36**, 2191–2201 (2017).

82. Ma, X. M. & Blenis, J. Molecular mechanisms of mTOR-mediated translational control. *Nat. Rev. Mol. Cell Biol.* **10**, 307–318 (2009).

83. Toschi, A., Lee, E., Gadir, N., Ohh, M. & Foster, D. A. Differential dependence of hypoxia-inducible factors 1 alpha and 2 alpha on mTORC1 and mTORC2. *J. Biol. Chem.* **283**, 34495–34499 (2008).

84. Bernardi, R. *et al.* PML inhibits HIF-1alpha translation and neoangiogenesis through repression of mTOR. *Nature* **442**, 779–785 (2006).

85. Holmes, D. PI3K pathway inhibitors approach junction. *Nat. Rev. Drug Discov.* **10**, 563–4 (2011).

86. Hanahan, D. & Weinberg, R. A. Hallmarks of cancer: the next generation. *Cell* **144**, 646–674 (2011).

87. Warburg, O., Wind, F. & Negelein, E. The metabolism of tumors in the body. *J. Gen. Physiol.* **8**, 519–530 (1927).

88. Lunt, S. Y. & Vander Heiden, M. G. Aerobic glycolysis: meeting the metabolic requirements of cell proliferation. *Annu. Rev. Cell Dev. Biol.* **27**, 441–464 (2011).

89. Rathmell, W. K., Rathmell, J. C. & Linehan, W. M. Metabolic Pathways in Kidney Cancer: Current Therapies and Future Directions. *J. Clin. Oncol.* JCO2018792309 (2018). doi:10.1200/JCO.2018.79.2309

90. Bacigalupa, Z. A. & Rathmell, W. K. Beyond glycolysis: Hypoxia signaling as a master regulator of alternative metabolic pathways and the implications in clear cell renal cell carcinoma. *Cancer Lett.* **489**, 19–28 (2020).

91. Wettersten, H. I., Aboud, O. A., Lara, P. N. J. & Weiss, R. H. Metabolic reprogramming in clear cell renal cell carcinoma. *Nat. Rev. Nephrol.* **13**, 410–419 (2017).

92. Gordan, J. D. & Simon, M. C. Hypoxia-inducible factors: central regulators of the tumor phenotype. *Curr. Opin. Genet. Dev.* **17**, 71–77 (2007).

93. Hu, C.-J., Wang, L.-Y., Chodosh, L. A., Keith, B. & Simon, M. C. Differential roles of hypoxia-inducible factor 1alpha (HIF-1alpha) and HIF-2alpha in hypoxic gene regulation. *Mol. Cell. Biol.* **23**, 9361–9374 (2003).

94. Yoshino, H. *et al.* PHGDH as a Key Enzyme for Serine Biosynthesis in HIF2α-Targeting Therapy for Renal Cell Carcinoma. *Cancer Res.* **77**, 6321–6329 (2017).

95. Chappell, J. C., Payne, L. B. & Rathmell, W. K. Hypoxia, angiogenesis, and metabolism in the hereditary kidney cancers. *J. Clin. Invest.* **129**, 442–451 (2019).

96. Chan, D. A. *et al.* Targeting GLUT1 and the Warburg effect in renal cell carcinoma by chemical synthetic lethality. *Sci. Transl. Med.* **3**, 94ra70 (2011).

97. Hakimi, A. A. *et al.* An Integrated Metabolic Atlas of Clear Cell Renal Cell Carcinoma. *Cancer Cell* **29**, 104–116 (2016).

98. Wettersten, H. I. *et al.* Grade-Dependent Metabolic Reprogramming in Kidney Cancer Revealed by Combined Proteomics and Metabolomics Analysis. *Cancer Res.* **75**, 2541–2552 (2015).

99. Li, B. *et al.* Fructose-1,6-bisphosphatase opposes renal carcinoma progression. *Nature* **513**, 251–255 (2014).

100. Abu Aboud, O. *et al.* Glutamine Addiction in Kidney Cancer Suppresses Oxidative Stress and Can Be Exploited for Real-Time Imaging. *Cancer Res.* **77**, 6746–6758 (2017).

101. Gameiro, P. A. *et al.* In vivo HIF-mediated reductive carboxylation is regulated by citrate levels and sensitizes VHL-deficient cells to glutamine deprivation. *Cell Metab.* **17**, 372–385 (2013).

102. Okazaki, A. *et al.* Glutaminase and poly(ADP-ribose) polymerase inhibitors suppress pyrimidine synthesis and VHL-deficient renal cancers. *J. Clin. Invest.* **127**, 1631–1645 (2017).

103. Meric-Bernstam, F. *et al.* Phase 1 study of CB-839, a small molecule inhibitor of glutaminase (GLS), alone and in combination with everolimus (E) in patients (pts) with renal cell cancer (RCC). *J. Clin. Oncol.* **34**, 4568 (2016).

104. Shim, E.-H. *et al.* L-2-Hydroxyglutarate: an epigenetic modifier and putative oncometabolite in renal cancer. *Cancer Discov.* **4**, 1290–1298 (2014).

105. Wise, D. R. *et al.* Hypoxia promotes isocitrate dehydrogenase-dependent carboxylation of α-ketoglutarate to citrate to support cell growth and viability. *Proc. Natl. Acad. Sci. U. S. A.* **108**, 19611–19616 (2011).

106. Metallo, C. M. *et al.* Reductive glutamine metabolism by IDH1 mediates lipogenesis under hypoxia. *Nature* **481**, 380–384 (2011).

107. Gebhard, R. L. *et al.* Abnormal cholesterol metabolism in renal clear cell carcinoma. *J. Lipid Res.* **28**, 1177–1184 (1987).

108. Horiguchi, A. *et al.* Fatty acid synthase over expression is an indicator of tumor aggressiveness and poor prognosis in renal cell carcinoma. *J. Urol.* **180**, 1137–1140 (2008).

109. von Roemeling, C. A. *et al.* Stearoyl-CoA desaturase 1 is a novel molecular therapeutic target for clear cell renal cell carcinoma. *Clin. Cancer Res.* **19**, 2368–2380 (2013).

110. Du, W. *et al.* HIF drives lipid deposition and cancer in ccRCC via repression of fatty acid metabolism. *Nat. Commun.* **8**, 1769 (2017).

111. Perroud, B., Ishimaru, T., Borowsky, A. D. & Weiss, R. H. Grade-dependent proteomics characterization of kidney cancer. *Mol. Cell. Proteomics* **8**, 971–985 (2009).

112. McDermott, D. F. *et al.* The high-dose aldesleukin 'select' trial: a trial to prospectively validate predictive models of response to treatment in patients with metastatic renal cell carcinoma. *Clin. Cancer Res.* **21**, 561–568 (2015).

113. Motzer, R. J., Bacik, J., Murphy, B. A., Russo, P. & Mazumdar, M. Interferon-Alfa as a Comparative Treatment for Clinical Trials of New Therapies Against Advanced Renal Cell Carcinoma. *J. Clin. Oncol.* **20**, 289–296 (2002).

114. Dizman, N., Philip, E. J. & Pal, S. K. Genomic profiling in renal cell carcinoma. *Nat. Rev. Nephrol.* **16**, 435–451 (2020).

115. Motzer, R. J. *et al.* Sunitinib versus interferon alfa in metastatic renal-cell carcinoma. *N. Engl. J. Med.* **356**, 115–124 (2007).

116. Rini, B. I. *et al.* Phase III trial of bevacizumab plus interferon alfa versus interferon alfa monotherapy in patients with metastatic renal cell carcinoma: final results of CALGB

90206. *J. Clin. Oncol.* **28**, 2137–2143 (2010).

117. Rini, B. I. *et al.* Comparative effectiveness of axitinib versus sorafenib in advanced renal cell carcinoma (AXIS): a randomised phase 3 trial. *Lancet* **378**, 1931–1939 (2011).

118. Motzer, R. J. *et al.* Axitinib versus sorafenib as second-line treatment for advanced renal cell carcinoma: overall survival analysis and updated results from a randomised phase 3 trial. *Lancet. Oncol.* **14**, 552–562 (2013).

119. Motzer, R. J. *et al.* Pazopanib versus sunitinib in metastatic renal-cell carcinoma. *N. Engl. J. Med.* **369**, 722–731 (2013).

120. Choueiri, T. K. *et al.* Cabozantinib versus Everolimus in Advanced Renal-Cell Carcinoma. *N. Engl. J. Med.* **373**, 1814–1823 (2015).

121. Rini, B. I. & Atkins, M. B. Resistance to targeted therapy in renal-cell carcinoma. *Lancet. Oncol.* **10**, 992–1000 (2009).

122. Xu, W., Atkins, M. B. & McDermott, D. F. Checkpoint inhibitor immunotherapy in kidney cancer. *Nat. Rev. Urol.* **17**, 137–150 (2020).

123. Siska, P. J. *et al.* Mitochondrial dysregulation and glycolytic insufficiency functionally impair CD8 T cells infiltrating human renal cell carcinoma. *JCI insight* **2**, (2017).

124. Motzer, R. J. *et al.* Nivolumab versus Everolimus in Advanced Renal-Cell Carcinoma. *N. Engl. J. Med.* **373**, 1803–1813 (2015).

125. Motzer, R. J. *et al.* Avelumab plus Axitinib versus Sunitinib for advanced renal cell carcinoma. *N. Engl. J. Med.* **380**, 1103–1115 (2019).

126. Rini, B. I. *et al.* Pembrolizumab plus Axitinib versus Sunitinib for advanced renal cell carcinoma. *N. Engl. J. Med.* **380**, 1116–1127 (2019).

127. Motzer, R. *et al.* Lenvatinib plus Pembrolizumab or Everolimus for Advanced Renal Cell

Carcinoma. *N. Engl. J. Med.* (2021). doi:10.1056/NEJMoa2035716

128. Choueiri, T. K. *et al.* Nivolumab plus Cabozantinib versus Sunitinib for Advanced Renal-Cell Carcinoma. *N. Engl. J. Med.* **384**, 829–841 (2021).

129. Lee, W. S., Yang, H., Chon, H. J. & Kim, C. Combination of anti-angiogenic therapy and immune checkpoint blockade normalizes vascular-immune crosstalk to potentiate cancer immunity. *Exp. Mol. Med.* **52**, 1475–1485 (2020).

130. Hack, S. P., Zhu, A. X. & Wang, Y. Augmenting Anticancer Immunity Through Combined Targeting of Angiogenic and PD-1/PD-L1 Pathways: Challenges and Opportunities. *Front. Immunol.* **11**, 598877 (2020).

131. Lim, A. R., Rathmell, W. K. & Rathmell, J. C. The tumor microenvironment as a metabolic barrier to effector T cells and immunotherapy. *Elife* **9**, (2020).

132. Lebelo, M. T., Joubert, A. M. & Visagie, M. H. Warburg effect and its role in tumourigenesis. *Arch. Pharm. Res.* **42**, 833–847 (2019).

133. Pavlova, N. N. & Thompson, C. B. The Emerging Hallmarks of Cancer Metabolism. *Cell Metab.* **23**, 27–47 (2016).

134. Menk, A. V *et al.* Early TCR Signaling Induces Rapid Aerobic Glycolysis Enabling Distinct Acute T Cell Effector Functions. *Cell Rep.* **22**, 1509–1521 (2018).

135. Bantug, G. R., Galluzzi, L., Kroemer, G. & Hess, C. The spectrum of T cell metabolism in health and disease. *Nat. Rev. Immunol.* **18**, 19–34 (2018).

136. Kouidhi, S., Elgaaied, A. B. & Chouaib, S. Impact of Metabolism on T-Cell Differentiation and Function and Cross Talk with Tumor Microenvironment. *Front. Immunol.* **8**, 270 (2017).

137. Baumeister, S. H., Freeman, G. J., Dranoff, G. & Sharpe, A. H. Coinhibitory Pathways in

Immunotherapy for Cancer. *Annu. Rev. Immunol.* **34**, 539–573 (2016).

138. Gong, J., Chehrazi-Raffle, A., Reddi, S. & Salgia, R. Development of PD-1 and PD-L1 inhibitors as a form of cancer immunotherapy: a comprehensive review of registration trials and future considerations. *J. Immunother. cancer* **6**, 8 (2018).

139. Geltink, R. I. K., Kyle, R. L. & Pearce, E. L. Unraveling the Complex Interplay Between T Cell Metabolism and Function. *Annu. Rev. Immunol.* **36**, 461–488 (2018).

140. Chapman, N. M., Boothby, M. R. & Chi, H. Metabolic coordination of T cell quiescence and activation. *Nat. Rev. Immunol.* (2019). doi:10.1038/s41577-019-0203-y

141. Sena, L. A. *et al.* Mitochondria are required for antigen-specific T cell activation through reactive oxygen species signaling. *Immunity* **38**, 225–236 (2013).

142. Frauwirth, K. A. *et al.* The CD28 signaling pathway regulates glucose metabolism. *Immunity* **16**, 769–777 (2002).

143. Wang, R. *et al.* The transcription factor Myc controls metabolic reprogramming upon T lymphocyte activation. *Immunity* **35**, 871–882 (2011).

144. Palazon, A. *et al.* An HIF-1alpha/VEGF-A Axis in Cytotoxic T Cells Regulates Tumor Progression. *Cancer Cell* **32**, 669-683.e5 (2017).

145. Macintyre, A. N. *et al.* The glucose transporter Glut1 is selectively essential for CD4 T cell activation and effector function. *Cell Metab.* **20**, 61–72 (2014).

146. Chang, C.-H. *et al.* Posttranscriptional control of T cell effector function by aerobic glycolysis. *Cell* **153**, 1239–1251 (2013).

147. Angiari, S. *et al.* Regulation of T cell activation and pathogenicity by dimeric pyruvate kinase M2 (PKM2). *J. Immunol.* **202**, 125.11 LP-125.11 (2019).

148. Sinclair, L. V *et al.* Antigen receptor control of methionine metabolism in T cells. *Elife* **8**,

(2019).

149. Sinclair, L. V *et al.* Control of amino-acid transport by antigen receptors coordinates the metabolic reprogramming essential for T cell differentiation. *Nat. Immunol.* **14**, 500–508 (2013).

150. Najjar, Y. G. *et al.* Tumor cell oxidative metabolism as a barrier to PD-1 blockade immunotherapy in melanoma. *JCI insight* **4**, (2019).

151. Johnson, M. O. *et al.* Distinct Regulation of Th17 and Th1 Cell Differentiation by Glutaminase-Dependent Metabolism. *Cell* **175**, 1780-1795.e19 (2018).

152. Leone, R. D. *et al.* Glutamine blockade induces divergent metabolic programs to overcome tumor immune evasion. *Science* **366**, 1013–1021 (2019).

153. Buck, M. D. *et al.* Mitochondrial Dynamics Controls T Cell Fate through Metabolic Programming. *Cell* **166**, 63–76 (2016).

154. Klein Geltink, R. I. *et al.* Mitochondrial Priming by CD28. *Cell* **171**, 385-397.e11 (2017).

155. Ron-Harel, N. *et al.* Mitochondrial Biogenesis and Proteome Remodeling Promote One-Carbon Metabolism for T Cell Activation. *Cell Metab.* **24**, 104–117 (2016).

156. Ma, E. H. *et al.* Metabolic Profiling Using Stable Isotope Tracing Reveals Distinct Patterns of Glucose Utilization by Physiologically Activated CD8(+) T Cells. *Immunity* **51**, 856-870.e5 (2019).

157. Araki, K. *et al.* mTOR regulates memory CD8 T-cell differentiation. *Nature* **460**, 108–112 (2009).

158. Pearce, E. L. *et al.* Enhancing CD8 T-cell memory by modulating fatty acid metabolism. *Nature* **460**, 103–107 (2009).

159. Cui, G. *et al.* IL-7-Induced Glycerol Transport and TAG Synthesis Promotes Memory

CD8+ T Cell Longevity. *Cell* **161**, 750–761 (2015).

160. van der Windt, G. J. W. *et al.* Mitochondrial respiratory capacity is a critical regulator of CD8+ T cell memory development. *Immunity* **36**, 68–78 (2012).

161. Gubser, P. M. *et al.* Rapid effector function of memory CD8+ T cells requires an immediate-early glycolytic switch. *Nat. Immunol.* **14**, 1064–1072 (2013).

162. Bantug, G. R. *et al.* Mitochondria-Endoplasmic Reticulum Contact Sites Function as Immunometabolic Hubs that Orchestrate the Rapid Recall Response of Memory CD8(+) T Cells. *Immunity* **48**, 542-555.e6 (2018).

163. Fraser, K. A., Schenkel, J. M., Jameson, S. C., Vezys, V. & Masopust, D. Preexisting high frequencies of memory CD8+ T cells favor rapid memory differentiation and preservation of proliferative potential upon boosting. *Immunity* **39**, 171–183 (2013).

164. McLane, L. M., Abdel-Hakeem, M. S. & Wherry, E. J. CD8 T Cell Exhaustion During Chronic Viral Infection and Cancer. *Annu. Rev. Immunol.* **37**, 457–495 (2019).

165. Khan, O. *et al.* TOX transcriptionally and epigenetically programs CD8(+) T cell exhaustion. *Nature* **571**, 211–218 (2019).

166. Saeidi, A. *et al.* T-Cell Exhaustion in Chronic Infections: Reversing the State of Exhaustion and Reinvigorating Optimal Protective Immune Responses. *Front. Immunol.* **9**, 2569 (2018).

167. Schurich, A. *et al.* Distinct Metabolic Requirements of Exhausted and Functional Virus-Specific CD8 T Cells in the Same Host. *Cell Rep.* **16**, 1243–1252 (2016).

168. Fisicaro, P. *et al.* Targeting mitochondrial dysfunction can restore antiviral activity of exhausted HBV-specific CD8 T cells in chronic hepatitis B. *Nat. Med.* **23**, 327–336 (2017).

169. Bengsch, B. *et al.* Bioenergetic Insufficiencies Due to Metabolic Alterations Regulated by the Inhibitory Receptor PD-1 Are an Early Driver of CD8(+) T Cell Exhaustion. *Immunity* **45**, 358–373 (2016).

170. Scharping, N. E. *et al.* The Tumor Microenvironment Represses T Cell Mitochondrial Biogenesis to Drive Intratumoral T Cell Metabolic Insufficiency and Dysfunction. *Immunity* **45**, 374–388 (2016).

171. Gemta, L. F. *et al.* Impaired enolase 1 glycolytic activity restrains effector functions of tumor-infiltrating CD8(+) T cells. *Sci. Immunol.* **4**, (2019).

172. Brand, A. *et al.* LDHA-Associated Lactic Acid Production Blunts Tumor Immunosurveillance by T and NK Cells. *Cell Metab.* **24**, 657–671 (2016).

173. Ma, X. *et al.* Cholesterol Induces CD8(+) T Cell Exhaustion in the Tumor Microenvironment. *Cell Metab.* **30**, 143-156.e5 (2019).

174. Gubin, M. M. *et al.* Checkpoint blockade cancer immunotherapy targets tumour-specific mutant antigens. *Nature* **515**, 577–581 (2014).

175. Harris, A. L. Hypoxia--a key regulatory factor in tumour growth. *Nat. Rev. Cancer* **2**, 38–47 (2002).

176. Wilson, W. R. & Hay, M. P. Targeting hypoxia in cancer therapy. *Nat. Rev. Cancer* **11**, 393–410 (2011).

177. Marx, J. Cell biology. How cells endure low oxygen. *Science* **303**, 1454–6 (2004).

178. Papandreou, I., Cairns, R. A., Fontana, L., Lim, A. L. & Denko, N. C. HIF-1 mediates adaptation to hypoxia by actively downregulating mitochondrial oxygen consumption. *Cell Metab.* **3**, 187–197 (2006).

179. Kim, J., Tchernyshyov, I., Semenza, G. L. & Dang, C. V. HIF-1-mediated expression of

pyruvate dehydrogenase kinase: a metabolic switch required for cellular adaptation to hypoxia. *Cell Metab.* **3**, 177–185 (2006).

180. Gropper, Y. *et al.* Culturing CTLs under Hypoxic Conditions Enhances Their Cytolysis and Improves Their Anti-tumor Function. *Cell Rep.* **20**, 2547–2555 (2017).

181. Shen, X. *et al.* Recent Findings in the Regulation of Programmed Death Ligand 1 Expression. *Front. Immunol.* **10**, 1337 (2019).

182. Noman, M. Z. *et al.* PD-L1 is a novel direct target of HIF-1alpha, and its blockade under hypoxia enhanced MDSC-mediated T cell activation. *J. Exp. Med.* **211**, 781–790 (2014).

183. Ben-Shoshan, J., Maysel-Auslender, S., Mor, A., Keren, G. & George, J. Hypoxia controls CD4+CD25+ regulatory T-cell homeostasis via hypoxia-inducible factor-1alpha. *Eur. J. Immunol.* **38**, 2412–2418 (2008).

184. Hatfield, S. M. *et al.* Immunological mechanisms of the antitumor effects of supplemental oxygenation. *Sci. Transl. Med.* **7**, 277ra30 (2015).

185. Ho, P.-C. *et al.* Phosphoenolpyruvate Is a Metabolic Checkpoint of Anti-tumor T Cell Responses. *Cell* **162**, 1217–1228 (2015).

186. Chang, C. *et al.* Metabolic competition in the tumor microenvironment is a driver of cancer progression. *Cell* **162**, 1229–1241 (2015).

187. Zhao, E. *et al.* Cancer mediates effector T cell dysfunction by targeting microRNAs and EZH2 via glycolysis restriction. *Nat. Immunol.* **17**, 95–103 (2016).

188. Kim, K. H. & Roberts, C. W. M. Targeting EZH2 in cancer. *Nat. Med.* **22**, 128–134 (2016).

189. Sullivan, M. R. *et al.* Quantification of microenvironmental metabolites in murine cancers reveals determinants of tumor nutrient availability. *Elife* **8**, (2019).

190. Zhang, Y. *et al.* Enhancing CD8(+) T Cell Fatty Acid Catabolism within a Metabolically Challenging Tumor Microenvironment Increases the Efficacy of Melanoma Immunotherapy. *Cancer Cell* **32**, 377-391.e9 (2017).

191. Munn, D. H. & Mellor, A. L. Indoleamine 2,3 dioxygenase and metabolic control of immune responses. *Trends Immunol.* **34**, 137–143 (2013).

192. Mezrich, J. D. *et al.* An interaction between kynurenine and the aryl hydrocarbon receptor can generate regulatory T cells. *J. Immunol.* **185**, 3190–3198 (2010).

193. Fallarino, F. *et al.* Modulation of tryptophan catabolism by regulatory T cells. *Nat. Immunol.* **4**, 1206–1212 (2003).

194. Siska, P. J. & Rathmell, J. C. T cell metabolic fitness in antitumor immunity. *Trends Immunol.* **36**, 257–264 (2015).

195. Fischer, K. *et al.* Inhibitory effect of tumor cell-derived lactic acid on human T cells. *Blood* **109**, 3812–3819 (2007).

196. Harel, M. *et al.* Proteomics of Melanoma Response to Immunotherapy Reveals Mitochondrial Dependence. *Cell* **0**, (2019).

197. Tkach, M., Kowal, J. & Thery, C. Why the need and how to approach the functional diversity of extracellular vesicles. *Philos. Trans. R. Soc. Lond. B. Biol. Sci.* **373**, (2018).

198. Chen, G. *et al.* Exosomal PD-L1 contributes to immunosuppression and is associated with anti-PD-1 response. *Nature* **560**, 382–386 (2018).

199. Ricklefs, F. L. *et al.* Immune evasion mediated by PD-L1 on glioblastoma-derived extracellular vesicles. *Sci. Adv.* **4**, eaar2766 (2018).

200. Poggio, M. *et al.* Suppression of exosomal PD-L1 Induces systemic anti-tumor immunity and memory. *Cell* **177**, 414-427.e13 (2019).

201. Wang, X. *et al.* Hypoxic Tumor-Derived Exosomal miR-301a Mediates M2 Macrophage Polarization via PTEN/PI3Kgamma to Promote Pancreatic Cancer Metastasis. *Cancer Res.* **78**, 4586–4598 (2018).

202. Wan, L. *et al.* Exosomes from activated hepatic stellate cells contain GLUT1 and PKM2: a role for exosomes in metabolic switch of liver nonparenchymal cells. *FASEB J.* **33**, 8530–8542 (2019).

203. Zhang, Q. *et al.* Mutant KRAS exosomes alter the metabolic state of recipient colonic epithelial cells. *Cell. Mol. Gastroenterol. Hepatol.* **5**, 627-629.e6 (2018).

204. Cianciaruso, C. *et al.* Molecular Profiling and Functional Analysis of Macrophage-Derived Tumor Extracellular Vesicles. *Cell Rep.* **27**, 3062-3080.e11 (2019).

205. Parry, R. V *et al.* CTLA-4 and PD-1 receptors inhibit T-cell activation by distinct mechanisms. *Mol. Cell. Biol.* **25**, 9543–9553 (2005).

206. Patsoukis, N. *et al.* PD-1 alters T-cell metabolic reprogramming by inhibiting glycolysis and promoting lipolysis and fatty acid oxidation. *Nat. Commun.* **6**, 6692 (2015).

207. Zhang, C. *et al.* STAT3 Activation-Induced Fatty Acid Oxidation in CD8+ T Effector Cells Is Critical for Obesity-Promoted Breast Tumor Growth. *Cell Metab.* (2019). doi:10.1016/j.cmet.2019.10.013

208. Chang, C.-H. & Pearce, E. L. Emerging concepts of T cell metabolism as a target of immunotherapy. *Nat. Immunol.* **17**, 364–368 (2016).

209. Sukumar, M. *et al.* Inhibiting glycolytic metabolism enhances CD8+ T cell memory and antitumor function. *J. Clin. Invest.* **123**, 4479–4488 (2013).

210. Clever, D. *et al.* Oxygen Sensing by T Cells Establishes an Immunologically Tolerant Metastatic Niche. *Cell* **166**, 1117-1131.e14 (2016).

211. Crompton, J. G. *et al.* Akt inhibition enhances expansion of potent tumor-specific lymphocytes with memory cell characteristics. *Cancer Res.* **75**, 296–305 (2015).

212. Pilon-Thomas, S. *et al.* Neutralization of Tumor Acidity Improves Antitumor Responses to Immunotherapy. *Cancer Res.* **76**, 1381–1390 (2016).

213. Liu, P.-S. *et al.* Alpha-ketoglutarate orchestrates macrophage activation through metabolic and epigenetic reprogramming. *Nat. Immunol.* **18**, 985–994 (2017).

214. Kanarek, N., Petrova, B. & Sabatini, D. M. Dietary modifications for enhanced cancer therapy. *Nature* **579**, 507–517 (2020).

215. Terzo, E. A. *et al.* SETD2 loss sensitizes cells to PI3Kβ and AKT inhibition. *Oncotarget* **10**, 647–659 (2019).

216. Hsieh, J. J. *et al.* Renal cell carcinoma. *Nat. Rev. Dis. Prim.* **3**, 17009 (2017).

217. Jonasch, E. *et al.* State of the science: an update on renal cell carcinoma. *Mol. Cancer Res.* **10**, 859–880 (2012).

218. Motzer, R. J., Hutson, T. E., McCann, L., Deen, K. & Choueiri, T. K. Overall survival in renal-cell carcinoma with pazopanib versus sunitinib. *The New England journal of medicine* **370**, 1769–1770 (2014).

219. Gnarra, J. R. *et al.* Mutations of the VHL tumour suppressor gene in renal carcinoma. *Nat. Genet.* **7**, 85–90 (1994).

220. Brugarolas, J. Molecular genetics of clear-cell renal cell carcinoma. *J. Clin. Oncol.* **32**, 1968–1976 (2014).

221. Hakimi, A. A., Pham, C. G. & Hsieh, J. J. A clear picture of renal cell carcinoma. *Nature genetics* **45**, 849–850 (2013).

222. Linehan, W. M., Srinivasan, R. & Schmidt, L. S. The genetic basis of kidney cancer: a

metabolic disease. *Nat. Rev. Urol.* **7**, 277–285 (2010).

223. Varela, I. *et al.* Exome sequencing identifies frequent mutation of the SWI/SNF complex gene PBRM1 in renal carcinoma. *Nature* **469**, 539–542 (2011).

224. Hakimi, A. A. *et al.* Adverse outcomes in clear cell renal cell carcinoma with mutations of 3p21 epigenetic regulators BAP1 and SETD2: a report by MSKCC and the KIRC TCGA research network. *Clin. Cancer Res.* **19**, 3259–3267 (2013).

225. Kapur, P. *et al.* Effects on survival of BAP1 and PBRM1 mutations in sporadic clear-cell renal-cell carcinoma: a retrospective analysis with independent validation. *Lancet. Oncol.* **14**, 159–167 (2013).

226. Nam, S. J., Lee, C., Park, J. H. & Moon, K. C. Decreased PBRM1 expression predicts unfavorable prognosis in patients with clear cell renal cell carcinoma. *Urol. Oncol.* **33**, 340.e9–16 (2015).

227. Edmunds, J. W., Mahadevan, L. C. & Clayton, A. L. Dynamic histone H3 methylation during gene induction: HYPB/Setd2 mediates all H3K36 trimethylation. *EMBO J.* **27**, 406–420 (2008).

228. Yoh, S. M., Lucas, J. S. & Jones, K. A. The Iws1:Spt6:CTD complex controls cotranscriptional mRNA biosynthesis and HYPB/Setd2-mediated histone H3K36 methylation. *Genes Dev.* **22**, 3422–3434 (2008).

229. Brugge, J., Hung, M.-C. & Mills, G. B. A new mutational AKTivation in the PI3K pathway. *Cancer Cell* **12**, 104–107 (2007).

230. Feng, C. *et al.* PI3Kβ inhibitor TGX221 selectively inhibits renal cell carcinoma cells with both VHL and SETD2 mutations and links multiple pathways. *Sci. Rep.* **5**, 9465 (2015).

231. Dronamraju, R. *et al.* Set2 methyltransferase facilitates cell cycle progression by

maintaining transcriptional fidelity. *Nucleic Acids Res.* **46**, 1331–1344 (2018).

232. Miller, T. W. *et al.* Hyperactivation of phosphatidylinositol-3 kinase promotes escape from hormone dependence in estrogen receptor-positive human breast cancer. *J. Clin. Invest.* **120**, 2406–2413 (2010).

233. Barata, P. C. & Rini, B. I. Treatment of renal cell carcinoma: Current status and future directions. *CA. Cancer J. Clin.* **67**, 507–524 (2017).

234. Hacker, K. E. *et al.* Structure/Function Analysis of Recurrent Mutations in SETD2 Protein Reveals a Critical and Conserved Role for a SET Domain Residue in Maintaining Protein Stability and Histone H3 Lys-36 Trimethylation. *J. Biol. Chem.* **291**, 21283–21295 (2016).

235. Zhu, X. *et al.* Identification of functional cooperative mutations of SETD2 in human acute leukemia. *Nat. Genet.* **46**, 287–293 (2014).

236. Cerami, E. *et al.* The cBio cancer genomics portal: an open platform for exploring multidimensional cancer genomics data. *Cancer Discov.* **2**, 401–404 (2012).

237. Lehmann, B. D. *et al.* Identification of human triple-negative breast cancer subtypes and preclinical models for selection of targeted therapies. *J. Clin. Invest.* **121**, 2750–2767 (2011).

238. Zhang, N. *et al.* Overexpression of Separase induces aneuploidy and mammary tumorigenesis. *Proc. Natl. Acad. Sci. U. S. A.* **105**, 13033–13038 (2008).

239. Xiang, B. & Muthuswamy, S. K. Using three-dimensional acinar structures for molecular and cell biological assays. *Methods Enzymol.* **406**, 692–701 (2006).

240. Wolf, P. The nature and significance of platelet products in human plasma. *Br. J. Haematol.* **13**, 269–288 (1967).

241. Harding, C., Heuser, J. & Stahl, P. Receptor-mediated endocytosis of transferrin and recycling of the transferrin receptor in rat reticulocytes. *J. Cell Biol.* **97**, 329–339 (1983).

242. Pan, B. T., Teng, K., Wu, C., Adam, M. & Johnstone, R. M. Electron microscopic evidence for externalization of the transferrin receptor in vesicular form in sheep reticulocytes. *J. Cell Biol.* **101**, 942–948 (1985).

243. Maas, S. L. N., Breakefield, X. O. & Weaver, A. M. Extracellular vesicles: unique intercellular delivery vehicles. *Trends Cell Biol.* **27**, 172–188 (2017).

244. LeBleu, V. S. & Kalluri, R. Exosomes as a Multicomponent Biomarker Platform in Cancer. *Trends in cancer* **6**, 767–774 (2020).

245. Cocozza, F., Grisard, E., Martin-Jaular, L., Mathieu, M. & Théry, C. SnapShot: Extracellular Vesicles. *Cell* **182**, 262-262.e1 (2020).

246. Hanahan, D. & Weinberg, R. A. The hallmarks of cancer. *Cell* **100**, 57–70 (2000).

247. Mulcahy, L. A., Pink, R. C. & Carter, D. R. F. Routes and mechanisms of extracellular vesicle uptake. *J. Extracell. vesicles* **3**, (2014).

248. Bonsergent, E. *et al.* Quantitative characterization of extracellular vesicle uptake and content delivery within mammalian cells. *Nat. Commun.* **12**, 1864 (2021).

249. van Niel, G., D'Angelo, G. & Raposo, G. Shedding light on the cell biology of extracellular vesicles. *Nat. Rev. Mol. Cell Biol.* **19**, 213–228 (2018).

250. Colombo, M. *et al.* Analysis of ESCRT functions in exosome biogenesis, composition and secretion highlights the heterogeneity of extracellular vesicles. *J. Cell Sci.* **126**, 5553–5565 (2013).

251. McCullough, J., Fisher, R. D., Whitby, F. G., Sundquist, W. I. & Hill, C. P. ALIX-CHMP4 interactions in the human ESCRT pathway. *Proc. Natl. Acad. Sci. U. S. A.* **105**,

7687–7691 (2008).

252. Baietti, M. F. *et al.* Syndecan-syntenin-ALIX regulates the biogenesis of exosomes. *Nat. Cell Biol.* **14**, 677–685 (2012).

253. Ghossoub, R. *et al.* Syntenin-ALIX exosome biogenesis and budding into multivesicular bodies are controlled by ARF6 and PLD2. *Nat. Commun.* **5**, 3477 (2014).

254. Imjeti, N. S. *et al.* Syntenin mediates SRC function in exosomal cell-to-cell communication. *Proc. Natl. Acad. Sci. U. S. A.* **114**, 12495–12500 (2017).

255. Roucourt, B., Meeussen, S., Bao, J., Zimmermann, P. & David, G. Heparanase activates the syndecan-syntenin-ALIX exosome pathway. *Cell Res.* **25**, 412–428 (2015).

256. Stuffers, S., Sem Wegner, C., Stenmark, H. & Brech, A. Multivesicular endosome biogenesis in the absence of ESCRTs. *Traffic* **10**, 925–937 (2009).

257. Laulagnier, K. *et al.* Mast cell- and dendritic cell-derived exosomes display a specific lipid composition and an unusual membrane organization. *Biochem. J.* **380**, 161–171 (2004).

258. Brouwers, J. F. *et al.* Distinct lipid compositions of two types of human prostasomes. *Proteomics* **13**, 1660–1666 (2013).

259. Trajkovic, K. *et al.* Ceramide triggers budding of exosome vesicles into multivesicular endosomes. *Science* **319**, 1244–1247 (2008).

260. Catalano, M. & O'Driscoll, L. Inhibiting extracellular vesicles formation and release: a review of EV inhibitors. *J. Extracell. vesicles* **9**, 1703244 (2020).

261. Menck, K. *et al.* Neutral sphingomyelinases control extracellular vesicles budding from the plasma membrane. *J. Extracell. vesicles* **6**, 1378056 (2017).

262. Vuckovic, S. *et al.* The cationic small molecule GW4869 is cytotoxic to high phosphatidylserine-expressing myeloma cells. *Br. J. Haematol.* **177**, 423–440 (2017).

263. Wei, D. *et al.* RAB31 marks and controls an ESCRT-independent exosome pathway. *Cell Res.* **31**, 157–177 (2021).

264. Ostrowski, M. *et al.* Rab27a and Rab27b control different steps of the exosome secretion pathway. *Nat. Cell Biol.* **12**, 13–19 (2010).

265. Villarroya-Beltri, C. *et al.* ISGylation controls exosome secretion by promoting lysosomal degradation of MVB proteins. *Nat. Commun.* **7**, 13588 (2016).

266. Messenger, S. W., Woo, S. S., Sun, Z. & Martin, T. F. J. A Ca(2+)-stimulated exosome release pathway in cancer cells is regulated by Munc13-4. *J. Cell Biol.* **217**, 2877–2890 (2018).

267. Hyenne, V. *et al.* RAL-1 controls multivesicular body biogenesis and exosome secretion. *J. Cell Biol.* **211**, 27–37 (2015).

268. Verweij, F. J. *et al.* Quantifying exosome secretion from single cells reveals a modulatory role for GPCR signaling. *J. Cell Biol.* **217**, 1129–1142 (2018).

269. Tricarico, C., Clancy, J. & D'Souza-Schorey, C. Biology and biogenesis of shed microvesicles. *Small GTPases* **8**, 220–232 (2017).

270. Antonyak, M. A., Wilson, K. F. & Cerione, R. A. R(h)oads to microvesicles. *Small GTPases* **3**, 219–224 (2012).

271. Beer, K. B. *et al.* Extracellular vesicle budding is inhibited by redundant regulators of TAT-5 flippase localization and phospholipid asymmetry. *Proc. Natl. Acad. Sci. U. S. A.* **115**, E1127–E1136 (2018).

272. Muralidharan-Chari, V. *et al.* ARF6-regulated shedding of tumor cell-derived plasma membrane microvesicles. *Curr. Biol.* **19**, 1875–1885 (2009).

273. Schlienger, S., Campbell, S. & Claing, A. ARF1 regulates the Rho/MLC pathway to

control EGF-dependent breast cancer cell invasion. *Mol. Biol. Cell* **25**, 17–29 (2014).

274. Nabhan, J. F., Hu, R., Oh, R. S., Cohen, S. N. & Lu, Q. Formation and release of arrestin domain-containing protein 1-mediated microvesicles (ARMMs) at plasma membrane by recruitment of TSG101 protein. *Proc. Natl. Acad. Sci. U. S. A.* **109**, 4146–4151 (2012).

275. Jeppesen, D. K. *et al.* Reassessment of Exosome Composition. *Cell* **177**, 428-445.e18 (2019).

276. Tkach, M. & Théry, C. Communication by Extracellular Vesicles: Where We Are and Where We Need to Go. *Cell* **164**, 1226–1232 (2016).

277. Witwer, K. W. & Théry, C. Extracellular vesicles or exosomes? On primacy, precision, and popularity influencing a choice of nomenclature. *Journal of extracellular vesicles* **8**, 1648167 (2019).

278. Al-Nedawi, K. *et al.* Intercellular transfer of the oncogenic receptor EGFRvIII by microvesicles derived from tumour cells. *Nat. Cell Biol.* **10**, 619–624 (2008).

279. Ma, S. *et al.* Gain-of-function p53 protein transferred via small extracellular vesicles promotes conversion of fibroblasts to a cancer-associated phenotype. *Cell Rep.* **34**, 108726 (2021).

280. Nabet, B. Y. *et al.* Exosome RNA Unshielding Couples Stromal Activation to Pattern Recognition Receptor Signaling in Cancer. *Cell* **170**, 352-366.e13 (2017).

281. Melo, S. A. *et al.* Cancer exosomes perform cell-independent microRNA biogenesis and promote tumorigenesis. *Cancer Cell* **26**, 707–721 (2014).

282. Antonyak, M. A. *et al.* Cancer cell-derived microvesicles induce transformation by transferring tissue transglutaminase and fibronectin to recipient cells. *Proc. Natl. Acad. Sci. U. S. A.* **108**, 4852–4857 (2011).

283. Zhang, Q. *et al.* Transfer of Functional Cargo in Exomeres. *Cell Rep.* **27**, 940-954.e6 (2019).

284. Luga, V. *et al.* Exosomes mediate stromal mobilization of autocrine Wnt-PCP signaling in breast cancer cell migration. *Cell* **151**, 1542–1556 (2012).

285. Clancy, J. W. *et al.* Regulated delivery of molecular cargo to invasive tumour-derived microvesicles. *Nat. Commun.* **6**, 6919 (2015).

286. Sung, B. H., Ketova, T., Hoshino, D., Zijlstra, A. & Weaver, A. M. Directional cell movement through tissues is controlled by exosome secretion. *Nat. Commun.* **6**, 7164 (2015).

287. Sung, B. H. *et al.* A live cell reporter of exosome secretion and uptake reveals pathfinding behavior of migrating cells. *Nat. Commun.* **11**, 2092 (2020).

288. Zomer, A. *et al.* In Vivo imaging reveals extracellular vesicle-mediated phenocopying of metastatic behavior. *Cell* **161**, 1046–1057 (2015).

289. Bertolini, I. *et al.* Small Extracellular Vesicle Regulation of Mitochondrial Dynamics Reprograms a Hypoxic Tumor Microenvironment. *Dev. Cell* **55**, 163-177.e6 (2020).

290. Peinado, H. *et al.* Melanoma exosomes educate bone marrow progenitor cells toward a pro-metastatic phenotype through MET. *Nat. Med.* **18**, 883–91 (2012).

291. Rodrigues, G. *et al.* Tumour exosomal CEMIP protein promotes cancer cell colonization in brain metastasis. *Nat. Cell Biol.* **21**, 1403–1412 (2019).

292. Zhang, L. *et al.* Microenvironment-induced PTEN loss by exosomal microRNA primes brain metastasis outgrowth. *Nature* **527**, 100–104 (2015).

293. Hoshino, A. *et al.* Tumour exosome integrins determine organotropic metastasis. *Nature* **527**, 329–335 (2015).

294. Ortiz, A. *et al.* An Interferon-Driven Oxysterol-Based Defense against Tumor-Derived Extracellular Vesicles. *Cancer Cell* **35**, 33-45.e6 (2019).

295. Ko, S. Y. *et al.* Cancer-derived small extracellular vesicles promote angiogenesis by heparin-bound, bevacizumab-insensitive VEGF, independent of vesicle uptake. *Commun. Biol.* **2**, 386 (2019).

296. Feng, Q. *et al.* A class of extracellular vesicles from breast cancer cells activates VEGF receptors and tumour angiogenesis. *Nat. Commun.* **8**, 14450 (2017).

297. Sato, S. *et al.* EPHB2 carried on small extracellular vesicles induces tumor angiogenesis via activation of ephrin reverse signaling. *JCI Insight* **4**, (2019).

298. Li, J., Yuan, H., Xu, H., Zhao, H. & Xiong, N. Hypoxic Cancer-Secreted Exosomal miR-182-5p Promotes Glioblastoma Angiogenesis by Targeting Kruppel-like Factor 2 and 4. *Mol. Cancer Res.* **18**, 1218–1231 (2020).

299. Hsu, Y.-L. *et al.* Hypoxic lung cancer-secreted exosomal miR-23a increased angiogenesis and vascular permeability by targeting prolyl hydroxylase and tight junction protein ZO-1. *Oncogene* **36**, 4929–4942 (2017).

300. Webber, J. P. *et al.* Differentiation of tumour-promoting stromal myofibroblasts by cancer exosomes. *Oncogene* **34**, 290–302 (2015).

301. Maji, S. *et al.* Exosomal Annexin II Promotes Angiogenesis and Breast Cancer Metastasis. *Mol. Cancer Res.* **15**, 93–105 (2017).

302. Lucero, R. *et al.* Glioma-Derived miRNA-Containing Extracellular Vesicles Induce Angiogenesis by Reprogramming Brain Endothelial Cells. *Cell Rep.* **30**, 2065-2074.e4 (2020).

303. Kucharzewska, P. *et al.* Exosomes reflect the hypoxic status of glioma cells and mediate

hypoxia-dependent activation of vascular cells during tumor development. *Proc. Natl. Acad. Sci. U. S. A.* **110**, 7312–7317 (2013).

304. Clayton, A. *et al.* Human tumor-derived exosomes down-modulate NKG2D expression. *J. Immunol.* **180**, 7249–7258 (2008).

305. Huber, V. *et al.* Human colorectal cancer cells induce T-cell death through release of proapoptotic microvesicles: role in immune escape. *Gastroenterology* **128**, 1796–1804 (2005).

306. Fu, W. *et al.* CAR exosomes derived from effector CAR-T cells have potent antitumour effects and low toxicity. *Nat. Commun.* **10**, 4355 (2019).

307. Wolfers, J. *et al.* Tumor-derived exosomes are a source of shared tumor rejection antigens for CTL cross-priming. *Nat. Med.* **7**, 297–303 (2001).

308. Plebanek, M. P. *et al.* Pre-metastatic cancer exosomes induce immune surveillance by patrolling monocytes at the metastatic niche. *Nat. Commun.* **8**, 1319 (2017).

309. Moroishi, T. *et al.* The Hippo Pathway Kinases LATS1/2 Suppress Cancer Immunity. *Cell* **167**, 1525-1539.e17 (2016).

310. Neviani, P. *et al.* Natural Killer-Derived Exosomal miR-186 Inhibits Neuroblastoma Growth and Immune Escape Mechanisms. *Cancer Res.* **79**, 1151–1164 (2019).

311. Chen, F. *et al.* Extracellular vesicle-packaged HIF-1α-stabilizing lncRNA from tumour-associated macrophages regulates aerobic glycolysis of breast cancer cells. *Nat. Cell Biol.* **21**, 498–510 (2019).

312. Speth, J. M. *et al.* Alveolar macrophage secretion of vesicular SOCS3 represents a platform for lung cancer therapeutics. *JCI insight* **4**, (2019).

313. Zhu, J. & Thompson, C. B. Metabolic regulation of cell growth and proliferation. *Nat.*

Rev. Mol. Cell Biol. **20**, 436–450 (2019).

314. Yang, E. *et al.* Exosome-mediated metabolic reprogramming: the emerging role in tumor microenvironment remodeling and its influence on cancer progression. *Signal Transduct. Target. Ther.* **5**, 242 (2020).

315. Ronquist, K. G., Ek, B., Stavreus-Evers, A., Larsson, A. & Ronquist, G. Human prostasomes express glycolytic enzymes with capacity for ATP production. *Am. J. Physiol. Endocrinol. Metab.* **304**, E576-82 (2013).

316. Zhao, H. *et al.* Tumor microenvironment derived exosomes pleiotropically modulate cancer cell metabolism. *Elife* **5**, e10250 (2016).

317. Minciacchi, V. R. *et al.* Large oncosomes contain distinct protein cargo and represent a separate functional class of tumor-derived extracellular vesicles. *Oncotarget* **6**, 11327–11341 (2015).

318. Qu, L. *et al.* Exosome-transmitted lncARSR promotes sunitinib resistance in renal cancer by acting as a competing endogenous RNA. *Cancer Cell* **29**, 653–668 (2016).

319. Zhou, L. *et al.* Targeting MET and AXL overcomes resistance to sunitinib therapy in renal cell carcinoma. *Oncogene* **35**, 2687–2697 (2016).

320. Binenbaum, Y. *et al.* Transfer of miRNA in Macrophage-Derived Exosomes Induces Drug Resistance in Pancreatic Adenocarcinoma. *Cancer Res.* **78**, 5287–5299 (2018).

321. Kreger, B. T., Johansen, E. R., Cerione, R. A. & Antonyak, M. A. The Enrichment of Survivin in Exosomes from Breast Cancer Cells Treated with Paclitaxel Promotes Cell Survival and Chemoresistance. *Cancers (Basel).* **8**, (2016).

322. Ma, X. *et al.* Essential role for TrpC5-containing extracellular vesicles in breast cancer with chemotherapeutic resistance. *Proc. Natl. Acad. Sci. U. S. A.* **111**, 6389–6394 (2014).

323. Boelens, M. C. *et al.* Exosome transfer from stromal to breast cancer cells regulates therapy resistance pathways. *Cell* **159**, 499–513 (2014).

324. Skog, J. *et al.* Glioblastoma microvesicles transport RNA and proteins that promote tumour growth and provide diagnostic biomarkers. *Nat. Cell Biol.* **10**, 1470–6 (2008).

325. Melo, S. A. *et al.* Glypican-1 identifies cancer exosomes and detects early pancreatic cancer. *Nature* **523**, 177–182 (2015).

326. Lai, X. *et al.* A microRNA signature in circulating exosomes is superior to exosomal glypican-1 levels for diagnosing pancreatic cancer. *Cancer Lett.* **393**, 86–93 (2017).

327. Hoshino, A. *et al.* Extracellular Vesicle and Particle Biomarkers Define Multiple Human Cancers. *Cell* **182**, 1044-1061.e18 (2020).

328. Ridder, K. *et al.* Extracellular vesicle-mediated transfer of functional RNA in the tumor microenvironment. *Oncoimmunology* **4**, e1008371 (2015).

329. Kowal, J. *et al.* Proteomic comparison defines novel markers to characterize heterogeneous populations of extracellular vesicle subtypes. *Proc. Natl. Acad. Sci. U. S. A.* **113**, E968-77 (2016).

330. Morales-Kastresana, A. *et al.* Labeling Extracellular Vesicles for Nanoscale Flow Cytometry. *Sci. Rep.* **7**, 1878 (2017).

331. Gangadaran, P. *et al.* A new bioluminescent reporter system to study the biodistribution of systematically injected tumor-derived bioluminescent extracellular vesicles in mice. *Oncotarget* **8**, 109894–109914 (2017).

332. Lai, C. P. *et al.* Dynamic biodistribution of extracellular vesicles in vivo using a multimodal imaging reporter. *ACS Nano* **8**, 483–494 (2014).

333. Zhang, P. *et al.* Ultrasensitive detection of circulating exosomes with a 3D-nanopatterned

microfluidic chip. *Nat. Biomed. Eng.* **3**, 438–451 (2019).

334. Siegel, R. L., Miller, K. D., Fuchs, H. E. & Jemal, A. Cancer Statistics, 2021. *CA. Cancer J. Clin.* **71**, 7–33 (2021).

335. Linehan, W. M. *et al.* The Metabolic Basis of Kidney Cancer. *Cancer Discov.* **9**, 1006–1021 (2019).

336. Rey, S. & Semenza, G. L. Hypoxia-inducible factor-1-dependent mechanisms of vascularization and vascular remodelling. *Cardiovasc. Res.* **86**, 236–242 (2010).

337. Cao, Y. *et al.* VEGF exerts an angiogenesis-independent function in cancer cells to promote their malignant progression. *Cancer Res.* **72**, 3912–3918 (2012).

338. McKay, R. R., Bossé, D. & Choueiri, T. K. Evolving systemic treatment landscape for patients with advanced renal cell carcinoma. *J. Clin. Oncol.* JCO2018790253 (2018). doi:10.1200/JCO.2018.79.0253

339. Göran Ronquist, K. Extracellular vesicles and energy metabolism. *Clin. Chim. Acta.* **488**, 116–121 (2019).

340. Carayon, K. *et al.* Proteolipidic composition of exosomes changes during reticulocyte maturation. *J. Biol. Chem.* **286**, 34426–34439 (2011).

341. Umezu, T. *et al.* Exosomal miR-135b shed from hypoxic multiple myeloma cells enhances angiogenesis by targeting factor-inhibiting HIF-1. *Blood* **124**, 3748–3757 (2014).

342. Parolini, I. *et al.* Microenvironmental pH is a key factor for exosome traffic in tumor cells. *J. Biol. Chem.* **284**, 34211–34222 (2009).

343. King, H. W., Michael, M. Z. & Gleadle, J. M. Hypoxic enhancement of exosome release by breast cancer cells. *BMC Cancer* **12**, 421 (2012).

344. Panigrahi, G. K. *et al.* Hypoxia-induced exosome secretion promotes survival of African-American and Caucasian prostate cancer cells. *Sci. Rep.* **8**, 3853 (2018).

345. Voss, B. J. *et al.* Alteration of the Helicobacter pylori membrane proteome in response to changes in environmental salt concentration. *Proteomics. Clin. Appl.* **9**, 1021–1034 (2015).

346. Thissen, D., Steinberg, L. & Kuang, D. Quick and easy implementation of the Benjamini-Hochberg Procedure for controlling the false positive rate in multiple comparisons. *J. Educ. Behav. Stat.* **27**, 77–83 (2002).

347. Valley, M. P. *et al.* A bioluminescent assay for measuring glucose uptake. *Anal. Biochem.* **505**, 43–50 (2016).

348. Chandrashekar, D. S. *et al.* UALCAN: a portal for facilitating tumor subgroup gene expression and survival analyses. *Neoplasia* **19**, 649–658 (2017).

349. Liang, W. *et al.* FAM3D is essential for colon homeostasis and host defense against inflammation associated carcinogenesis. *Nat. Commun.* **11**, 5912 (2020).

350. Wood, C. G. *et al.* Neoadjuvant pazopanib and molecular analysis of tissue response in renal cell carcinoma. *JCI Insight* **5(22):e132**, (2020).

351. Théry, C. *et al.* Minimal information for studies of extracellular vesicles 2018 (MISEV2018): a position statement of the International Society for Extracellular Vesicles and update of the MISEV2014 guidelines. *J. Extracell. Vesicles* **7**, 1535750 (2018).

352. Liu, X.-D. *et al.* Resistance to Antiangiogenic Therapy Is Associated with an Immunosuppressive Tumor Microenvironment in Metastatic Renal Cell Carcinoma. *Cancer Immunol. Res.* **3**, 1017–1029 (2015).

353. Adelaiye-Ogala, R. *et al.* EZH2 modifies Sunitinib resistance in renal cell carcinoma by

kinome reprogramming. *Cancer Res.* **77**, 6651–6666 (2017).

354. Brooks, S. A. *et al.* Alternate Metabolic Programs Define Regional Variation of Relevant Biological Features in Renal Cell Carcinoma Progression. *Clin. Cancer Res.* **22**, 2950–2959 (2016).

355. Ronquist, G. Prostasomes are mediators of intercellular communication: from basic research to clinical implications. *J. Intern. Med.* **271**, 400–413 (2012).

356. Kriebel, P. W. *et al.* Extracellular vesicles direct migration by synthesizing and releasing chemotactic signals. *J. Cell Biol.* **217**, 2891–2910 (2018).

357. Li, J. *et al.* Hypoxic glioma stem cell-derived exosomes containing Linc01060 promote progression of glioma by regulating the MZF1/c-Myc/HIF-1α. *Cancer Res.* (2020). doi:10.1158/0008-5472.CAN-20-2270

358. Carmeliet, P. & Jain, R. K. Principles and mechanisms of vessel normalization for cancer and other angiogenic diseases. *Nat. Rev. Drug Discov.* **10**, 417–427 (2011).

359. Biswas, S. *et al.* Effects of HIF-1alpha and HIF2alpha on Growth and Metabolism of Clear-Cell Renal Cell Carcinoma 786-0 Xenografts. *J. Oncol.* **2010**, 757908 (2010).

360. Turajlic, S. *et al.* Tracking Cancer Evolution Reveals Constrained Routes to Metastases: TRACERx Renal. *Cell* **173**, 581-594.e12 (2018).

361. Monzon, F. A. *et al.* Chromosome 14q loss defines a molecular subtype of clear-cell renal cell carcinoma associated with poor prognosis. *Mod. Pathol.* **24**, 1470–1479 (2011).

362. Ebright, R. Y. *et al.* HIF1A signaling selectively supports proliferation of breast cancer in the brain. *Nat. Commun.* **11**, 6311 (2020).

363. Li, L. *et al.* Exosomes Derived from Hypoxic Oral Squamous Cell Carcinoma Cells Deliver miR-21 to Normoxic Cells to Elicit a Prometastatic Phenotype. *Cancer Res.* **76**,

1770–1780 (2016).

364. Wang, T. *et al.* Hypoxia-inducible factors and RAB22A mediate formation of microvesicles that stimulate breast cancer invasion and metastasis. *Proc. Natl. Acad. Sci. U. S. A.* **111**, E3234-42 (2014).

365. Nicolás-Ávila, J. A. *et al.* A network of macrophages supports mitochondrial homeostasis in the heart. *Cell* **183**, 94-109.e23 (2020).

366. Bader, J. E., Voss, K. & Rathmell, J. C. Targeting metabolism to improve the tumor microenvironment for cancer immunotherapy. *Mol. Cell* **78**, 1019–1033 (2020).

367. Abbott, B. Cancer Death Rate in U.S. Falls by Largest Yearly Amount on Record - WSJ. Available at: https://www.wsj.com/articles/cancer-death-rate-in-u-s-falls-by-largest-yearly-amount-on-record-11610463601. (Accessed: 7th March 2021)

368. Levine, R. L. Cancer did not stay home for COVID-19. *Sci. Adv.* **6**, eabd7487 (2020).

369. Datta, A. *et al.* Manumycin A suppresses exosome biogenesis and secretion via targeted inhibition of Ras/Raf/ERK1/2 signaling and hnRNP H1 in castration-resistant prostate cancer cells. *Cancer Lett.* **408**, 73–81 (2017).

370. Hendricks, M. R. *et al.* Extracellular vesicles promote transkingdom nutrient transfer during viral-bacterial co-infection. *Cell Rep.* **34**, 108672 (2021).

371. Kalluri, R. & LeBleu, V. S. The biology, function, and biomedical applications of exosomes. *Science* **367**, (2020).

372. Nolte-'t Hoen, E., Cremer, T., Gallo, R. C. & Margolis, L. B. Extracellular vesicles and viruses: Are they close relatives? *Proc. Natl. Acad. Sci. U. S. A.* **113**, 9155–9161 (2016).

373. Quinn, W. J. 3rd *et al.* Lactate Limits T Cell Proliferation via the NAD(H) Redox State. *Cell Rep.* **33**, 108500 (2020).

374. Reinfeld, B. I. *et al.* Cell-programmed nutrient partitioning in the tumour microenvironment. *Nature* (2021). doi:10.1038/s41586-021-03442-1

375. Jimenez, L. *et al.* Quantitative Proteomic Analysis of Small and Large Extracellular Vesicles (EVs) Reveals Enrichment of Adhesion Proteins in Small EVs. *J. Proteome Res.* **18**, 947–959 (2019).

376. Hoshino, D. *et al.* Exosome secretion is enhanced by invadopodia and drives invasive behavior. *Cell Rep.* **5**, 1159–1168 (2013).

377. Lim, A. R. & Rathmell, W. K. Chromophobe Renal Cell Carcinoma. in *Rare Kidney Tumors: Comprehensive Multidisciplinary Management and Emerging Therapies* (eds. Malouf, G. G. & Tannir, N. M.) 43–51 (Springer International Publishing, 2019). doi:10.1007/978-3-319-96989-3_4

378. Lopez-Beltran, A. *et al.* 2009 Update on the classification of renal epithelial tumors in adults. *Int. J. Urol.* **16**, 432–443 (2009).

379. Thoenes, W., Storkel, S. & Rumpelt, H. J. Human chromophobe cell renal carcinoma. *Virchows Arch. B. Cell Pathol. Incl. Mol. Pathol.* **48**, 207–217 (1985).

380. Störkel, S., Steart, P. V., Drenckhahn, D. & Thoenes, W. The human chromophobe cell renal carcinoma: Its probable relation to intercalated cells of the collecting duct. *Virchows Arch. B Cell Pathol. Incl. Mol. Pathol.* **56**, 237–245 (1988).

381. Delongchamps, N. B. *et al.* Hybrid tumour 'oncocytoma-chromophobe renal cell carcinoma' of the kidney: A report of seven sporadic cases. *BJU Int.* **103**, 1381–1384 (2009).

382. Podduturi, V., Yourshaw, C. J. & Zhang, H. Eosinophilic variant of chromophobe renal cell carcinoma. *Proc. (Bayl. Univ. Med. Cent).* **28**, 57–8 (2015).

383. Speicher, M. R. *et al.* Specific loss of chromosomes 1, 2, 6, 10, 13, 17, and 21 in chromophobe renal cell carcinomas revealed by comparative genomic hybridization. *Am. J. Pathol.* **145**, 356–364 (1994).

384. Iqbal, M. A., Akhtar, M. & Ali, M. A. Cytogenetic findings in renal cell carcinoma. *Hum. Pathol.* **27**, 949–954 (1996).

385. Davis, C. F. *et al.* The somatic genomic landscape of chromophobe renal cell carcinoma. *Cancer Cell* **26**, 319–330 (2014).

386. Guo, J. *et al.* Tuberous sclerosis-associated renal cell carcinoma: a clinicopathologic study of 57 separate carcinomas in 18 patients. *Am. J. Surg. Pathol.* **38**, 1457–67 (2014).

387. Pavlovich, C. P. *et al.* Renal tumors in the Birt-Hogg-Dubé syndrome. *Am. J. Surg. Pathol.* **26**, 1542–1552 (2002).

388. Delahunt, B. *et al.* Fuhrman grading is not appropriate for chromophobe renal cell carcinoma. *Am. J. Surg. Pathol.* **31**, 957–960 (2007).

389. Steffens, S. *et al.* The Fuhrman grading system has no prognostic value in patients with nonsarcomatoid chromophobe renal cell carcinoma. *Hum. Pathol.* **45**, 2411–2416 (2014).

390. Paner, G. P. *et al.* A novel tumor grading scheme for chromophobe renal cell carcinoma: prognostic utility and comparison with Fuhrman nuclear grade. *Am. J. Surg. Pathol.* **34**, 1233–1240 (2010).

391. Delahunt, B. *et al.* The International Society of Urological Pathology (ISUP) grading system for renal cell carcinoma and other prognostic parameters. *Am. J. Surg. Pathol.* **37**, 1490–1504 (2013).

392. Prasad, S. R. *et al.* Segmental disorders of the nephron: histopathological and imaging perspective. *Br. J. Radiol.* **80**, 593–602 (2007).

393. Fahey, C. C. & Rathmell, W. K. A tale of two cancers: Complete genetic analysis of chromophobe renal cell carcinoma contrasts with clear cell renal cell carcinoma. *Mol. Cell. Oncol.* **2**, e979686 (2015).

394. Birt, A. R. *et al.* Hereditary multiple fibrofolliculomas with trichodiscomas and acrochordons. *Arch. Dermatol.* **113**, 1674 (1977).

395. Schmidt, L. S. *et al.* Birt-Hogg-Dubé syndrome, a genodermatosis associated with spontaneous pneumothorax and kidney neoplasia, maps to chromosome 17p11.2. *Am. J. Hum. Genet.* **69**, 876–882 (2001).

396. Schmidt, L. S. & Linehan, W. M. Molecular genetics and clinical features of Birt–Hogg–Dubé syndrome. *Nat. Rev. Urol.* **12**, 558–569 (2015).

397. Rathmell, K. W., Chen, F. & Creighton, C. J. Genomics of chromophobe renal cell carcinoma: implications from a rare tumor for pan-cancer studies. *Oncoscience* **2**, 81–90 (2015).

398. *Kidney Cancer*. (Springer International Publishing, 2015). doi:10.1007/978-3-319-17903-2

399. Nickerson, M. L. *et al.* Mutations in a novel gene lead to kidney tumors, lung wall defects, and benign tumors of the hair follicle in patients with the Birt-Hogg-Dubé syndrome. *Cancer Cell* **2**, 157–64 (2002).

400. Nagy, A., Zoubakov, D., Stupar, Z. & Kovacs, G. Lack of mutation of the folliculin gene in sporadic chromophobe renal cell carcinoma and renal oncocytoma. *Int. J. Cancer* **109**, 472–475 (2004).

401. Khoo, S. K. *et al.* Inactivation of BHD in sporadic renal tumors. *Cancer Res* **63**, 4583–4587 (2003).

402. Lim, D. H. K. *et al.* A new locus-specific database (LSDB) for mutations in the folliculin (FLCN) gene. *Hum. Mutat.* **31**, E1043–E1051 (2010).

403. Tsun, Z.-Y. *et al.* The folliculin tumor suppressor is a GAP for the RagC/D GTPases that signal amino acid levels to mTORC1. *Mol. Cell* **52**, 495–505 (2013).

404. Hong, S. B. *et al.* Tumor suppressor FLCN inhibits tumorigenesis of a FLCN-null renal cancer cell line and regulates expression of key molecules in TGF-β signaling. *Mol. Cancer* **9**, 160 (2010).

405. Hong, S. B. *et al.* Inactivation of the FLCN tumor suppressor gene induces TFE3 transcriptional activity by increasing its nuclear localization. *PLoS One* **5**, e15793 (2010).

406. Medvetz, D. A. *et al.* Folliculin, the product of the Birt-Hogg-Dube tumor suppressor gene, interacts with the adherens junction protein p0071 to regulate cell-cell adhesion. *PLoS One* **7**, e47842 (2012).

407. Nahorski, M. S. *et al.* Folliculin interacts with p0071 (plakophilin-4) and deficiency is associated with disordered Rhoa signalling, epithelial polarization and cytokinesis. *Hum. Mol. Genet.* **21**, 5268–5279 (2012).

408. Northrup, H. & Krueger, D. A. Tuberous sclerosis complex diagnostic criteria update: Recommendations of the 2012 international tuberous sclerosis complex consensus conference. *Pediatr. Neurol.* **49**, 243–254 (2013).

409. Curatolo, P., Bombardieri, R. & Jozwiak, S. Tuberous sclerosis. *Lancet* **372**, 657–668 (2008).

410. Tee, A. R. *et al.* Tuberous sclerosis complex-1 and -2 gene products function together to inhibit mammalian target of rapamycin (mTOR)-mediated downstream signaling. *Proc. Natl. Acad. Sci. U. S. A.* **99**, 13571–13576 (2002).

411. Crino, P. B., Nathanson, K. L. & Henske, E. P. The tuberous sclerosis complex. *N Engl J Med* **355**, 1345–56 (2006).

412. Washecka, R. & Hanna, M. Malignant renal tumors in tuberous sclerosis. *Urology* **37**, 340–3 (1991).

413. Yang, P. *et al.* Renal cell carcinoma in tuberous sclerosis complex. *Am J Surg Pathol* **38**, 895–909 (2014).

414. Bjornsson, J., Short, M. P., Kwiatkowski, D. J. & Henske, E. P. Tuberous sclerosis-associated renal cell carcinoma. Clinical, pathological, and genetic features. *Am. J. Pathol.* **149**, 1201–8 (1996).

415. Welter, C., Kovacs, G., Seitz, G. & Blin, N. Alteration of mitochondrial DNA in human oncocytomas. *Gene Chromosom. Cancer* **1**, 79–82 (1989).

416. Kovacs, A., Storkel, S., Thoenes, W. & Kovacs, G. Mitochondrial and chromosomal DNA alterations in human chromophobe renal cell carcinomas. *J. Pathol.* **167**, 273–277 (1992).

417. Chomyn, A. Mitochondrial genetic control of assembly and function of complex I in mammalian cells. *J Bioenerg Biomembr.* **33**, 251–257 (2001).

418. Amin, M. B. *et al.* Chromophobe renal cell carcinoma: histomorphologic characteristics and evaluation of conventional pathologic prognostic parameters in 145 cases. *Am. J. Surg. Pathol.* **32**, 1822–1834 (2008).

419. Thoenes, W. *et al.* Chromophobe cell renal carcinoma and its variants--a report on 32 cases. *J. Pathol.* **155**, 277–87 (1988).

420. Crotty, T. B., Farrow, G. M. & Lieber, M. M. Chromophobe cell renal carcinoma: Clinicopathological features of 50 cases. *J. Urol.* **154**, 964–967 (1995).

421. Volpe, A. *et al.* Chromophobe renal cell carcinoma (RCC): Oncological outcomes and

prognostic factors in a large multicentre series. *BJU Int.* **110**, 76–83 (2012).

422. Motzer, R. J. *et al.* Treatment outcome and survival associated with metastatic renal cell carcinoma of non-clear-cell histology. *J. Clin. Oncol.* **20**, 2376–2381 (2002).

423. Escudier, B. *et al.* Renal cell carcinoma: ESMO Clinical Practice Guidelines for diagnosis, treatment and follow-up. *Ann. Oncol.* **27**, v58–v68 (2016).

424. Tsimafeyeu, I. *et al.* Phase II, multicenter, uncontrolled trial of single-agent capecitabine in patients with non-clear cell metastatic renal cell carcinoma. *Am. J. Clin. Oncol.* **35**, 251–254 (2012).

425. Choueiri, T. K. *et al.* Efficacy of sunitinib and sorafenib in metastatic papillary and chromophobe renal cell carcinoma. *J. Clin. Oncol.* **26**, 127–131 (2008).

426. Tannir, N. M. *et al.* A phase 2 trial of sunitinib in patients with advanced non-clear cell renal cell carcinoma. *Eur Urol* **62**, 1013–1019 (2012).

427. Dutcher, J. P. *et al.* Effect of temsirolimus versus interferon-alpha on outcome of patients with advanced renal cell carcinoma of different tumor histologies. *Med. Oncol.* **26**, 202–209 (2009).

428. Koh, Y. *et al.* Phase II trial of everolimus for the treatment of nonclear-cell renal cell carcinoma. *Ann. Oncol.* **24**, 1026–1031 (2013).

429. Tannir, N. M. *et al.* Everolimus versus sunitinib prospective evaluation in metastatic non-clear cell renal cell carcinoma (ESPN): A randomized multicenter phase 2 trial. *Eur. Urol.* **69**, 866–874 (2016).

430. Armstrong, A. J. *et al.* Everolimus versus sunitinib for patients with metastatic non-clear cell renal cell carcinoma (ASPEN): A multicentre, open-label, randomised phase 2 trial. *Lancet Oncol.* **17**, 378–388 (2016).

431. Choueiri, T. K. *et al.* PD-L1 expression in nonclear-cell renal cell carcinoma. *Ann. Oncol.* **25**, 2178–84 (2014).